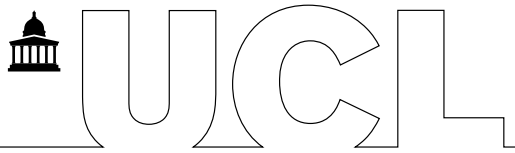

R-matrix calculations of electron-molecule collisions: flexible implementation and practice

Will Brigg

A thesis submitted to University College London

for the degree of Doctor of Philosophy

Department of Physics & Astronomy

University College London

March 18, 2018

I, Will Brigg, confirm that the work presented in this thesis is my own. Where previous work has been derived from other sources, I confirm that this has been referred to in the thesis, and that any images taken from other sources have also been given due credit.

Abstract

This thesis uses the UK computational implementation of the **R**-matrix method to calculate *ab initio* electron scattering cross sections from methane, paying special attention to several different models. The relative rates of convergence, and the reproduction of several key physical properties for each are examined, with the aim of producing a single unified model - in this case specifically for methane, but the practices should theoretically hold for other molecules too. The models specifically look at the inclusion of different classes of electronic configurations, and examine their behaviour with respect to variation of their defining characteristics.

The various properties replicated by this unified model all converge towards the accepted values, however for some properties the convergence is slow, meaning that a calculation large enough to give the desired results would still be impractical at this point.

Also included are descriptions of additions and advances to the Quantemol-N software package, worked on as part of the CASE studentship, and several related extensions, aimed at significantly decreasing the difficulty of utilising the UKRMol suite. The descriptions of these extensions include several example results of other small hydrocarbons, including photoionization cross sections of hydrogen and nitrogen diamers, and methane; photodetachment of the CN^- and C_2H^- anions; total cross sections and eigenphase sums for electron-molecule scattering with water, 1-propanol ($CH_3CH_2CH_2OH$), and carbonyl sulfide (OCS); and finally various cross sections including dissociative electron attachment for Indium(I) Iodide are included.

Acknowledgements

Obvious thanks have to go straight to my parents, for their endless support, and their apparently inexhaustible patience. Four years is a long time. Thank you both.

Also Drs. James Munro first, and then later, Stephen Harrison deserve a huge thank you, for happily dealing with my questions, and sharing with me much of their invaluable experience. You both taught me well, and for that I am grateful.

Everyone else here in the office at Quantemol: Anna, Adam, Arun, Brent, Derek, James, Sebastian, and Sergio, too deserve to be thanked and acknowledged, you have all made the time that much more enjoyable.

I would also like to thank Dr Pavlos Galiatsatos for his help understanding some of the more intricate parts the codes, and also Dr Alex Harvey, for the continuous support integrating his work into Quantemol-N, and many other more general questions.

Dr Martin Plummer also deserves thanks, without whom the larger calculations on methane would probably still be running several years from now. As too does Prof. Viatcheslav Kokoouline for insight, and help in the testing of the photodetachment additions to Quantemol-N.

I would especially like to thank Dr Dan Brown, and Jonathan Tennyson for accepting me for the CASE studentship. As if the normal PhD experience is not enough, the countless extra opportunities this has given me, I am especially grateful for. I will admit that, at first, I thought of Dan as a bit of a taskmaster - but opinions change, and I am extremely grateful for having been driven to achieve so much more. In the initial interview I remember Dan asking me several difficult questions, one of which, inquiring as to a particularly poor *communication skills* result, to which I gave the admittedly cliché answer "If you look at my results then, and now, you can see that I am not the same person I was then that I am now". I believe this is just as true now as it was then, if not more so, and I believe this is in no small part down to being pushed harder to achieve. Thank you Dan.

Finally, I must thank Jonathan again. Completing a PhD requires that you jump through many hoops, many of which put in place to help you guide oneself through the process and, I am sure, to aid those who receive comparatively less face time with their supervisor(s). For me, this was a complete non issue: the amount of help, continuous aid, and the ever present willingness to answer my *many* questions, at all hours of the day and night, is something I will not soon forget.

* * *

This work was funded by the Science & Technology Facilities Council, and also made use of the facilities of HECToR, the UK's national high-performance computing service (2007-2015), which was provided by UoE HPCx Ltd at the University of Edinburgh, Cray Inc and NAG Ltd, and funded by the Office of Science and Technology through EPSRC's High End Computing Programme.

Contents

List of Figures

List of Tables

Publications

M. M. Fujimoto, W. J. Brigg, and J. Tennyson, '**R**-Matrix calculations of differential and integral cross sections for low-energy electron collisions with ethanol', *Eur. Phys. J. D* **66** (2014).

> Electron collisions with C_2H_5OH are studied up to impact energies of 10 eV using several theoretical models. Calculated differential cross sections suggest that the extrapolation to low angles used to extend experimental data and hence give integral cross sections significantly underestimates the large, dipole-driven forward scattering cross section. An improved set of values for the rotationally-unresolved elastic cross section is proposed; the corresponding rotationally resolved cross sections are also presented. Static exchange plus polarisation calculations find a very broad shape resonance in each of the $2A'$ and $2A''$ symmetries in the 7 eV collision region however no resonance at lower energies, in qualitative agreement with the interpretation of some but not all dissociative electron attachment measurements.

W. J. Brigg, J. Tennyson, and M. Plummer, 'R-matrix calculations of low-energy electron collisions with methane', *J. Phys. B: At. Mol. Opt.* **47** (2014), p. 185203.

> R-matrix calculations are performed for electron collision with CH_4 at energies between 0.02 and 15 eV using a series of different *ab initio* models for both the target and the full scattering system. A target model similar to the standard multi-reference configuration interaction used in electronic structure calculations is found to give the best results. Results are presented for elastic scattering, with particular emphasis on the Ramsauer-Townsend miminum, and for rotational excitation, momentum transfer and electron impact dissociation. Extensive comparisons are made with previous studies.

W. J. Brigg, A. G. Harvey, A. Dzarasova, S. Mohr, D. S. Brambila, F. Morales, O. Smirnova, and J. Tennyson, 'Calculated photoionization cross sections using Quantemol-N', *Jpn. J. Appl. Phys.* (2015).

> Quantemol-N is an expert system designed to run the widely used UK Molecular R-matrix code (UKRMol). Originally designed to consider electron - molecule collision problems, here we present an extension to treat molecular photoionization. Sample results are given for the photoionization of molecular nitrogen and methane. Comparisons are made with experimental results showing good agreement.

1

Introduction

1.1 A CASE studentship

The work undertaken to complete this thesis was part of an Industrial *Collaborative Awards in Science and Engineering* (CASE) Studentship, funded by the Science & Technology Facilities Council. This entails time being split between the academic side, and with the industrial partner - in this case, the company Quantemol.

The aim here is to provide the student with additional experience outside of that usually obtained in a PhD. The relationship between the student and industrial partner is symbiotic though, especially for this company in particular: the overlap is considerable, and knowledge gained on each side is beneficial in the other role. New developments on the academic side filter through into the codes upon which the Quantemol software is based. Incorporating these improvements and advances into the software requires a general understanding of what is happening, rather than simply understanding the relatively narrow specifics of just your own test case; this requirement very much helps improve understanding of the physics involved and, at least in my opinion, is a very valuable activity in terms of learning.

A more thorough description of the Quantemol codes is given in the Quantemol-N section, page 84, before this though we cover the **R**-matrix theory, upon which the Quantemol-N software builds.

1.2 Electron-molecule collisions

Electron-molecule collisions are an important underlying process in many active areas of modern research (Trajmar et al., 2006; Mason, 2009; Tennyson, 2010). There are the realms of plasma physics, and discharges, which encompass many orders of magnitude in scale. At one end of the scale is the enormous, such as the weakly ionized interstellar medium (Geppert and Larsson, 2008), and hotter regions of the interstellar medium, in shocks (Fuente et al., 2008), and planetary nebulae (Röllig et al., 2007). At intermediate scales, such as atmospheric physics, including auroras, both at home (Huestis et al., 2008), and extra terrestrially (Ajello et al., 2001), and lightning (Luque et al., 2008). Then we have the other end of the gamut; small scales used in the industries dominating much of modern technology, such as plasma etching and thin film deposition. These plasma processes are also important in some fusion reactors, and the discharges initiating laser processes, as well as more mature processes, such as spark plugs in combustion engines, electric lighting, and gaseous high voltage switches. Outside of the plasma physics, and discharges world, they are also now widely accepted to be the main cause of radiation damage within cells (Michael and O'Neill, 2000).

The ubiquity of electron molecule collisions has driven much research, both theoretical (Winstead and Mckoy, 2000), and experimental (Brunger and Buckman, 2002).

1.2.1 Experimental Methods

Electron-molecule scattering experiments are difficult: the process that is ultimately being investigated has to be extracted from a chain of results, each with its own specific dependencies on the numerous details of the instrumental set up, which each introduce additional uncertainties and considerations necessary to yield an accurate cross section.

There are several different experimental techniques for obtaining electron-molecule scattering cross sections. A few popular methods are described below, along with the common issues that need to be dealt with.

The *transmission* family of experiments, covered in more detail in Bederson and Kieffer (1971), involve firing an electron beam through a chamber containing the species

of interest, and measuring its attenuation. The total cross section is then extracted from the measured electron current using the Beer-Lambert law:

$$I(a) = I_0 \exp(-nl\sigma)$$

where the I_0 is the initial and $I(a)$ the final measured currents, l is the length of the chamber, and n is the density of the target gas. This produces what is known as a *grand total cross section*, since it includes all scattering processes of the electrons. Experiments are usually performed such that the density of the target species is set such that it can be reasonably assumed that the electron only scatters once.

Another family of techniques involve the observation of the angular dependence as well, and then total cross sections are obtained by integrating over the angular distribution. One way of achieving this is by taking a similar set up described for a transmission experiment, but positioning the detector away from the path of the electron beam. Alternatively, one can carry out a *crossed beam* experiment (Trajmar and McConkey, 1994), where in addition to the electron beam, a molecular (or atomic) beam is introduced. In both of these techniques the differential cross section is then inferred from the number of scattered electrons detected at different angular positions.

In the techniques described above, the electron detector can be an *electron energy-loss spectrometer* (EELS); capable of discriminating between electrons of different energy, where the difference in the initial and final energies of the electrons in the beam has excited the target species in some way. This gives a count of electrons of various energies (corresponding to different target excited states) per energy, and allows inelastic cross sections to be calculated.

Of course, these scattering experiments are not quite as simple as described above, and have to additionally take into account factors introduced by the instrumental set up. For example, whenever a beam is used, the energy and spatial distribution of the electron beam (and in the case of a crossed beam experiment, the density distribution of the target molecules too) must be considered.The response of the electron detector, which is often non-linear (especially at low energy), must also be carefully calibrated for each angle and energy investigated. These difficulties, as well as many other con-

siderations are covered in great detail by Bederson and Kieffer (1971); Nickel et al. (1989); Trajmar and McConkey (1994); Brunger and Buckman (2002), and are some of the reasons that electron scattering experiments are difficult.

These difficulties, or more accurately the attractiveness of avoiding them, have driven many advances in the field. One of which, known as the *relative flow* technique, does away with requiring many of these aspects be calibrated. Instead, the experiment is performed twice, once for the species of interest, and again with a species whose cross section is known accurately. For low energy the *standard* cross section to compare against is usually electron-helium (Brunger and Buckman, 2002), though it has also been suggested that neon be used as a secondary standard (Shi and Burrow, 1992).

Another advance involves replacing EELSs with a *field-free drift tube*, and have the electron beam pulsed. The scattered electrons then traverse the drift tube, this separates the electrons temporally, depending on the energy loss. This is known as the *time of flight* approach (LeClair et al., 1996), it is simpler to carry out, and removes the energy dependence of the detector from the list of difficulties of scattering experiments.

A final, important, consideration to note is that experimental differential cross sections are not possible at all angles, backscattering is difficult simply due to the geometry of the problem: the detector can not be in the same place as the source; though the use magnetic fields to rotate the incoming and outgoing electrons now allows backscattering to be measured too (Zubek et al., 1996; Read and Channing, 1996). Forward scattering is also problematic, since the unscattered electron beam coincides with the forward scattering - this can not be dealt with by rotating the beams. Typically, the range over which the DCS is measured is $\theta_{\text{min}} \leqslant \theta_{\text{measured}} \leqslant 140°$; where, depending on the electron energy, $\theta_{\text{min}} \approx 10°$ for elastic scattering, and $\theta_{\text{min}} \approx 5°$ for inelastic processes (Brunger and Buckman, 2002). These portions therefore need to be extrapolated in order to obtain the total cross section; unfortunately it is also these regions which often contribute significantly to the scattering, especially for scattering from polar molecules. There are several techniques for the extrapolation of these DCSs, discussed in Brunger et al. (1990); Lun et al. (1994); Sun et al. (1995); Zhang et al. (2011).

In general, more data is found for smaller target molecules, with there being less activity (experimental and theoretical) for more complicated targets. There are also fewer studies on excited species, and radicals. Excited states are more difficult to study since it is very difficult to obtain an molecular beam of targets in a single excited state[1]. The problem is even worse for unstable targets, where the beam is created by breaking up a precursor species - potentially resulting in a beam of multiple, reactive, species, all of which contributing to the measured cross section, though radicals are beginning to be covered more extensively (Maddern et al., 2008a,b).

1.2.2 Theoretical Methods

There are several different theoretical techniques which can be used to calculate scattering cross sections, but a few distinctions should be made first: when describing a set of theoretical results, one can talk about the underlying *theory* used, the specific *implementation* of that theory, and the *model* employed by the implementation, each of which will be briefly covered below.

All of the methods described here aim to solve the same equation, and it is where each of the techniques begins, the Schrödinger equation (eq. (1.3.4)). It has no simple solution though, and so different techniques are applied to reach a set of solutions - wavefunctions of the target molecule - and then calculate scattering observables from these wavefunctions. All of the methods here are *variational* methods, since they use variational calculus to reach their solutions. Three of the most popular methods to reach these solutions are the *Kohn* (Schneider and Rescigno, 1988; Rescigno et al., 1995; Winstead et al., 1992), and *Schwinger* (Takatsuka and McKoy, 1981, 1984), *variational principles*, and the ***R**-matrix method* (Wigner, 1946b,a; Wigner and Eisenbud, 1947), where the R-matrix method is the method used in this thesis, and is discussed in much more detail in the next section.

One of the defining aspects of electron scattering is that the the system can be left in a varietry of states after the scattering: these states - or scattering channels -

[1] Even for ground state studies it is common for the beam to contain some distribution of rotational states, usually arising from the temperature of the beam: electron scattering cross sections from the *ground state* are more accurately an average over the distribution of initial states of the target.

define the asymptotic boundary conditions of the problem. The Schwinger method; and the Kohn, and **R**-matrix, methods handle the boundary conditions in different ways. The Schwinger method is based on an integral approach, through which the correct asymptotic boundary conditions are automatically included, whereas the Kohn, and **R**-matrix, methods use trial wavefunctions, including the appropriate functions to represent the boundary necessary conditions (Resigno and Lengsfield III, 1995). It has been argued that this difference results in the **K**-matrices produced by the Schwinger method being one iteration better than those using the close-coupling approach (Takatsuka and McKoy, 1981), but it also has the disadvantage that the integral formalism requires that the integrals contain Green's functions[1], making them more complex than those of the Kohn and **R**-matrix methods (Truhlar et al., 2007). That the **R**-matrix method and the Kohn method were paired together here is no coincidence and in fact a particular version of Kohn's variational method, the *log derivative Kohn principal*, have been shown to be equivalent to the **R**-matrix method (Meyer, 1994). The main difference between the Kohn method and the **R**-matrix method is that the **R**-matrix method traditionally performs the inversion of the Hamiltonian via diagonalisation, whereas the Kohn log derivative method performs numerically simpler matrix inversion. For the Kohn method, the matrix inversions are simpler, but must be performed for every energy (Meyer, 1994; Rescigno et al., 1995) - this is not required for the **R**-matrix method, where the complicated solution to part of the problem is energy independent; this is especially useful when a fine energy grid is required, such as when examining resonance structures for example (see section 3.1.5).

How the above theories are implemented should not be important - two different implementations of the same theory should yield the same result. The only differences will be their various limitations. The implementation of the **R**-matrix theory used below is the *UK molecular **R**-matrix* (UKRmol) implementation (Carr et al., 2012). A limitation of this implementation, for example, is that only Abelian[2] point groups can

[1] Though there are methods of eliminating the integrals including the Green's function, but they either require replacing them with other - also complicated - integrals, or the choice of a special trial function(Truhlar et al., 2007).

[2] See chapter 2.

be used[1].

The final consideration here is the model examined, where different models are simply distinguished from one another by the levels of approximation made, and are discussed in detail in section 1.5. There are many comparisons between the different methods, many of which show the various methods agreeing - a promising result[2] - but there are also comparisons attempting to describe which methods are the most reliable, often however, the comparisons made are not completely justifiable since they compare results of different methods which have not used the same model (Takatsuka et al., 1981). Additionally, simply comparing the results of several methods applied to the same model may be misleading, as different approaches will not take the same length of time; an aspect of any calculation which should be considered.

Uncertainty Quantification

The need for *uncertainty quantification* (UQ) of theoretical results is becoming increasingly recognised, and recently Chung et al. (2016) have identified protocols for UQ in atomic and molecular structure calculations. However, as discussed by Chung et al. (2016), these methods are still in their infancy for scattering calculations and at present are only of use for relatively simple scattering problems, such as collisions with the one electron molecular hydrogen ion (Zammit et al., 2014). As far as electron collisions with methane go, we are not yet in a position to assign uncertainties to key processes, due to the major unquantified uncertainties remaining in the model. Thus, for example, the recent compilation of reccomended electron collision data for methane in Song et al. (2015) made extensive use of the results presented in this thesis. While they give recommended uncertainties for those processes which are well determined experimentally, they present no uncertainties for the various processes which rely on our, or indeed other, theoretical calculations.

[1] A previous implementation included a full symmetry treatment, but was limited to linear molecules (Noble et al., 1982; Noble, 1982).

[2] it is important to understand that just because several different theories agree with each other, this does not imply that the results are correct, as there may be defects in the common model

1.3 The R-Matrix Method

The equations governing these collisions typically allow for various approximations, depending on the scattering energy. For electron collisions, it is useful to divide the problem up into several smaller problems, where these approximations can be applied. These regions are the low-energy region, defined as that below the target species' ionization threshold, the intermediate-energy range, spanning the range directly below and above the ionization threshold, and the high-energy regime.

From a theoretical standpoint, the high-energy regime is the simplest region, since exchange interactions can be ignored. This means collisions can be approximated as being impulsive or modelled using perturbation theory, while still giving reliable results; the same is not true of the low and intermediate-energy ranges, where many subtle effects can influence the outcome of a collision.

In the low energy regime, in approximate order of increasing scattering energy, the following processes can be considered (Tennyson, 2010):

Elastic Scattering

$$\mathrm{AB} + e^- \rightarrow \mathrm{AB} + e^-$$

Rotational Excitation

$$\mathrm{AB}_{j''} + e^- \rightarrow \mathrm{AB}_{j'} + e^-$$

where j denotes the rotational states of the target.

Vibrational Excitation

$$\mathrm{AB}_{\nu''=0} + e^- \rightarrow \mathrm{AB}_{\nu'} + e^-$$

where ν denotes the vibrational states of the target, where typically $\nu'' = 0$, since at $T \sim 300$ K molecules are essentially in their ground state. The same is not true for the rotational states, where the target in an experiment will have a distribution of j''.

Dissociative electron attachment (DEA)

$$\mathrm{AB} + e^- \rightarrow \mathrm{A}^- + \mathrm{B}$$

Dissociative recombination

$$\mathrm{AB}^+ + e^- \rightarrow \mathrm{A} + \mathrm{B}$$

Electronic excitation

$$\mathrm{AB} + e^- \rightarrow \mathrm{AB}^* + e^-$$

Impact dissociation

$$\mathrm{AB} + e^- \rightarrow \mathrm{A} + \mathrm{B} + e^-$$

where in practice, this usually goes via an intermediate electronic excitation.

All of these processes share a common intermediary: AB^-. The **R**-matrix method is designed to obtain accurate wave functions for this intermediate species, allowing for all of the above to be calculated.

The **R**-matrix method is so named because it based about the goal of calculating the **R**-matrix, which in its simplest form can be described as:

$$\mathbf{F}(r_a) = \mathbf{R}(r_a, E) r_a \left.\frac{\mathrm{d}\mathbf{F}}{\mathrm{d}r}\right|_{r=r_a} \tag{1.3.1}$$

or

$$F_i(r_a) = \sum_j R_{ij}(r_a, E) r_a \left.\frac{\mathrm{d}F_j}{\mathrm{d}r}\right|_{r=r_a} . \tag{1.3.2}$$

That is, **R**-matrix relates the radial wave function, **F** to its derivative at a specific radius, r_a. The i and j subscripts in eq. (1.3.2) denote the specific channels of the system, the asymptotic states of the collision.

This can also be written for any radial distance;

$$\mathbf{R}(r, E) = \frac{\mathbf{F}(r)}{r\mathbf{F}'(r)} \tag{1.3.3}$$

where the $'$ represents a radial derivative. It is this definition of the **R**-matrix as the link between the radial function and its derivative *at this distance,* r_a, (eq. (1.3.1)) which dictates the basic step in the **R**-matrix method: the division of space into two regions (Burke and Berrington, 1993); an *inner* region, containing the wave function

of the N-electron target, and the *outer* region, containing only the scattering electron, with the scattering electron the only party free to exist in both regions.

1.3.1 History

Traditionally, *ab initio* calculation of the **R**-matrix was not possible, since it is defined by the complex physics of the system enclosed within the sphere, radius r_a, as defined in eq. (1.3.1), which were not known. For this reason, in the original formulation, no attempt was made to obtain solutions to the inner region problem (Wigner, 1946b,a; Wigner and Eisenbud, 1947; Kapur and Peierls, 1938). Instead, the **R**-matrix was parametrised on the boundary, and only the energy dependence of the outer region was studied. This approach was also used in atomic (Meyerhof, 1963), and then molecular (Fabrikant, 1985; Meyerhof and Laricchia, 1997; Humberston et al., 1997; Wilde et al., 1999; Hotop et al., 2004) physics.

The first *ab initio* **R**-matrix methods were developed for atoms (Burke et al., 1971; Burke and Robb, 1976; Burke, 1977). Later, *ab initio* formulations of the **R**-matrix method were developed to treat molecules, with Burke et al. (1977) building on the earlier work of Schneider (1975a,b); Schneider and Hay (1976). Early electron-molecule **R**-matrix codes, as implemented by Noble et al. (1982), were effectively limited to diatomic molecules, by the choice of *Slater Type Orbitals* (STOs). The move to using *Gaussian Type Orbitals* (GTOs), by Nestmann et al. (1991), to represent the target and continuum functions allowed general polyatomic **R**-matrix calculations to be carried out. This simplified all of the integrals, now having analytical solutions (however, the Gaussian tails extending outside of the **R**-matrix radius must still be subtracted). A recent advance in this area is the move to using B-splines to represent the continuum functions, enabling larger **R**-matrix radii, higher ℓ, and a more accurate representation of the wave function's tail, corresponding to an unbound particle (Mašín and Gorfinkiel, 2014).

In larger molecules, where an accurate *ab initio* solution is not yet possible, the **R**-matrix is still used to parameterize resonances(Hotop et al., 2004; Tarana et al., 2009).

1.3.2 Derivation

To begin with, it is important to point out that the **R**-matrix, as in eq. (1.3.3), is defined everywhere, but by separating space into the two regions, and defining the inner region as enclosing the entire charge cloud of the target, several useful identities can be made, allowing a definition of the **R**-matrix to be found on the boundary between these regions.

We start with the Schrödinger equation for an $N+1$ electron molecular system in the fixed nuclei approximation;

$$(\hat{\mathbf{H}} - E_k) \left|\Psi_k^{N+1}\right\rangle = 0. \tag{1.3.4}$$

In order to consider this in a finite volume - i.e. inside the sphere defined in eq. (1.3.1) - an extra term needs to be included to keep the Hamiltonian Hermitian, this is the Bloch operator, $\mathbf{L}_b$ (Bloch, 1957):

$$(\hat{\mathbf{H}} + \hat{\mathbf{L}}_b - E_k) \left|\Psi_k^{N+1}\right\rangle = \hat{\mathbf{L}}_b \left|\Psi_k^{N+1}\right\rangle, \tag{1.3.5}$$

$$\hat{\mathbf{L}}_b(b) = \sum_{i=1}^{N+1} \frac{\hbar^2}{2m_e r_a} \delta(r_i - r_a) \left(\frac{\mathrm{d}}{\mathrm{d}r_i} - \frac{b-1}{r_i}\right). \tag{1.3.6}$$

Where m_e is the electron mass, δ the dirac delta function, and b is an arbitrary constant, usually set to zero[1]. Equation (1.3.5) is the Schrödinger equation for $r \leqslant a$, which has the formal solution:

$$\left|\Psi_k^{N+1}\right\rangle = (\hat{\mathbf{H}} + \hat{\mathbf{L}}_b - E_k)^{-1} \hat{\mathbf{L}}_b \left|\Psi_k^{N+1}\right\rangle \tag{1.3.7}$$

which has the discrete solutions

$$\left\langle \Psi_k^{N+1} \right| \hat{\mathbf{H}} + \hat{\mathbf{L}}_b \left|\Psi_{k'}^{N+1}\right\rangle = E_k \delta_{kk'} \tag{1.3.8}$$

where, in this case, the Dirac notation implies integration is over the region defined by

[1] The **S**-matrix (or *scattering* matrix), discussed later, can be shown to be independent of the choice of b, even with a finite basis set(Meyer, 1994; Mori, 1972).

$r \leqslant a$, with the tails having been subtracted;

$$\int_0^{r_a} \mathrm{d}r = \int_0^{\infty} \mathrm{d}r - \int_{r_A}^{\infty} \mathrm{d}r \tag{1.3.9}$$

The eigenfunctions of this Hamiltonian, $\left|\Psi_k^{N+1}\right\rangle$, form a complete basis set inside this region. A solution to the Schrödinger equation, eq. (1.3.5), can be written in terms of these functions;

$$\Psi^{N+1} = \sum_k A_k(E)\Psi_k^{N+1} \tag{1.3.10}$$

The inner region basis functions are constructed using the close-coupling approximation (Arthurs and Dalgarno, 1960), and take the form:

$$\Psi_k^{N+1} = \mathcal{A}\sum_{ij} a_{ijk}\Phi_i^N(\mathbf{x}_1 ... \mathbf{x}_N)u_{ij}(\mathbf{x}_{N+1}) + \sum_i b_{ik}\chi_i^{N+1}(\mathbf{x}_1 ... \mathbf{x}_{N+1}) \tag{1.3.11}$$

which will be discussed in more detail below. Φ_i^N is the wavefunction of the i^{th} target state, and is itself represented by a sum over target configurations,

$$\Phi_i^N = \sum_m c_{im}\chi_m^N(\mathbf{x}_1 ... \mathbf{x}_N). \tag{1.3.12}$$

In eq. (1.3.11), a_{ijk} is the coefficient of the i^{th} target times the j^{th} continuum orbital in the k^{th} inner region wave function, b_{ik} the i^{th} L^2 configuration in the k^{th} inner region wave function. These are obtained by diagonalising the $N+1$ electron Hamiltonian. u_{ij} is the j^{th} continuum orbital associated with target state i, and $\chi_i^{N(+1)}$ is the i^{th} N(+1) electron L^2 CSF. The electrons in the scattering wavefunction must obey the Pauli principle, and are therefore anti-symmetrized by the operator $\mathcal{A}$. In eq. (1.3.12), c_{im} is the coefficient of the m^{th} *Configuration State Function* (CSF) in the i^{th} target wavefunction, which describes the distribution of electrons between orbitals and the associated spin-couplings. This will be discusses in more detail in the Inner Region section, page 25.

The continuum orbitals employed in eq. (1.3.11) are constructed as sets of Gaussians on the centre of mass, with coefficients chosen to replicate either Coulomb or Bessel functions (depending on the charge of the molecule) on the molecular centre of mass

(Faure et al., 2002). Originally, the continuum functions were contractions of GTOs, but these contractions were later replaced by just the GTOs as it was found to be more efficient. When a molecule has atoms away from its centre-of-mass, or at high energy where higher angular momentum states are accessible, the orbitals orbitals are generally speaking more complicated; representing these higher ℓ partial waves with a single centre expansion of GTOs would require increasingly large continuum basis sets which would quickly become untenable[1]. The solution to this is to include MOs not already included in the active space in the continuum basis set[2]. These are known as *virtual orbitals*.

On the **R**-matrix boundary, eq. (1.3.11) can be simplified, since the L^2 configurations have zero amplitude, and only the scattering electron can exist at $r = r_a$, so the second sum, and $\mathcal{A}$ both disappear. On the boundary:

$$\Psi_k^{N+1}\Big|_{r_a} = \sum_{ij} a_{ijk}\Phi_i^N u_{ij}(r_a) \tag{1.3.13}$$

One of the sets of variables required to generate the **R**-matrix are the boundary amplitudes, ω_{ik}, where the boundary amplitude of the k^{th} inner region function for the i^{th} channel is defined by the overlap integral

$$\omega_{ik}(r_a) = \left\langle \Phi_i^N Y_{\ell_i m_i} \Xi_{1/2} \,\middle|\, \Psi_k^{N+1} \right\rangle . \tag{1.3.14}$$

where $Y_{\ell m}(\theta, \phi)$ are the spherical harmonics, and ℓ, and m are the azimuthal and magnetic spin quantum numbers. $\Xi_{1/2}$ is the one electron spin function. This form is, in practice, not used, and instead it can be extracted from the definition of the inner region wavefunction on the boundary, eq. (1.3.13):

$$\omega_{ik}(r_a) = \sum_j u_{ij}(r_a) a_{ijk} \tag{1.3.15}$$

[1] This is limited by the integral codes anyway, and within the UKRMol codes the highest ℓ that has been used with GTOs is 5 (h). MolPro too is limited to $\ell \leqslant 7$. The diatomic (alchemy) codes compute these analytically, and have been used in calculations with $\ell = 8$ in the past, with no apparent reason not to be capable of going higher.

[2] This is the case only in *contracted* calculations, an alternative is to include the same orbitals in the L^2 configuration space - this approach is known as *uncontracted*.

Equation (1.3.15) also allows us to write the inner region wavefunction on the boundary in terms of the boundary amplitudes;

$$\Psi_k^{N+1}\Big|_{r_a} = \sum_i \Phi_i^N \sum_j u_{ij} a_{ijk} = \sum_i \Phi_i^N \omega_{ik}(r_a) \tag{1.3.16}$$

Returning to eq. (1.3.7), using the resolution of the identity:

$$\mathbb{1} = \sum_k |\Psi_k\rangle \langle\Psi_k| \tag{1.3.17}$$

and the result of eq. (1.3.8), we can write

$$\left|\Psi^{N+1}(E)\right\rangle\Big|_{r_a} = \sum_k \frac{\left|\Psi_k^{N+1}\right\rangle \left\langle\Psi_k^{N+1}\right| \hat{\mathbf{L}}_b \left|\Psi^{N+1}\right\rangle}{E_k - E}. \tag{1.3.18}$$

Where $\left|\Psi^{N+1}(E)\right\rangle$ is the full energy dependant wavefunction, and $\left|\Psi_k^{N+1}\right\rangle$ the wavefunctions for specific states. Then, expanding $\left|\Psi^{N+1}\right\rangle$ as in eq. (1.3.10) and $\left|\Psi_k^{N+1}\right\rangle$ as in eq. (1.3.16);

$$\left|\Psi^{N+1}\right\rangle = \sum_{jkmnp} A_j \frac{\omega_{mk}\omega_{nk}}{E_k - E} \left|\Phi_m^N\right\rangle \left\langle\Phi_n^N \,\middle|\, \Phi_p^N\right\rangle \hat{\mathbf{L}}_b \omega_{pj}. \tag{1.3.19}$$

but Φ_k^N are orthonormal, so $\left\langle\Phi_n^N \,\middle|\, \Phi_p^N\right\rangle = \delta_{np}$;

$$\left|\Psi^{N+1}\right\rangle\Big|_{r_a} = \sum_{jkmn} A_j \frac{\omega_{mk}\omega_{nk}}{E_k - E} \left|\Phi_m^N\right\rangle \hat{\mathbf{L}}_b \omega_{nj}. \tag{1.3.20}$$

On the boundary;

$$F_n(r_a) = \sum_j A_j \omega_{nj}(r_a) \tag{1.3.21}$$

where F_n is the *outer region* radial function. At the boundary however, this has to match with the target wavefunction. Rearranging eq. (1.3.19) and substituting in eq. (1.3.21) gives:

$$\left|\Psi^{N+1}\right\rangle\Big|_{r_a} = \sum_{km} \frac{\omega_{mk}}{E_k - E} \left|\Phi_m^N\right\rangle \sum_n \omega_{nk} \hat{\mathbf{L}}_b F_n \tag{1.3.22}$$

Then substituting in the definition of $\hat{\mathbf{L}}_b$ from eq. (1.3.6),

$$\left|\Psi^{N+1}\right\rangle = \frac{\hbar}{2m_e r_a}\sum_{km}\frac{\omega_{mk}}{E_k - E}\left|\Phi_m^N\right\rangle\sum_n \omega_{nk}\sum_{i=1}^{N+1}\delta(r_i - r_a)\left(\frac{\mathrm{d}}{\mathrm{d}r_i} - \frac{b-1}{r_i}\right)F_n. \quad (1.3.23)$$

giving:

$$\left|\Psi^{N+1}\right\rangle\Big|_{r_a} = \frac{\hbar}{2m_e r_a}\sum_{km}\frac{\omega_{mk}}{E_k - E}\left|\Phi_m^N\right\rangle\sum_n \omega_{nk}\left[r\frac{\mathrm{d}F_n}{\mathrm{d}r} - bF_n\right]\Bigg|_{r=r_a}. \quad (1.3.24)$$

On the boundary, $\left|\Psi^{N+1}\right\rangle$ has many forms, as in eqs. (1.3.10) to (1.3.13) and (1.3.16). Another is in terms of the outer region radial wave functions, F_i and target wavefunctions, $\left|\Phi^N\right\rangle$:

$$\left|\Psi^{N+1}\right\rangle = \sum_m F_m\left|\Phi_m^N\right\rangle, \quad (1.3.25)$$

which, gives

$$F_m = \frac{\hbar}{2m_e r_a}\sum_{kn}\frac{\omega_{mk}\omega_{nk}}{E_k - E}\left[r\frac{\mathrm{d}F_n}{\mathrm{d}r} - bF_n\right]\Bigg|_{r=r_a}. \quad (1.3.26)$$

Comparing eq. (1.3.26) to eq. (1.3.2), and setting $b = 0$ gives:

$$R_{mn}(r_a, E) = \frac{\hbar}{2m_e r_a}\sum_k \frac{\omega_{mk}\omega_{nk}}{E_k - E} \quad (1.3.27)$$

which is the standard expression for the **R**-matrix on the boundary (Tennyson, 2010). The same derivation is possible without actually definining the Bloch term, and can be found in Burke et al. (1971).

Clearly, there are singularities in the **R**-matrix for $E = E_k$, as a result, the eigenenergies are often referred to as **R**-matrix *poles*.

1.3.3 Inner Region

Building the parameters needed to construct the **R**-matrix is the main purpose of the inner region calculation, as it is used to give the scattering observables. The required values to generate the **R**-matrix are shown in eq. (1.3.27), the **R**-matrix pole positions, E_k, and the associated boundary amplitudes, ω_{ik}, of the inner region wavefunctions, Ψ_k^{N+1}. Within the inner region the interaction of the scattering electron with the target

is complicated: both correlation and exchange effects need to be considered in detail. The $N+1$ electron wavefunction in this region is generally written as eq. (1.3.11):

$$\left|\Psi_k^{N+1}\right\rangle = \mathcal{A}\sum_{ij} a_{ijk}\Phi_i^N(\mathbf{x}_1...\mathbf{x}_N)u_{ij}(\mathbf{x}_{N+1}) + \sum_i b_{ik}\chi_i^{N+1}(\mathbf{x}_1...\mathbf{x}_{N+1})$$

The UKRMol codes use a particularly efficient procedure for treating wavefunctions in this form (Tennyson, 1996a).

The additional orbitals, u_{ij}, are the only contribution to the inner region wavefuntion which are non zero at $r \geqslant a$, and so are the only possible contribution to the boundary amplitudes, w_{ij}, which is what allows eq. (1.3.15) to be used instead of eq. (1.3.14).

The second summation in eq. (1.3.11) involves configurations which have no amplitude on the **R**-matrix boundary and where all electrons are placed in orbitals associated with the target. Since they are confined to a finite volume of space they are often referred to as L^2 configurations. Such configurations allow for relaxation of the orthogonalisation between the continuum orbitals and those belonging to the target and are also used to model the effects of target polarisation. Which sets of configurations you include depend on the calculation in question; different models are discussed extensively below. L^2 configurations are generated for each these models by placing an extra electron (the scattering electron) in any of the orbitals specified subject to the constraints of occupancy and overall symmetry. Doing this requires care with the phase of the overall wavefunction (Tennyson, 1997).

In standard close-coupling treatments, the first summation over i in eq. (1.3.11) runs over the target electronic states included in the model. Given that even without considering the target continuum, there are an infinite number of target states to consider, this sum is always truncated. The ***R**-Matrix with Pseudo States* (RMPS) method (Bartschat et al., 1996) uses the properties of the **R**-matrix to try and create effectively complete close-coupling expansions. In terms of eq. (1.3.11), this is done by extending the sum over i to run over a set of pseudo-states. These states are designed to give a complete representation of all the target electronic states, including the continuum, up to some total energy but only within the confines of the R-matrix

sphere. In practice this is done by adding an extra basis set at the centre of the system; for molecules this involves an additional set of even-temperered GTOs (Gorfinkiel and Tennyson, 2004).

In addition to the energies of the poles, the multipole moments of the targets are needed, not for the construction of the **R**-matrix, but as they determine the long range potentials in the outer region;

$$V_{ij}(r) = \sum_{\lambda=0} \frac{\alpha_{ij}^{(\lambda)}}{r^{\lambda+1}} \tag{1.3.28}$$

where $\alpha_{ij}^{(\lambda)}$ is the asymptotic potential coefficient of order λ between channels i and j, defined as (Burke et al., 1977):

$$\alpha_{ij}^{(\lambda)} = \sqrt{\frac{2\ell_i + 1}{2\ell_j + 1}} C(\ell_i \lambda \ell_j; m_i m_\lambda m_j) C(\ell_i \lambda \ell_j; 000) Q_{ij}^{(\lambda)} \tag{1.3.29}$$

where ℓ_j is the orbital angular momentum of the scattering electron for the i^{th} channel, $C(\ell_1 \ell_2 \ell_3; m_1 m_2 m_3)$ is a Clebsch-Gordon coefficient, and $Q_{ij}^{(\lambda)}$ is the target moment between the i^{th} and j^{th} channels, where if $i = j$ it is a permanent moment, and if $i \neq j$ it is a transition moment.

1.3.4 Outer Region

In the outer region, since there is only one scattering particle, the physics is, compared to the inner region, simple. The wave function in this region can be written as:

$$\Psi^{N+1}(E) = \sum_{i=1}^{n} \Phi_i^N(\mathbf{x}_1 \dots \mathbf{x}_N) F_i(r_{N+1}) Y_{\ell_i m_i}(\theta, \phi) \Xi_{1/2} \tag{1.3.30}$$

where the sum is now over the n-channels of the problem.

Substituting eq. (1.3.30) into the Schrödinger equation gives a set of n coupled differential equations for the radial function, $F_i(r)$, (Burke et al., 1971):

$$\left[-\frac{\mathrm{d}^2}{\mathrm{d}r^2} + \frac{\ell_i(\ell_i + 1)}{r^2} - k_i^2 \right] F_i(r) = 2 \sum_{j=1}^{n} V_{ij}(r) F_j(r) \tag{1.3.31}$$

where V_{ij} is as in eq. (1.3.28). This means that the *outer region* calculation involves

solving these differential equations. In reality though, finding $F_i(r)$ is not required, and instead the **R**-matrix can be used. We already have a solution for the **R**-matrix, in eq. (1.3.2), but this is on the boundary. To obtain an energy dependant form, the **R**-matrix is propagated from the boundary out to some farther distance, $r = r_f$, beyond which, the non-Coulombic potential can be ignored (Burke and Noble, 1995; Morgan, 1984). There are several techniques for obtaining asymptotic solutions in the region for $r > r_f$ (Burke and Schey, 1962; Crees, 1980, 1981; Gailitis, 1976), with the most advanced being that of Gailitis (Gailitis, 1976; Noble and Nesbet, 1984). Propagation of the **R**-matrix in this way means that the wave function does not need to be defined in the region $r_a < r < r_f$.

The solution in the outer region can be written in terms of equations which are the same as for atoms, the calculations are simply more computationally demanding for molecules, as there is less symmetry, leading to degeneracies, and the long-range forces are considerably stronger, especially if the molecule has a large dipole. The larger long range forces require more terms in the partial wave expansion as it must be extended to higher ℓ, and the presence of a permanent dipole leads to coupling between channels differing in ℓ by one (Tennyson, 2010). Additionally, strongly polar molecules require the rotational motion be taken into account; this is dealt with using approaches based on a frame transformation (Lane, 1980), and through the use of the *Adiabatic Nuclear Rotation* (ANR) approximation, with a Born correction (Baluja et al., 2000) to account for contributions from the higher ℓ partial waves.

Additionally, we need the wavenumber of the scattering electron for the i^{th} asymptotic channel;

$$k_i^2 = 2(E - E_i^{(N)}) \tag{1.3.32}$$

where, by convention, $E - E_i^{(N)}$ is the difference in the energy of the scattered electron, and that of the lowest target state. Channels are described as being *open*, or *closed* depending on whether k_i^2 is positive or negative (respectively). For a normalised wave

function, the outer region solutions asymptotically approach the following results:

$$\lim_{r\to\infty} F_{ij}(r) = \begin{cases} {}^{1}/_{\sqrt{k_i}}\ (\delta_{ij}\sin\theta_i + K_{ij}\cos\theta_i) & \text{if } E_i \geqslant 0 \\ 0 & \text{otherwise} \end{cases} \tag{1.3.33}$$

where θ_i is the channel angle;

$$\theta_i = \begin{cases} k_i r - {}^{1}/_{2}\ \ell_i\pi & \text{Neutral target} \\ k_i r - {}^{1}/_{2}\ \ell_i\pi - \eta_i \ln(2k_i r) + \sigma_i & \text{for } Z - N \neq 0 \end{cases} \tag{1.3.34}$$

and

$$\eta_i = \frac{Z-N}{k_i}$$
$$\sigma_i = \arg(\Gamma(1+\ell_i+i\eta_i)).$$

σ_i is sometimes referred to as the *Coulomb phase*. The important quantity here is the **K**-matrix, a symmetric matrix with dimension n, the number of open channels.

At r_f, where the propagated **R**-matrix have been propagated out to a sufficient radius such that the coupling potentials to be negligible, the solutions are matched to Coulomb or Bessel functions (Collins and Schneider, 1983). This matching defines the **K**-matrix. The radius at which the coupling potentials are negligible can be very large, analytic solutions to the integrals have been proposed in order to reduce the radius required to apply the matching procedure (Burke and Schey, 1962; Burke et al., 1964; Gailitis, 1976). The **K**-matrix can be obtained for $r_a < r = r_b < r_f$. The **K**-matrix holds all of the information required to compute scattering observables, and is defined in eq. (1.3.37) below.

Looking back to eq. (1.3.33), for open channels;

$$\lim_{r\to\infty} F_{ij}(r) = {}^{1}/_{\sqrt{k_i}}(\delta_{ij}\sin\theta_i + K_{ij}\cos\theta_i)$$

where these are the solutions to the differential equations of eq. (1.3.31). The two parts

of F_{ij} are the regular, and irregular solutions to these differential equations, $F_{ij}^{(C)}$ and $S_{ij}^{(C)}$, respectively;

$$F_{ij} = F_{ij}^{(C)} + F_{ij}^{(S)}$$

$$\lim_{r\to\infty} F_{ij}^{(C)}(r) = {}^{1}/_{\sqrt{k_i}}\ \delta_{ij} \sin\theta_i \tag{1.3.35}$$

$$\lim_{r\to\infty} F_{ij}^{(S)}(r) = {}^{1}/_{\sqrt{k_i}}\ K_{ij} \cos\theta_i \tag{1.3.36}$$

The **K**-matrix contains the asymptotic solutions, and K_{ij} is the element coupling the channels i and j. It can be defined as (Noble and Nesbet, 1984):

$$\mathbf{K} = -\left(\mathbf{F}^{(C)} - \mathbf{R}\mathbf{F}'^{(C)}\right)^{-1}\left(\mathbf{F}^{(S)} - \mathbf{R}\mathbf{F}'^{(S)}\right)\Big|_{r=r_b} \tag{1.3.37}$$

where **R** is the **R**-matrix at $r = r_b$, $\mathbf{A}'$ denotes a generalised derivative;

$$\mathbf{A}' = r_b \left.\frac{\mathrm{d}\mathbf{A}}{\mathrm{d}r}\right|_{r=r_b} \tag{1.3.38}$$

Many of the other scattering matrices, and observables are defined in terms of the **K**-matrix. The *scattering*, or **S**-matrix;

$$\mathbf{S} = \frac{\mathbb{1} + i\mathbf{K}}{\mathbb{1} - i\mathbf{K}} \tag{1.3.39}$$

and the eigenphase sum, δ_{ii}^{D};

$$\delta(E) = \sum_i \mathrm{atan}(K_{ii}^{D}) \tag{1.3.40}$$

Where K_{ii}^{D} are the eigenvalues of the **K**-matrix. Eigenphases are very useful for diagnosing potential problems with calculations, studying the convergence of calculations, and comparing different models. Examples of this can be seen in figs. 2.9, 2.16, 3.15, 3.17, 3.19 and 3.21.

There is also the **T**-matrix, or *transition*-matrix, with a simple relation to the **S**-matrix;

$$\mathbf{T} = \mathbf{S} - \mathbb{1} \tag{1.3.41}$$

which can be thought of as $\mathbf{S}$ in the absense of all interactions. The definition of $\mathbf{T}$ has differing phase factors under different conventions, with no universal agreement. In Taylor (1972), for example, the convention used has $\mathbf{S} = \mathbb{1} - 2\pi i\mathbf{T}$.

1.4 UKRmol R-Matrix method implementation

1.4.1 Inner Region

As mentioned previously, the inner region is all about calculating eq. (1.3.11), and the various coefficients involved, and a smaller number of additional quantities. Looking back to eq. (1.3.11);

$$\left|\Psi_k^{N+1}\right\rangle = \mathcal{A}\sum_{ij} a_{ijk}\Phi_i^N(\mathbf{x}_1...\mathbf{x}_N)u_{ij}(\mathbf{x}_{N+1}) + \sum_i b_{ik}\chi_i^{N+1}(\mathbf{x}_1...\mathbf{x}_{N+1})$$

and breaking down the various parts into their components; first we have eq. (1.3.12), the target wavefunctions;

$$\Phi_i^N = \sum_m c_{im}\chi_m^N(\mathbf{x}_1...\mathbf{x}_N)$$

where $\chi_i^{N(+1)}$ in eqs. (1.3.11) and (1.3.12) are the $N(+1)$ L^2 configurations;

$$\chi_m^N = \sum_n d_{mn}\xi_n \tag{1.4.1}$$

$$\chi_i^{N+1} = \sum_n f_{in}\xi_n. \tag{1.4.2}$$

Here we have introduced ξ_n, the n^{th} *Molecular Orbital* (MO), which is just a *Linear Combination of Atomic Orbitals* (LCAO);

$$\xi_n = \sum_p g_{np}\zeta_p \tag{1.4.3}$$

where ζ_p is the p^{th} atomic orbital, or basis function. The basis sets used by the *polyatomic UKRmol codes* are GTOs, where each basis function is described as such (having dropped the subscript p notation to differentiate between seperate basis functions, and

instead defining a single basis function for a specific ℓ):

$$\zeta_\ell = R_\ell(r) T_{\ell m}(\theta, \phi) \tag{1.4.4}$$

where $T_{\ell m}(\theta, \phi)$ are the *Tesserel Harmonics*, or *Real Spherical Harmonics*. The radial part for a GTO, $R_\ell(r)$ is

$$R_\ell(r) = r^\ell \sum_q c_q A(\ell, \alpha_q) e^{-\alpha_q r^2} \tag{1.4.5}$$

where $A(\ell, \alpha_q)$ is a normalization constant, given in eq. (1.7.2). $R_\ell(r)$ is a contraction of several GTOs, since GTOs do not have the correct shape at the nucleus. c_q is the contraction coefficient, and α_q is the exponent. q here distinguishes between the different primitive exponents in the basis set.

The coefficients in the equations above, a_{ijk}, b_{ik}, c_{im}, d_{mn}, f_{in}, g_{np}, c_p and α_p are all either direct inputs, or are the variables being calculated in the inner region, and the approach to doing so is outlined below and in fig. 1.1.

There are eleven inner region programs used in a standard UKRmol calculation. The first six come from five routines of the Sweden-Molecule quantum chemistry suite of Almlöf and Taylors (1984); `swmol3`, `sword`, `swjkf`, `swscf`, `swtrmo`, and the additional routine, `swedmos` of Morgan et al. (1997). These programs take the molecular geometry and basis functions as input, and provide orthogonalised *Hartree Fock self consistent field* (HF-SCF) molecular orbitals, and one and two electron integrals, i.e. they provide the ξ_n of eqs. (1.4.1) to (1.4.3).

In more detail; `swmol3` creates the atomic orbitals, and calculates the one and two electron integrals between the various atomic orbitals - the molecule orbitals created later are linear sums of these atomic orbitals, so their overlap integrals are just sums of atomic orbital overlap integrals.

`swfjk` generates combinations of Coulomb and Fock matrix integrals, used by `swscf` to create the target MOs by performing the Hartree-Fock self consistent field optimisation.

`swedmos` orthogonalises the orbitals. It takes two sets of orbitals, and returns them,

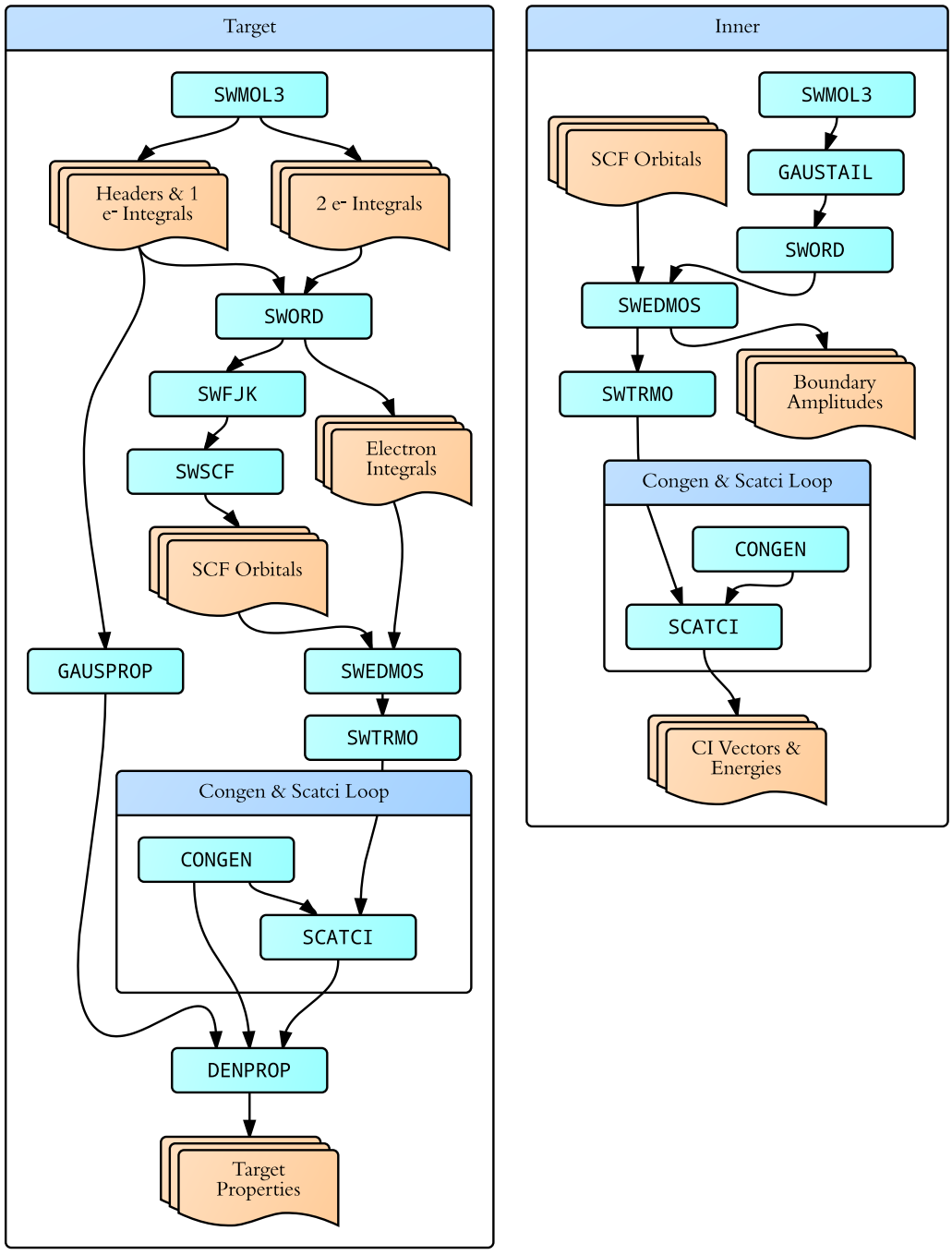

Figure 1.1: Simplified input/output and program flow for the inner region. Turquoise rectangles represent the various routines of the inner region, and orange stacks are important files. The three important sets of data for the outer region are the *Target Properties*, the *Boundary Amplitudes*, and the *CI Vectors & Energies*.

each orthogonal amongst themselves, and occupying their own orthogonal spaces. The *occupied* orbitals which come out of `swscf` are orthogonal, but the *virtual orbitals* are not orthogonal to them. Likewise, for the $N+1$ problem, the virtual orbitals have already been orthogonalised to the occupied orbitals, but the continuum orbitals have not. A standard orthogonalisation technique is the Gram-Schmidt process, where each vector has its projection onto each of the previous vectors (which have already been orthogonalised) subtracted from itself. This process is numerically unstable though, and linear dependence can cause issues. For the virtual orbitals, this is rarely a problem, and they are Schmidt orthogonalised. However, for practical purposes the continuum functions are often over complete when added to the target, i.e. somewhat linearly dependant; removing Gram-Schmidt orthogonalisation as an option. Instead, the vectors are first Gram-Schmidt orthogonalised one by one onto the original target vectors (i.e. not with each other). Then Löwdin's symmetric scheme (Löwdin, 1950) is used to orthogonalise them amongst themselves, with orbitals corresponding to small eigenvalues in the overlap matrix being deleted. *Small* here corresponds to less than a certain deletion threshold, provided to `swedmos` via its namelist, selecting an appropriate deletion threshold is not simple, and over vigilant culling of orbitals can lead to an incomplete representation of the continuum (Tennyson, 2010), this is demonstrated in fig. 2.16. After this process the whole orbital set is orthogonal.

The two unmentioned modules are less entwined with the production of the coefficients in eqs. (1.4.1) to (1.4.3), and more related to the specific implementation of the sweden-molecule codes. `sword` orders the integrals produced by `swmol3`, and and `swtrmo` performs the four-index transform. All the names of these routines come from a combination of the actions they provide, and the maximum variable name length of six characters - part of the fortran 66/77 specification.

The above mentioned routines are common to both the N, and $N+1$ electron problems. There are five more programs not mentioned yet, two of which are `gausprop` and `gaustail`. `gausprop` calculates the property integrals, required by `denprop`, and `gaustail` evaluates the integrals of the tails of the continuum orbtials, $\int_{r_a}^{\infty} u_{ij}(r)\mathrm{d}r$,

and the two electron integrals:

$$\langle u_i(\mathbf{r}_1)\eta_j(\mathbf{r}_2)|\,{}^1\!/_{|\mathbf{r}_1-\mathbf{r}_2|}\,|u_k\mathbf{r}_1)\eta_l(\mathbf{r}_2)\rangle\,.$$

These are not calculated using a modified version of the sweden integral codes, but rather by subtracting from integrals over all space, with several optimisations made to limit the number of integrals that need to be calculated(Morgan et al., 1997); for example, since all electrons but the scattering electron are limited to be inside the **R**-matrix sphere, one orbital must be a target orbital, and the other a continuum orbital.

The next step in fig. 1.1 is the *congen & scatci loop*, where the loop is over each of the molecular symmetries.

`congen` generates the configurations $\chi_n^{N(+1)}$, based on various rules provided, giving the d_{mn} and f_{in} of eqs. (1.4.1) and (1.4.2). This is an important part of the calculation, as the set of configurations used is one of the defining characteristics of a given model.

`scatci` takes the configurations generated by `congen`, constructs, and then diagonalises the Hamiltonian. Traditionally, this was the longest stage to a calculation, but thanks to upgrades in the last few years to parallelise the code, making use of the standard linear algebra package PARPACK (Maschhoff and Sorensen, 1996), and substantial increases in cpu speed, is sometimes usurped as the most expensive area of calculation by the outer region routines - purely due to their serial nature[1]. The Hamiltonians here can become very large, and since the problems requires that these Hamiltonians are diagonalised, they must be loaded into memory, requiring machines with very large quantities of RAM. The quantities calculated here are the eigen energies, and vectors, i.e. E_k, a_{ijk}, and b_{ik} of eqs. (1.3.8) and (1.3.11).

The last unmentioned routine, `denprop`, calculates the density matrices, and wavefunction properties. The wavefunction properties for pairs of wavefunctions are used to give the asymptotic potential via the $\alpha_{ij}^{(\lambda)}$ coefficients, as in eqs. (1.3.28) and (1.3.29). A heavily modified version of this code exists for calculating the necessary parameters

[1]Though this is now in the process of being dealt with too, with parallel outer region codes being developed (Sunderland et al., 2002, 2009; Burke et al., 2002).

for photoionization cross sections exists too, and is discussed in detail in section 3.1.4, page 92.

1.4.2 Outer Region

This is where the majority of the experimental observables are computed. The structure of the outer region programs is slightly different from that of the inner region, with all of the required subroutines being compiled into a single executable, with the ability to easily select which modules are required simply by commenting out lines in the main program file[1]. The main programs, and a general overview of the structure of an outer region calculation are shown in fig. 1.2.

The naming scheme for the outer region routines is very similar to that of the inner region. `swinterf` provides an interface between the inner and outer regions. It includes the *sw* prefix because traditionally, either the Alchemy quantum chemistry suite(McLean et al., 1991), or the Sweden suite were used in the inner region; the *sw* indicated that this version was for the Sweden codes. This program takes the target properties, boundary amplitudes, and eigen energies and vectors, and creates two files. The first file contains a description of the model in terms of the target properties, channel quantum numbers, and symmetry. The second file contains the parameters required to construct the **R**-matrix and the coefficients of the multipole expansion for the long range potentials. This is all the information required to calculate the remaining scattering observables, and is considerably more compact than the inputs requires to generate it.

Next, we have `rsolve`. This is the main part of the outer region calculation, and the most time consuming step. It also benefits heavily from parallelisation, as seen in the parallel versions of the outer region codes of Sunderland et al. (2002, 2009) and Burke et al. (2002). `rsolve` is where the energy dependence of the problem is finally introduced; it generates the energy dependant **K**-matrices. This is done by propagating the **R**-matrix out to some radius (Morgan, 1984), at which point it is matched to an

[1] Although this is merely an implementation detail, and it would be very possible to compile each subroutine with a wrapping program and then call each routine individually, which may be desirable if intermediary files need to be altered before the calculation continues.

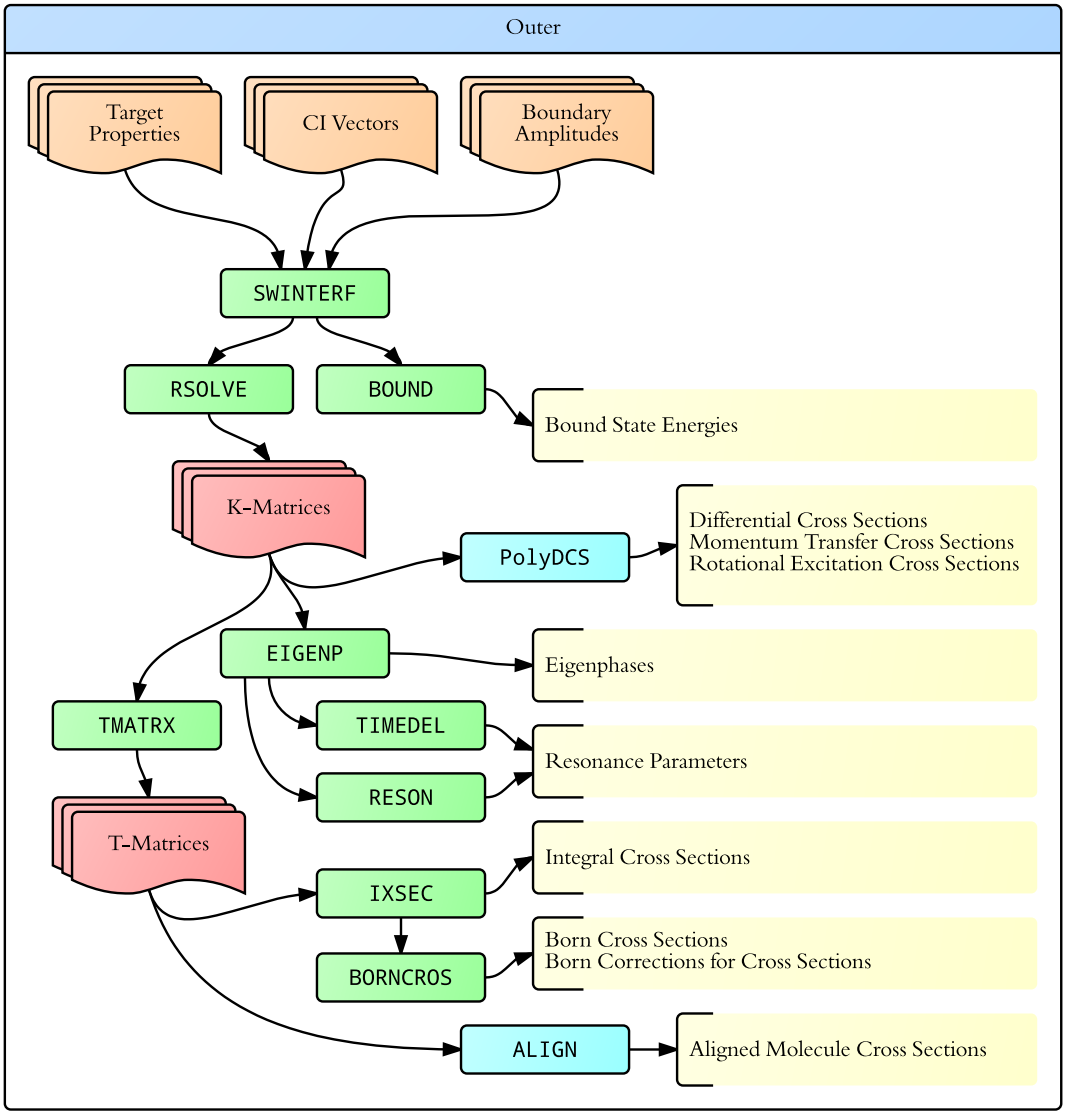

Figure 1.2: Simplified input/output and program flow for the outer region modules. Turquoise rectangles represent the various programs of the outer region, green rectangles are subroutines of the modular outer region program, orange stacks are important input files coming from the inner region calculation, and red stacks are important intermediary files created, which can be extracted and used as inputs for other programs (although sometimes the exact formatting of the file may need to be altered).

asymptotic expansion (Noble and Nesbet, 1984), where the **K**-matrix can be obtained using a standard formula, as in eq. (1.3.37).

`bound` is used to give bound state wavefunctions, and does so by calling `rsolve` with bound state boundary conditions according to algorithms originally developed for finding the bound states of atoms (Sarpal et al., 1991; Rabadán and Tennyson, 1996). It gives the B_{ik} coefficients described in eq. (3.1.17),

$$\Phi_i^N = \sum_k B_{ik} \psi_k^{(N)}$$

The **K**-matrices are used by several routines, and can also be used by external programs. Inside the UKRmol codes, they are the input for `eigenp`, which provide the eigenphases by taking the arctan of their eigenvalues, as in eq. (1.3.40). `timedel` (Stibbe and Tennyson, 1998) and `reson` (Tennyson and Noble, 1984) then find resonances, using the time delay method (Stibbe and Tennyson, 1996), and by attempting to fit Breit-Wigner profiles to the eigenphase sums, respectively.

`tmatrx` takes the **K**-matrices, and uses standard formulae to give the **T**-matrices, which are then used by `ixsec` to give integral cross sections. `borncross` calculates born cross sections, and also gives a Born correction for the cross sections. Cross sections of species with dipoles converge slowly with partial waves, and so a correction to make up for the omitted states with $\ell > \ell_{\max}$ (where $\ell_{\max}$ is typically 4) is applied (Chu and Dalgarno, 1974; Baluja et al., 2000).

`PolyDCS` and `Align` are seperate programs, of Sanna and Gianturco (1998) and Harvey (2010), respectively. They are both discussed thoroughly in the sections 3.1.2 and 3.1.3, below (pages 88 and 91).

1.5 Model Classification

There are several important aspects to describing a model in an **R**-matrix calculation: ranging from simpler decisions, such as the basis set used, or the method by which the orbitals were obtained, and how many of these orbitals to include in the active space; to more involved inputs, such as the set of configurations to include in the wave-

functions. Models are typically divided into different families based on the selection criteria describing the CSFs included in the *Configuration Interaction* (CI) part of the calculation, where including different sets of CSFs provide the necessary interactions for modelling different physical aspects of the molecule.

Below, several of the more common schemes are described, by describing the χ_i^{N+1} and χ_m^N terms in eqs. (1.3.11) and (1.3.12),

$$\Psi_k^{N+1} = \mathcal{A} \sum_{ij} a_{ijk} \Phi_i^N(\mathbf{x}_1 ... \mathbf{x}_N) u_{ij}(\mathbf{x}_{N+1}) + \sum_i b_{ik} \chi_i^{N+1}(\mathbf{x}_1 ... \mathbf{x}_{N+1})$$

$$\Phi_i^N = \sum_m c_{im} \chi_m^N(\mathbf{x}_1 ... \mathbf{x}_N).$$

Including different configurations in the model allows the representation of different types of resonance, the two main resonance processes being *shape* type, and *Feshbach* resonances. The first type, the shape resonance, can be thought of as scattering electron occupying the *Lowest Unoccupied Molecular Orbital* (LUMO). Shape resonances are generally short lived, resulting in relatively broad features.

The other main resonance type, the Feshbach resonance, is the simultaneous excitation of the target, and capture of the scattering electron, with the excited state known as the parent state. Feshbach resonances are particularly important for positive ions, since there is an infinite Rydberg series of resonances for each value of (ℓ_i, m_i), and each electronically excited state of the target. These resonances have relatively long lifetimes, resulting in narrow features in the scattering observables.

A third type of resonance, a *core excited shape* resonance also exists, closely related to the Feshbach resonance. In a Feshbach resonance, the scattering electron is trapped at an energy just below that of the parent state - a core excited resonance occupies an orbital just above that of the parent state. The core excited resonance is much rarer than a Feshbach resonance, and it is difficult to tell one from the other without additional investigation. Like Feshbach resonances, these too have long lifetimes, and so narrow resonance features.

A final class of resonances, the *pseudo* resonance also exists. As the name suggests,

these are not true resonances; but an artefact of an incomplete model. It is often impractical to include all of the channels in the outer region, and so after some arbitrary cut-off energy, additional channels can be removed from the model. Above this energy, pseudo-resonances occur where an omitted channel opens, and occur as sharp features. These features can be smoothed over (Gorfinkiel and Tennyson, 2005; Meyer et al., 1995), but the result is only an approximation. Generally speaking they are a problem best avoided.

1.5.1 Static Exchange

This is the special case where only the ground state occupied orbitals are included in the active space, yielding only one target configuration, χ_m^N. In this case, there is only one target wavefuntion, so there is no sum over i in the first sum of eq. (1.3.11).

A *Static Exchange* (SE) model cannot model electronic excitation, and so cannot model the parents states preceding Feshbach and core excited shape resonances. Only shape resonances are given by an SE model. It is also unable to model the polarisability of the target using the *sum over states* (SOS) method used in the UKRmol suite, this is discussed in section 2.1.2.

Despite these shortcomings, the SE model has its uses. At high energy, where other models would be plagued by pseudo-resonances, an SE model shows none, as there are no channels for the omitted ones to couple to; and being a rigorously defined model, it can be used to compare different methods. It is also a very simple model, and so typically very fast, serving as a good base from which to build a larger model.

1.5.2 Complete Active Space Configuration Interaction

At the other end of the scale, is the *Complete Active Space Configuration Interaction* (CAS-CI)[1] model. This model includes additional orbitals in the active space above the ground state, where all possible configurations are included in χ_m^N and χ_i^{N+1}. The static exchange model can be thought of as the special case of CAS-CI, where no additional

[1]The *CAS* section of this acronym, *Complete Active Space*, is itself used to describe the set of all configurations described by a set of orbitals

orbitals are included.

The treatment of electronic excitation necessarily involves using target wavefunctions determined using *Configuration Interaction* (CI) based procedure. Use of a CAS-CI representation of the target has certain advantages when balancing the N and $N+1$ electron calculations (Tennyson, 1996b), since the target and scattering calculations are represented with equivalent levels of approximation. A CASCI target wavefunction includes all possible CSFs generated using a given orbital set and can be described as:

$$[\mathrm{CAS}]^N.$$

It is often both impractical and unnecessary to include *all* of the configurations, and electrons in core orbitals can be frozen,

$$[\mathrm{core}]^n[\mathrm{CAS}]^{N-n},$$

where n electrons are frozen in $^{\mathrm{n}}/_2$ core orbitals and the remaining $(N-n)$ target electrons are distributed freely across a set of suitably selected valence orbitals.

There exist several types of CI calculation, described by the number of electron excitations allowed, CI described above is *full* CI. That is, all configurations are included, regardless of how many electrons must be excited to reach them. Including all configurations is obviously computationally expensive, and so some scheme to remove CSFs less likely to contribute to the model is always useful. One such scheme is to limit the number of electrons allowed to excite to other orbitals. Such models employing these schemes are known by the acronyms CIS, CISD, CISDT, etc. where S, D, and T stand for single, double, and triple excitations. In this nomenclature, the models increase in size as (SE,) CIS, CISD, . . . , full CI. These models are described with active spaces as in table 1.1:

The remaining models are, necessarily, somewhere in-between SE and full CI, but not necessarily on the scale of models in table 1.1.

Table 1.1: Occupation of orbital sets for various CI models included differing numbers of excited electrons. Each model is represented by a row *and all of the previous rows.*

Core	Ground State Orbitals	Excitation Orbitals	Model name	Balance
n	$N-n$	0	SE	n/a
n	$N-n-1$	1	CI S / SEP	Least Ballanced
n	$N-n-2$	2	CI SD	
n	$N-n-3$	3	CI SDT	
		$\vdots$		
n	0	$N-n$	Full CI	Balanced

1.5.3 Static Exchange plus Polarisation

The smallest advance above the SE model is to include single excitations. The *Static Exchange plus Polarisation* (SEP) model allows single excitations from the ground state into some arbitrarily larger set of orbitals, modelling polarisability by exciting a target electron into a virtual orbital while also occupying another virtual orbital with the scattering electron. This is equivalent to the CIS model, in the special case where the configurations do not interact with the target state. Brillouin's theorem (McWeeny, 1989) shows that this is the case for single excitations from a Hartree-Fock wave function.

CAS-CI models are, by definition balanced; by this we mean that all configurations are included, and the N-electron target, and $N+1$-electron scattering calculation are treated equally. SEP models on the other hand are arguably not balanced (Tarana and Horáček, 2007). A summary of the relative levels of balance of different models can be seen in table 1.1. They do however provide a means of modelling the polarisability of the molecule, as well as, to some extent, Feshbach resonances.

1.5.4 Multi Reference Configuration Interaction

A step up from the CIS(D,T,etc.) models are *Multi Reference Configuration Interaction* (MRCI) models, where instead of only allowing excitations from the ground state, a

smaller active space is chosen, from which excitations are allowed. The nomenclature for these models is the same as for CI models, with MRCIS, MRCISD, MRCISDT, etc. being models including several reference configurations, and then all configurations reachable within the limited number of electron excitations. These models can be described in a similar way to the CI models, and are shown in table 1.2

Table 1.2: Occupation of orbital sets for various MRCI models included differing numbers of excited electrons. Each model is represented by a row *and all of the previous rows*.

Core	Reference States' Orbitals	Excitation Orbitals	Model name	Balance
n	$N-n$	0	n/a[a]	n/a
n	$N-n-1$	1	MRCI S	Least Balanced
n	$N-n-2$	2	MRCI SD	
n	$N-n-3$	3	MRCI SDT	
		$\vdots$		
n	0	$N-n$	Full CI	Balanced

[a] While this may at first appear to be a full CI model of the smaller active space defined by the *Reference States' Orbitals*, it is not, the continuum orbitals will have been orthogonalised to the unused excitation orbitals, giving an incomplete continuum representation.

Two important things to note about the models described in table 1.2 are firstly, that when all sets of excitations are included, the model essentially becomes a full CI calculation over the full set of orbitals. And second, noting the first model, while this may at first appear to be a full CI calculation of the smaller active space defined by the *Reference States' Orbitals*, it will not be, since the continuum orbitals will have been orthogonalised to the *Excitation Orbitals*, leaving a large gap in the representation of possible states of the molecule.

All of the above models use the same orbital set created solely for the target, simply using higher and higher orbitals to augment the active space. There are also models which use orbitals designed to represent particular physics of the problem. Two such model is described below.

1.5.5 Rydberg Model

While typically Rydberg orbitals are associated with atoms, they are found in molecules too; when the orbitals have high principal quantum numbers. When the electronic excitations are into Rydberg like orbitals, or where the molecule is known to have a Rydberg like behaviour, it is appropriate to augment the basis set with functions capable of describing these diffuse Rydberg states being included on the center of mass (Cooper and Kirby, 1987; Tennyson, 1996b; Rozum et al., 2003).

The choice of configurations is secondary, and it is the creation of the orbitals using diffuse functions for modelling the Rydberg states which defines this model.

1.5.6 R-matrix with Pseudo States

The Rydberg model predates the development of the ***R**-matrix with Pseudo States* (RMPS) method (Madden et al., 2011; Gorfinkiel and Tennyson, 2005). In fact the two procedures have some similarities since the RMPS method involves using the same CSFs as in the Rydberg model, but uses a distinct basis set for the RMPS orbitals - a set of even-tempered GTOs place on the molecular centre-of-mass. The aim here is to fill up all the space inside the **R**-matrix sphere, representing the Rydberg states leading up to ionization and continuum of states, found above the ionization limit, with this sphere.

A problem with this method is that it adds a third, notionally complete, basis set. This of course can cause problems with linear dependence, especially if any of the atomic centres are on the centre of mass.

Both this model and the Rydberg model use the same CSFs as the MRCIS model, only utilising different orbitals, designed to model particular physics of the problem

1.6 Additional Considerations

There are a few additional input parameters which also require care, which are not isolated to a single model type, but still have important implications that need to be taken into account in any calculation.

When discussing `swedmos`, *virtual orbitals* were mentioned. These are additional, unoccupied, target orbitals, which are used to augment the continuum basis set, and provide a means to represent higher ℓ partial waves without including higher ℓ terms in the continuum basis set. Typically, at least one virtual orbital is included for each symmetrically non redundant atom off the centre of mass. In methane, this would mean a minimum of 2 virtual orbitals would normally be included (in the C_{2v} representation used). If the virtual orbitals are contracted, this is, in effect, adding more u_{ij} to eq. (1.3.11);

$$\left|\Psi_k^{N+1}\right\rangle = \mathcal{A}\sum_{ij} a_{ijk}\Phi_i^N(\mathbf{x}_1...\mathbf{x}_N)u_{ij}(\mathbf{x}_{N+1}) + \sum_i b_{ik}\chi_i^{N+1}(\mathbf{x}_1...\mathbf{x}_{N+1}).$$

When the size of the active space is increased, it is simply increasing the number of configurations, χ_i^{N+1}, which means that the same orbitals and configurations are included, i.e. both methods end up including the same configurations. For this reason, virtual orbitals are less important when the number of orbitals included in the CAS is increased. Every additional orbital included also contributes to the problem of linear dependence, and so if there are already many orbitals in the active space, then the improvement found by including virtual orbitals will be lessened, while still increasing the risk of problematic linear dependence.

1.7 Basis Sets

Equation (1.4.5) describes the radial part of a GTO with the coefficients c_q and α_q. Including the dropped p subscript of eq. (1.4.5), we have

$$R_{p\ell}(r) = r^\ell \sum_q c_{\ell pq} A(\ell, \alpha_q) e^{-\alpha_{\ell q} r^2}, \tag{1.7.1}$$

each basis set is made up of a set of exponents for each ℓ, $\alpha_{\ell q}$, and coefficients defining the contractions to create the individual basis functions. The normalisation coefficient,

A, is a function of ℓ and α_q, such that $\int |R_{p\ell}(r)|^2 \, \mathrm{d}r = 1$:

$$A(\ell, \alpha_q) = \sqrt{\frac{\left(2\alpha_q/\pi\right)^{3/2} \left(4\alpha_q\right)^{\ell}}{(2\ell - 1)!!}} \tag{1.7.2}$$

The original basis functions were devised by Slater, giving the functions describing atomic orbitals, known as STOs. The main body of an STO is an inverse exponential - and calculating overlap integrals between STOs is difficult. Overlap integrals between GTOs can be done analytically, but GTOs do not have the same shape as STOs, see fig. 1.3, and so sums of Gaussians are created to approximate STOs.

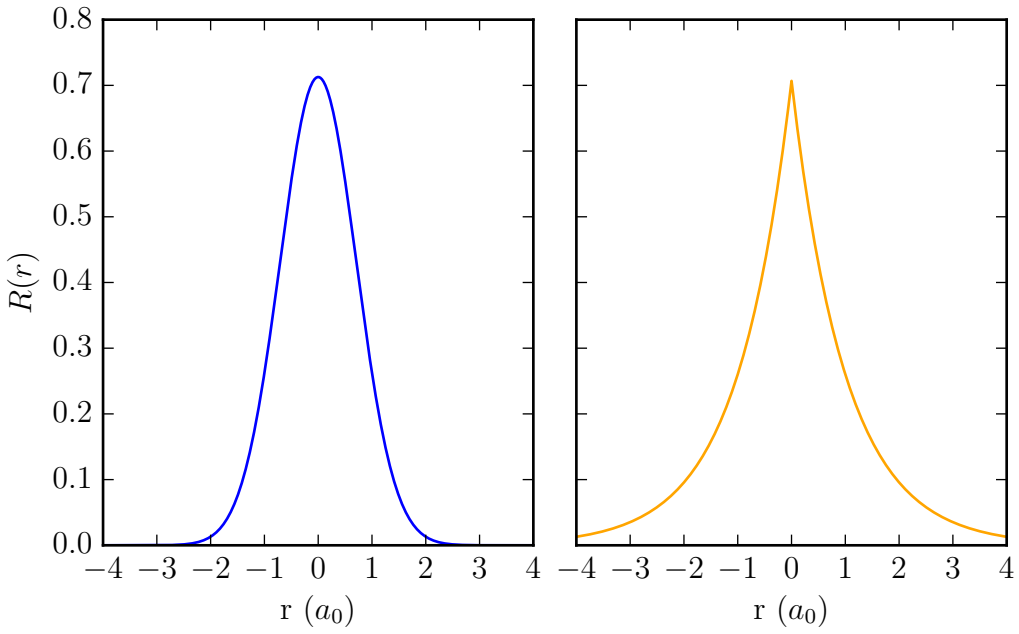

Figure 1.3: Comparison of Gaussian and Slater type function shapes. ■, GTO; ■, STO.

For example, the coefficients and exponents of the 3-21G basis set[1] are given in table 1.3, and the functions these define in table 1.4.

This is just one of many many basis sets, each with their own obscure name - there are several nomenclature systems used, depending on the creator of the basis set, though there are two common naming schemes, the *Pople* basis sets (Pople and Nesbet,

[1]This is a small basis set, and was chosen for exactly this reason - to reduce the size of the coefficients table, and the cumbersome formulae following.

Table 1.3: Exponents and contraction coefficients of the 3-21G basis set for carbon. The first three coefficients have been separated to indicate the core contraction of functions.

q	Exponent $\alpha_{\ell q}$	$c_{\ell 1 q}$	$c_{\ell 2 q}$	$c_{\ell 3 q}$
		$\ell = 0$		
1	172.256	0.0617669	0.0	0.0
2	25.9109	0.358794	0.0	0.0
3	5.53335	0.700713	0.0	0.0
4	3.66498	0.0	-0.395897	0.0
5	0.770545	0.0	-1.21584	0.0
6	0.195857	0.0	0.0	1.0
		$\ell = 1$		
1	3.66498	0.23646	0.0	
2	0.770545	0.860619	0.0	
2	0.195857	0.0	1.0	

Table 1.4: 3-21G basis functions for carbon

ℓ	q	Function
0	1	$0.0617669A(0, 172.256)e^{-172.256r^2} + A(0, 25.9109)e^{-25.9109r^2} + 5.53335e^{-5.53335r^2}$
0	2	$0.0617669A(0, 3.66498)e^{-3.66498r^2} + A(0, 0.770545)e^{-0.770545r^2}$
0	3	$A(0, 0.195857)e^{-0.195857r^2}$
1	1	$r\left[A(1, 3.66498)e^{-3.66498r^2} + A(1, 0.770545)e^{-0.770545r^2}\right]$
1	2	$rA(1, 0.195857)e^{-0.195857r^2}$

1954; Ditchfield et al., 1971), and the *correlation consistent* (CC) basis sets (Dunning, 1989). Pople basis functions are described as so:

$$A - BC[DE\ldots][+]\mathrm{G}[*]$$

with [...]s representing optional components. Where A is the number of primitive Gaussian functions in the contractions for the core orbitals, and then $BCD\ldots$ are the numbers of primitive functions in the contractions for the valence orbitals - the first two valence orbitals are included in all of the Pople basis sets, but some include more. Some of these basis functions also include diffuse functions, represented by a '+' before the G, and others can include polarisation functions (including both is also allowed), labelled with a $*$[1]. Appling this nomenclature to the 3-21G basis set described in tables 1.3 and 1.4, we see that the core 1s orbital are made up of three contracted Gaussian functions, and that the 2s and 1p valence orbitals are each described by a pair of orbitals, the first being comprised of two primitive functions, and the second a single function. Obviously approximating an STO with more GTOs will give a better likeness, and this can be seen in fig. 1.4 - though the difference is small, the main advantage of a larger basis set is that there are more orbitals for the valence electrons, which allow a better representation of excitations (the addition of extra, diffuse or polarisation functions in turn allows for better representations of these phenomena). The difference between two Pople basis sets of the same order (i.e. X-YZG) is just that there are different numbers of orbitals in the contractions, there are still the same number of basis functions in total. A comparison of three X-YZG basis sets is shown in fig. 1.4.

The other heavily used basis sets are the *correlation consistent* sets, the idea behind these sets is that each family of basis sets within systematically converge to the all-electron correlation energy at the limit of a complete basis set. The various families of

[1]Some sets even go a stage further with the additional diffuse or polarisation functions, and will indicate this by including two of the relevant symbol in the name.

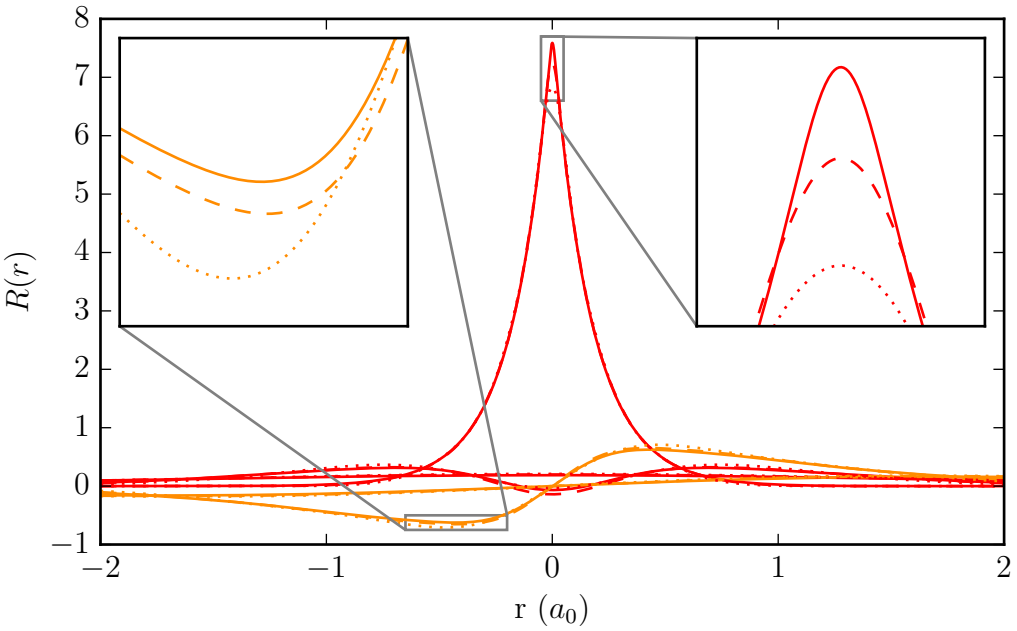

Figure 1.4: Comparison of the 6-31G (—), 4-31G (- - -), and 3-21G (· · · ·) basis sets. The colours show the different ℓ components: ■, S orbitals; ■, P Orbitals

these basis sets follow the systematic names:

$$[\text{aug}] - \text{cc} - \text{p}[[\text{w}]\text{C}]n\text{Z}[-(\text{PP}|\text{DK})]$$

which, ignoring the optional additions for now, can be read as (for $n = \text{T}$) *correlation consistent polarised Valence Triple Zeta*. Again, the [. . .]s denote optional adjustments to the standard basis sets, and terms enclosed in $(X|Y)$ brackets indicate that one of the set be selected. n is one of {D, T, Q, 5, 6, 7} (Double, Triple, etc.), corresponding to the number of *zeta* functions included for the core orbitals. The use of *zeta* as the number of primitives comes from the lesser used convention of labelling primitive functions as ζ, as in eq. (1.4.4). The original family of these basis sets were the cc-pVnZ sets, where the V denotes that the coefficients have been optimised (with respect to obtaining the convergence at the complete basis level) considering only the core-valence correlation. *aug* denotes that additional diffuse functions are added.

Subsequent development of the sets led to the creation of several related sets, and the extra options, w, and C: when considering all of the electrons in the correlation cal-

culations, there are additional correlation terms to consider: the core-core terms - basis sets taking this into account in the optimisation include the label C (Core). Further work then concluded that since the core-core correlation converges more slowly than the core-valence correlation, the two should not be weighted evenly in the optimisation, leading to the additional w (weighted) label (Peterson and Dunning Jr., 2002). Finally, the PP and DK indicate that the basis includes either *Pseudo Potentials* (Peterson, 2003), or that the basis set is a Douglas-Kroll relativistically contracted set (de Jong et al., 2001)[1].

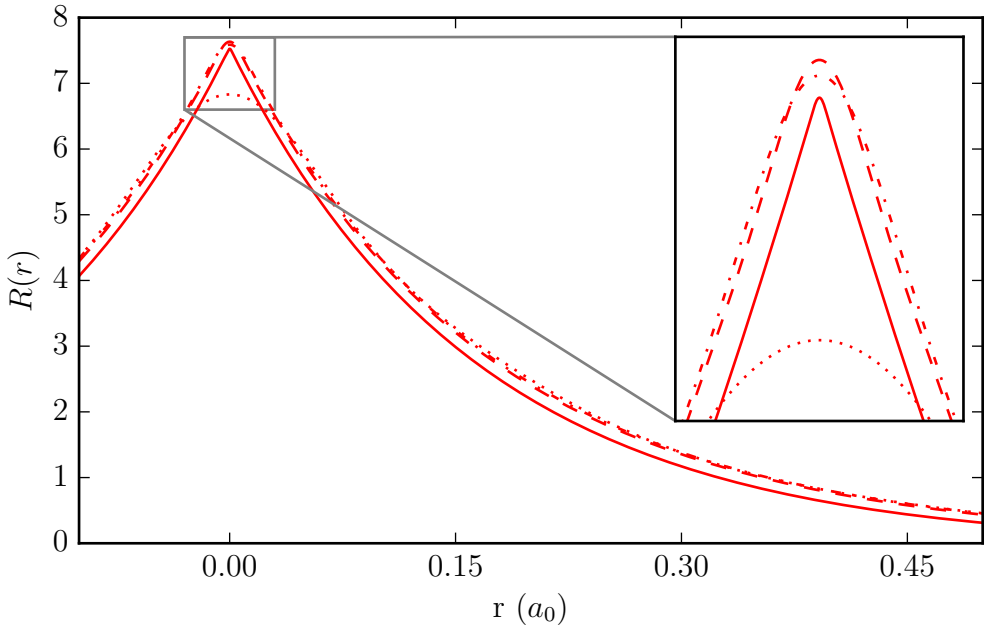

Figure 1.5: Comparison of the cc-pV6Z (—), cc-pVTZ (- - -), 6-31G (– · –), and 3-21G (· · · ·) basis sets' 1s core functions.

The representation of the core orbitals converges very quickly with the number of Gaussian primitives, seen in fig. 1.5, the much larger difference between basis sets as they increase in size is the number of orbitals described for the valence electrons (and then the diffuse and polarised orbitals on top of these). See fig. 1.6 for an idea of the increasing size of basis sets, and table 1.5 for the number of functions per ℓ for the

[1]These basis sets are mentioned, for completeness, but have not been used in this thesis, since none of the calculations carried out have required them.

Pople and correlation consistent basis sets used later.

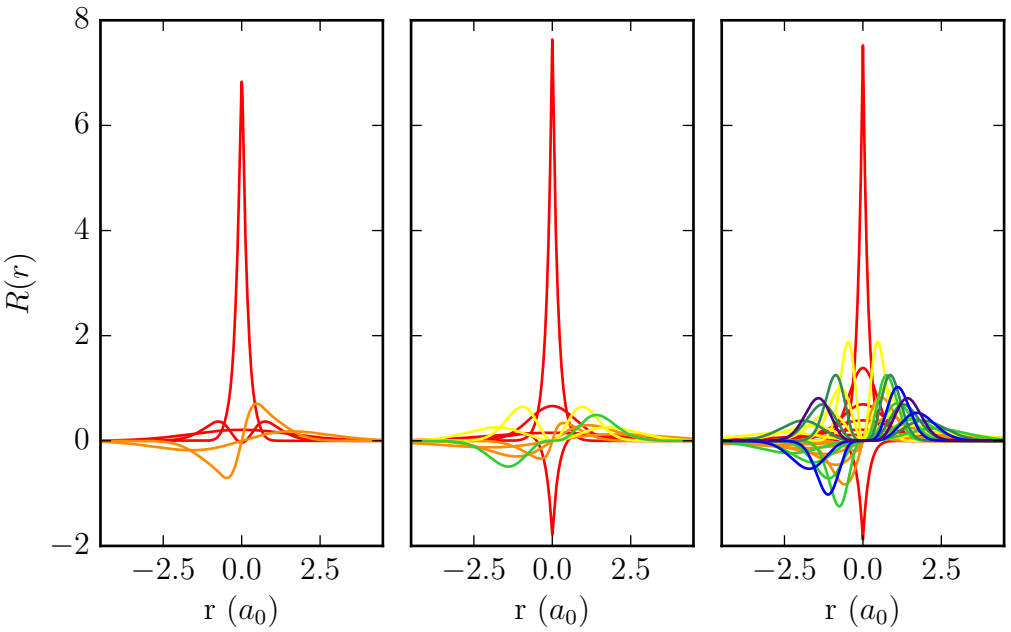

Figure 1.6: Comparison of the 3-21G (left), cc-pVTZ (centre), and cc-pV6Z (right) basis sets. The colours show the different ℓ components: ■, S; ■, P; ■, D; ■, F; ■, G; ■, H; ■, I.

Table 1.5: Overview of the number of functions of each type in the basis sets used in this thesis, for Carbon and Hydrogen. Each cell gives the total number of functions for the corresponding ℓ of its column, followed by the number of primitives making up the contractions (or just 1 if the function is a primitive).

Basis Set	Atom	S	P	D	F	G
Pople basis sets						
3-21G	C	3: 3,2,1	2: 2,1			
	H	2: 2,1				
4-31G	C	4: 4,3,1	2: 3,1			
	H	2: 3,1				
6-31G	C	4: 6,3,1	2: 3,1			
	H	2: 3,1				
6-311G	C	4: 6,3,1,1	2: 3,1,1			
	H	2: 3,1,1				
6-311G**	C	4: 6,3,1,1	2: 3,1,1	1: 1		
	H	2: 3,1,1				
6-311++G** [a]	C	4: 6,3,1,1,1	2: 3,1,1,1	1: 1		
	H	2: 3,1,1,1	1: 1			
Correlation Consistent basis sets						
cc-pVDZ	C	3: 8,8,1	2: 3,1	1: 1		
	H	2: 3,1	1: 1			
cc-pVTZ	C	4: 8,8,1,1	3: 3,1,1	2: 1,1	1: 1	
	H	3: 3,1,1	2: 1,1	1: 1		
cc-pVQZ	C	5: 9,9,1,1,1	4: 3,1,1,1	3: 1,1,1	1: 1,1	1: 1
	H	4: 3,1,1,1	3: 1,1,1	1: 1,1	1: 1	
aug-cc-pVTZ	C	5: 8,8,1,1,1	4: 3,1,1,1	3: 1,1,1	2: 1,1	
	H	4: 3,1,1,1	3: 1,1,1	2: 1,1		

[a] The Pople 6-311+G, 6-311G* and 6-311+G*, nor the 6-31G* basis sets are not defined for H, hence them not appearing here.

2

Methane

Cross sections for electron collisions with methane are important for a number of different applications including combustion (Goodings et al., 1979; Prager et al., 2007) and plasma-enhanced combustion (Wisman et al., 2007), the atmosphere of Titan (Cravens et al., 2010) and chemical vapor deposition (Baek et al., 2013). As a result a number of compilations of recommended values for this cross sections have been performed (Morgan, 1992; Shirai et al., 2002; Kato et al., 2009; Reiter and Janev, 2010; Fuss et al., 2010; Song et al., 2015). Individual experimental studies are discussed later.

Methane has become a standard system for testing theoretical methods (Lengsfield III et al., 1991; Winstead et al., 1993; Bettega et al., 1993; Nestmann et al., 1994). However it is well-established that close-coupling based methods have difficulty converging the polarization potential (Gil et al., 1994; Varambhia et al., 2008). Theoretical treatments have considered elastic scattering (Boesten and Tanaka, 1991; Jain and Baluja, 1992; Machado et al., 2002), as well as electron impact rotational (Jain and Thompson, 1983; Brescansin et al., 1989; Machado et al., 2002), vibrational (Althorpe et al., 1995; Čurík et al., 2008) and electronic excitation (Gil et al., 1994; Bettega et al., 1998; Winstead et al., 1993; Kato et al., 2009). Recently Ziółlkowski et al. 2012 used a close-coupling R-matrix calculation to obtain electronically inelastic collisional excitation cross sections; they then used a high-level electronic structure calculation to determine excited state energies and derivative couplings, and trajectory surface hopping to determine branching in the dissociation of the methane. None of these

theoretical treatments provide a comprehensive solution to the low-energy electron scattering problem. Such a solution would, for example, provide a good representation of the well-known *Ramsauer-Townsend* (RT) minimum, which is very sensitive to the treatment of polarization, and at the same time consider electron impact electronic excitation which, in the case of methane, means representing diffuse electronically excited states which have a significant Rydberg character.

Rydberg states are not usually well represented in close-coupling expansions based upon standard treatments of the target molecule electronic structure. Special procedures have been proposed (Gil et al., 1994; Rozum et al., 2003) for treating Rydberg states in close-coupling studies (see the Rydberg Model section, page 44). More generally the molecular R-matrix with pseudostates method (Gorfinkiel and Tennyson, 2004, 2005) has been demonstrated to give an excellent representation of polarization effects (Halmová et al., 2008; Zhang et al., 2011). In this work we develop a comprehensive, *ab initio* model for the low energy scattering of electrons from methane which considers elastic scattering and rotational excitation at energies spanning the RT minimum, as well as electron impact electronic excitation and hence impact dissociation.

The goal was to create a single model which replicated the specific features of the low-energy electron-methane collision system simultaneously. To do this we concentrated on three main aspects of the problem: the location (and presence) of the RT minimum, the polarizability of the methane target, and the thresholds for the electronic excitations of the target. The following sections gives an overview of the theory used, and then describes attempts to develop a unified model. Results are presented and discussed, with the final section giving conclusions.

Methane in its equilibrium geometry has T_d symmetry. However the polyatomic implementation of the UKRMol codes only treat Abelian groups; which in practice means D_{2h} and its subgroups (Morgan et al., 1997). Here methane was treated using C_{2v} symmetry. D_2 symmetry can also be used and allows only a single H atom to be defined. Tests found that D_2 calculations yield the same results, with no noticable computational advantages. Care was taken in all models to preserve the degeneracies present in a fully symmetrised calculation. Where possible our results are presented

below using T_d symmetry. A C–H bondlength of 1.09395 Å with Hartree-Fock orbitals for the target representation.were used for all calculations.

2.1 Calculations

Many different calculations were performed in the search for a viable model yielding all of the desired properties simultaneously. Below are details on the trials of the various different models described in the Model Classification section, page 38, along with the qualitative and quantitative effects resulting from the variation of the defining parameters of the models.

2.1.1 Target wavefunctions

A scattering model comprises a target representation and a treatment of the "$N + 1$ electron" scattering system. Clearly the target polarizability and electronic excitation thresholds are properties of the target model alone, whereas the treatment of the RT minimum depends on both steps. A number of different target models are examined below, and in choosing between them it is also necessary to consider results obtained using them in scattering calculations.

2.1.2 Complete Active Space Configuration Interaction

All of the methane calculations froze at least the electrons in the $1a_1$ (carbon 1s) orbital. A small CASCI calculation for methane might be given by:

$$[1a_1]^2[2a_1, 1t_2, 2t_2]^8$$

which comprises the ground configuration plus the lowest unoccupied molecular orbital (LUMO). This model gives a target polarizability which is far too small, no RT minimum in the associated scattering calculation, and electronic excitations which are too high. Given that the RT minimum is a feature of low-energy electron scattering caused by a cancellation between the repulsive, static potential and the attractive po-

larizability, it is to be expected that underestimating the polarizability will lead to a poor representation of the minimum.

A more reasonable CAS distributes the eight valence electrons amongst the 8 active or valence orbitals, giving the following model:

$$[1a_1]^2[2a_1, 3a_1, 1t_2, 2t_2]^8$$

In fact, it was found that freezing the lowest 4 electrons had little effect on calculated cross sections, while drastically reducing the computation time, thus the following CASCI model was used as a base for the remainder of the calculations.

$$[1a_1, 2a_1]^4[3a_1, 1t_1, 2t_2]^6$$

In a CAS-CI calculation increasing the number of active orbitals improves all aspects of the calculation. In practice, this approach offers rapidly diminishing returns as using an enlarged CAS gives only a modest improvement to the scattering calculation for a large increase in computational cost (Tennyson, 1996b). Increasing the size of the active space has a larger effect on the excitation energies than the polarizability.

Presence of the Ramsauer-Townsend Minimum

Including extra orbitals in the active space does give an RT minimum eventually, where the number of orbitals required for it to present depends on the basis set. Using a larger basis set with more diffuse functions tended to give the RT minimum sooner - 6-311G* gave an RT minimum for all models examined, as did cc-pVDZ, though surprisingly cc-pVTZ did not[1].

Including the first 4 LUMOs meant that all basis sets tested, with the exception of TZ, produced an RT minimum, although they were all located too low in energy. The smaller basis sets also produced larger total cross sections above about 2 eV (larger by about 1 Å^2 at the peak). The same shifting of thresholds and the peak is seen when including more orbitals.

[1]This can happen when the basis set gives a poor representation of the molecular orbitals, leaving the target electron density overly diffuse - artificially increasing the polarizability.

Excitation Thresholds and Polarizabilities

Excitation energies and polarizabilties as a function of basis set used are shown in table 2.1. In these calculations, the polarizabilities obtained were consistently too low, ranging from 7.5 – 11.5 a_0^3, where the experimental value is 16.52 a_0^3 (Olney et al., 1997).

Table 2.1: First excitation threshold for different basis sets where the CAS is $[1a_1, 2a_1]^4[3a_1, 1t_1, 2t_2]^6$, and polarizabilities are computed using all states up to 25 eV.

Basis Set	First Threshold (eV)	polarizability (a_0^3)
DZP	13.853	9.14
TZ	13.650	8.11
6-31G*	12.335	11.27
6-31G	12.300	11.50
cc-pVDZ	11.626	9.69
cc-pVTZ	11.404	8.30
6-311G*	11.403	7.52
6-311G	11.372	7.75

The method for calculating the polarizabilities here is the *sum over states* (SOS) method, which comes from second-order pertutbation theory (Ditchfield et al., 1971), where the terms of the polarizability tensor are:

$$\alpha_{rs} = 2\sum_{ij} \frac{\langle\psi_i|\,\mu_r\,|\psi_j\rangle\,\langle\psi_j|\,\mu_s\,|\psi_i\rangle}{E_j - E_i} \tag{2.1.1}$$

where r and s represent a pair of Cartesian components, and $\langle\psi_i|$ and E_i are the i^{th} electronic wavefunction and its energy. The sum runs over all dipole allowed transitions - including those into the continuum. In order to converge, this method often requires many states, and the explicit requirement that these states include the con-

tinuum requires that the model used includes an appropriate representation of it. The requirement of the inclusion of many states for convergence is demonstrated both in figs. 2.4 and 2.5 and in Jones and Tennyson (2010).

The polarizabilities can be improved beyond those in the table by including more states in the target region, but the gains are small and the computational cost high. Even if all the states are included, this approach still leads to polarizabilities which converge to less than the true value (Jones and Tennyson, 2010). Up to this point, all test calculations were performed using a standard CAS-CI model. These tested included some very large CAS-CI treatments; up to $[1a_1]^2[2-5a_1, 1-4t_1, 1-4t_2, 1e]^8$, which would have been impractical to use in a full $N+1$ scattering treatment (Halmová et al., 2008).

2.1.3 Rydberg Model

Methane's low-lying excited electron states are diffuse and have a strong Rydberg character. An attempt at modelling this was made by including several additional diffuse functions using standard basis sets on the carbon without changing the CAS. These treatments lowered the excitation energies, but not significantly.

Next we tested the role of the CAS. Our model used a core CAS with the option of exciting a single electron outside this CAS. This model can be described by CSFs of the form:

$$[\text{core}]^n[\text{CAS}]^{(N-n)}$$
$$[\text{core}]^n[\text{CAS}]^{(N-n-1)}[\text{Rydberg}]^1 \,.$$

For example, the main model we tested had CSFs defined by:

$$[1a_1, 2a_1]^4[3a_1, 1t_2, 2t_2]^6$$
$$[1a_1, 2a_1]^4[3a_1, 1t_2, 2t_2]^5[4a_1, 3t_2, 4t_2, 1e]^1$$

We tested two different basis sets to represent Rydberg-like orbitals, which were added to the carbon basis set since the carbon is located at the centre-of-mass. The first basis was a set of quasi-Slater Type Orbitals recreated from Rozum et al. (2003) as a sum of 6 GTOs each. The second set were GTOs taken from Nestmann et al. (1994).These attempts gave large orbital spaces, the largest being $[8a_1, 5t_1, 7t_2, 3e]$; and gave significantly lower ground state energies but proved computationally expensive, where the target calculation alone took upwards of a whole day on a high end workstation; although these calculations were performed prior to the diagonalization routines being improved (Zhang et al., 2011). The results of the two different basis sets were very similar. Increasing the number of orbitals in the extended space decreases the ground state energy monotonically, with larger calculations giving lower results - the calculations are variational, so this is exactly as expected. This model improved upon all aspects of the CAS-CI *target* model - the results of this model were promising. Unfortunately though, to obtain a reasonable polarizability, the number of states required in the inner region was very large - with some tests reaching 999 states[1], such that the outer region calculations would have been infeasible, so this model was not used to produce full electron scattering cross sections.

2.1.4 R-Matrix with Pseudo States

We therefore undertook a series of RMPS calculations. For these calculations, the RMPS orbitals were represented using an even-tempered GTOs with 14 functions for the s, p, and d functions, each with $\alpha_0 = 0.05$ and $\beta = 1.4$, where the meaning of these variables is explained in Madden et al. (2011); Gorfinkiel and Tennyson (2005). The orthogonalisation thresholds used in the N, and $N + 1$ electron regions were 2×10^{-4} and 1×10^{-6}, respectively.

As with the Rydberg Model, the polarizability is dependant on the number of states included, and increases aymptotically with increasing numbers of states. Including all states up to 30eV gave a value within 15% of experiment. The RMPS approach again improved all aspects of the target model over the Rydberg Model, ground energies,

[1]Where 999 was a limitation of the column width of printed variables - this limitation has since been removed.

first excitation thresholds, and polarizabilities are shown in table 2.2.

Table 2.2: Ground energies, first excitation thresholds, and spherical polarizabilities (obtained by summing states up to 30 eV), for various MRCI models. The models are defined by the number of frozen orbitals in the core, and the number of possible excitations out of the active space.

Excitation Orbitals	**Ground Energy** E_h	**Threshold (eV)**	**polarizability** (a_0^3)
MRCI: 2 Frozen, Single excitations; $[1,2a_1]^4[3a_1,1t_2,2t_2]^{6-(0,1)}[\mathrm{RMPS}]^{(0,1)}$			
$[3t_2]$	-40.22466	11.291	10.92
$[4a_1,3t_2]$	-40.22676	10.948	11.45
$[4a_1,3t_2,4t_2]$	-40.25756	10.843	12.30
$[4a_1,3t_2,4t_2,1e]$	-40.27231	10.931	13.78
$[4a_1,5a_1,3t_2,4t_2,1e]$	-40.27474	10.928	13.84
$[4a_1,5a_1,1t_1,3t_2,4t_2,1e]$	-40.27474	10.928	13.84
MRCI: 2 Frozen, Double excitations; $[1a_1,2a_1]^4[3a_1,1t_2,2t_2]^{6-(0,1,2)}[\mathrm{RMPS}]^{(0,1,2)}$			
$[3t_2]$	-40.22466	11.291	10.93
$[4a_1,3t_2]$	-40.22676	10.948	11.47
$[4a_1,3t_2,4t_2]$	-40.25756	10.843	12.44
$[4a_1,3t_2,4t_2,1e]$	-40.27231	10.931	14.12
$[4a_1,5a_1,3t_2,4t_2,1e]$	-40.27474	10.928	14.18
MRCI: 1 Frozen, Triple excitations; $[1a_1]^2[2a_1,3a_1,1t_2,2t_2]^{8-(0,1,2,3)}[\mathrm{RMPS}]^{(0,1,2,3)}$			
$[3t_2]$	-40.22834	11.107	11.38
$[4a_1,3t_2]$	-40.22834	11.107	11.39
$[4a_1,3t_2,4t_2]$	-40.27699	10.566	13.01

The RMPS method gives a good target description but we encountered problems when it was used as part of a scattering calculation: the model predicted an unphysical bound anionic state. First, it was thought this might be a linear dependance problem (Little and Tennyson, 2014), particularly because this was the first time the molecular RMPS method had been used with an atom placed on the centre-of-mass. The integral

codes had to be adapted to cope with this, and the deletion thresholds to deal with linear dependence closely monitored, and adjusted. Increasing the deletion thresholds did not fix the model. Second, we tested the effects of the RMPS orbitals being used. After several other tests the space-filling, even-tempered GTOs were replaced by the virtual orbitals generated by a cc-pVTZ calculation. However this also had little effect: the cross sections obtained after this change were very similar to the standard RMPS ones. Third, a closer inspection of the configurations used in the target model compared to those used in the scattering calculation suggested that the calculation was over correlated as the L^2 terms from eq. (1.3.11) used in the RMPS calculation can contribute as double excitations of the target.

An explanation of this is that the SCF orbitals are stable with respect to single excitations, but not to double excitations, so when the continuum electron shares target orbitals in the L^2 terms from eq. (1.3.11), the energy changed, producing the unbalanced model.

The unbalanced nature of the RMPS model is clearly shown by the behaviour of the low-energy eigenphase sums as the number of orbitals included in the RMPS procedure is increased. As shown in fig. 2.1, the behaviour of the eigenphases changes abruptly with larger models. The eigenphases of the larger models are characteristic of the presence of a bound anionic state; these models also feature an **R**-matrix pole which lies below the energy of the target ground state. A standard CASCI calculation is balanced, by construction. An RMPS calculation may not be. How balanced a calculation must be to give physical results is not a simple problem, and the level of correlation between the N and $N+1$ electron problems is a subtle problem (Rescigno, 1994). A simple first approximation on how balanced the calculation is can be garnered from table 1.1, which demonstrates the sets of configurations used in different models, and their relative levels of correlation.

2.1.5 Multi-Reference Configuration Interaction

To try and balance the RMPS procedure we tested target models which had multiple excitations out of the CAS. Given that the cc-pVTZ basis set alone gave similar results

to the cc-pVTZ + RMPS GTOs sets for single excitation RMPS model, and given the extra complexity of using multiple basis sets and multiple orthogonalisations for the target, just the cc-pVTZ basis set alone was used to produce all orbitals. This approach is unlikely to be general as the central carbon in methane locates GTOs at the centre-of-mass.

The simplest form of this model is described by target CSFs of the form:

$$[1a_1, 2a_1]^4[3a_1, 1t_2, 2t_2]^6$$
$$[1a_1, 2a_1]^4[3a_1, 1t_2, 2t_2]^5[4a_1, 5a_1, 3t_2, 4t_2, 1e]^1$$
$$[1a_1, 2a_1]^4[3a_1, 1t_2, 2t_2]^4[4a_1, 5a_1, 3t_2, 4t_2, 1e]^2$$

Use of this wavefunction solved the issue of the erroneous bound state, as demonstrated by inspection of the low-energy eigenphase sums: compare the results presented in fig. 2.2 with those of the RMPS model given in fig. 2.1. The corresponding elastic cross sections show an even more dramatic change at low-energy, see fig. 2.3. This model employed a model based on a CAS-CI with both single and double excitations into a larger active space. This form of the wavefunction is similar to that produced by quantum chemical *multi-reference configuration interaction* (MRCI) calculations. It was therefore dubbed the MRCI model.

Of course the MRCI model can regarded as step towards doing a complete CASCI run with a CAS of $[1 - 5a_1, 1 - 4t_2, 1e]^{10}$. The next step would be to include triple excitations. However that appeared unneccesary for a balanced calculation (at least for the case of methane); the improvement of double over single excitations is very significantly more than the changes found when including triples over doubles. Furthermore, the computational demands of including triple excitations is too great to be contemplated in a full calculation. The model including only single excitations gives incorrect behaviour at low energy unlike that with doubles, see the total cross sections shown in fig. 2.3.

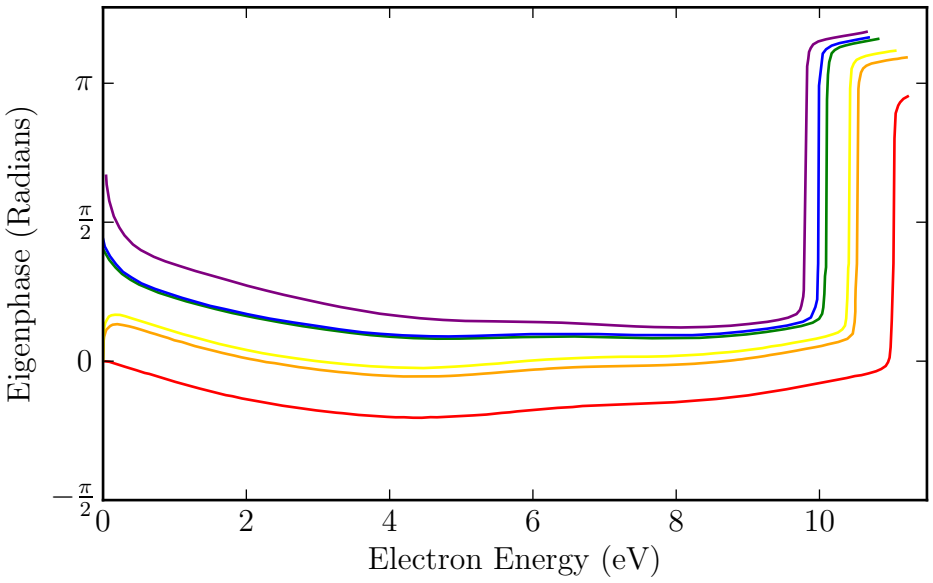

Figure 2.1: C_{2v} A_1 symmetry eigenphase sums for single-excitation RMPS models with increasing numbers of orbitals. All models used a target CASCI of ■ $[1a_1, 2a_1]^4[3a_1, 1t_2, 2t_2]^6$, and are then augmented by single excitations to the following additional virtual orbitals; ■ $[3t_2]$; ■ $[4a_1, 3t_2]$; ■ $[4a_1, 3t_2, 4t_2]$; ■ $[4a_1, 3t_2, 4t_2, 1e]$; ■ $[4a_1, 5a_1, 3t_2, 4t_2, 1e]$.

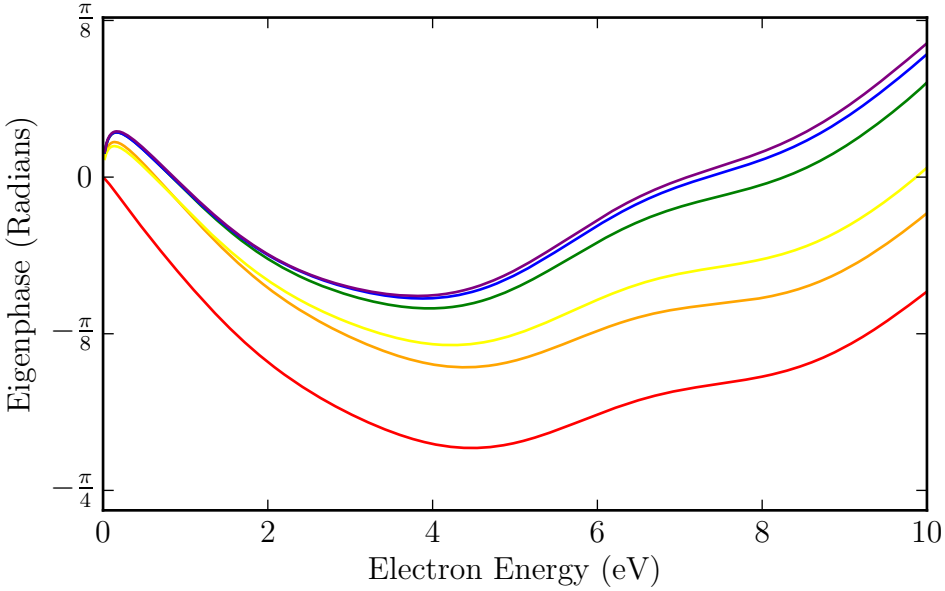

Figure 2.2: C_{2v} A_1 eigenphase sums at low energy for the various models examined. ■ CASCI model $[1a_1, 2a_1]^4[3a_1, 1t_2, 2t_2]^6$, and then the MRCI models, including single and double excitations to the following additional orbitals; ■ $[3t_2]$; ■ $[4a_1, 3t_2]$; ■ $[4a_1, 3t_2, 4t_2]$; ■ $[4a_1, 3t_2, 4t_2, 1e]$; ■ $[4a_1, 5a_1, 3t_2, 4t_2, 1e]$.

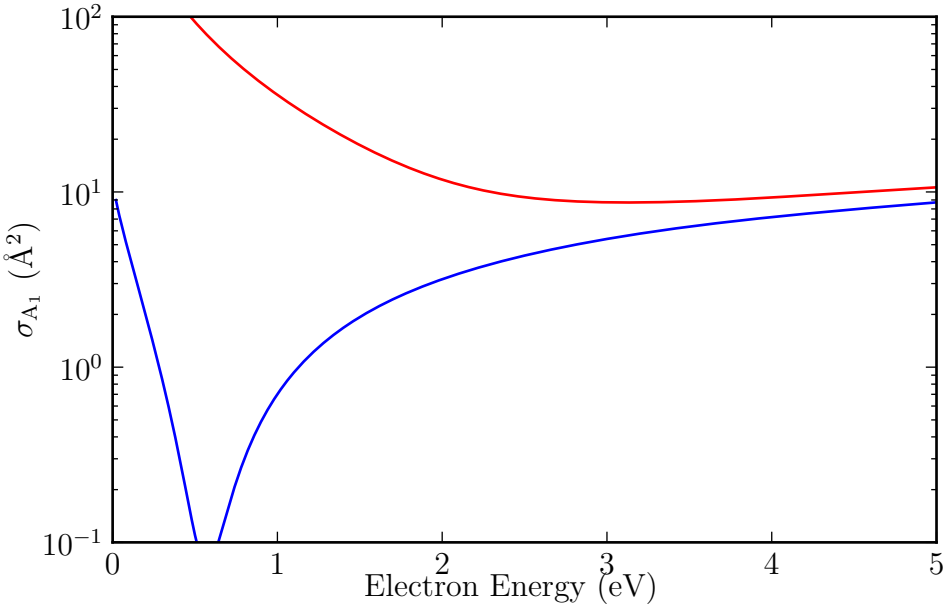

Figure 2.3: C_{2v} A_1 symmetry cross sections for Methane when including CSFs with single and double excitations to the virtual orbitals $[4a_1, 5a_1, 3t_2, 4t_2, 1e]$. ■ Single Excitation; ■ Double Excitation.

Model size

Ideally, every orbital would be included in the calculation. In reality there are several reasons this is not practical since the number of CSFs grows combinatorially with active space size. As the number of CSFs increases, so too do the sizes of the Hamiltonians for each symmetry[1]. The lions share or the computation time in this section is spent diagonalizing the Hamiltonian, which as mentioned previously can either by carried out using dense or sparse algorithms. The dense algorithm has a time complexity of $\mathcal{O}(n^3)$, where n is the dimension of the matrix. If dealing with a sparse matrix, then the approach is iterative, and has time complexity $\mathcal{O}(kn^2)$, where n is as before, and k is the number of requested eigenvalues. The process of taking only k eigenvalues and ignoring the rest is known as the Partition **R**-matrix (Tennyson, 2004).

[1]The relationship here is not linear. An example of one of the several optimisations in the configuration generation and CI calculation is that all CSFs pertaining to a particular target configuration and an occupation of any continuum orbital are represented as a single row in the Hamiltonian. The actual saving in terms of the Hamiltonian rank is a function of the number of continuum orbitals, n_c, the number of electrons, n_e, and the number of orbitals in the active space, n_o: $^{(n_c-1)(n_e+1)}/_{(n_c+n_cn_e-n_e+2n_{orb})}$. This saving is spread over all symmetries and spins however, so the picture on a per symmetry level is more complex.

The problem of overwhelmingly large Hamiltonians has been somewhat decreased by both an improvement in available hardware, and subsequent improvement in the routines to take advantage of new hardward, such as the parallelisation of the `scatci` diagonalization algorithm (Zhang et al., 2011; Roberts, 2012).

Another issue is the problem of linear dependence, deletion of continuum orbitals which strongly overlap target MOs, and the resulting incomplete continuum basis set, as previously discussed.

These limitations and considerations mean that compromises often have to be made in several areas of the calculation. Two areas which were looked at in detail were the total number of states included, and the number of orbitals in the active space for the excitations.

States per symmetry

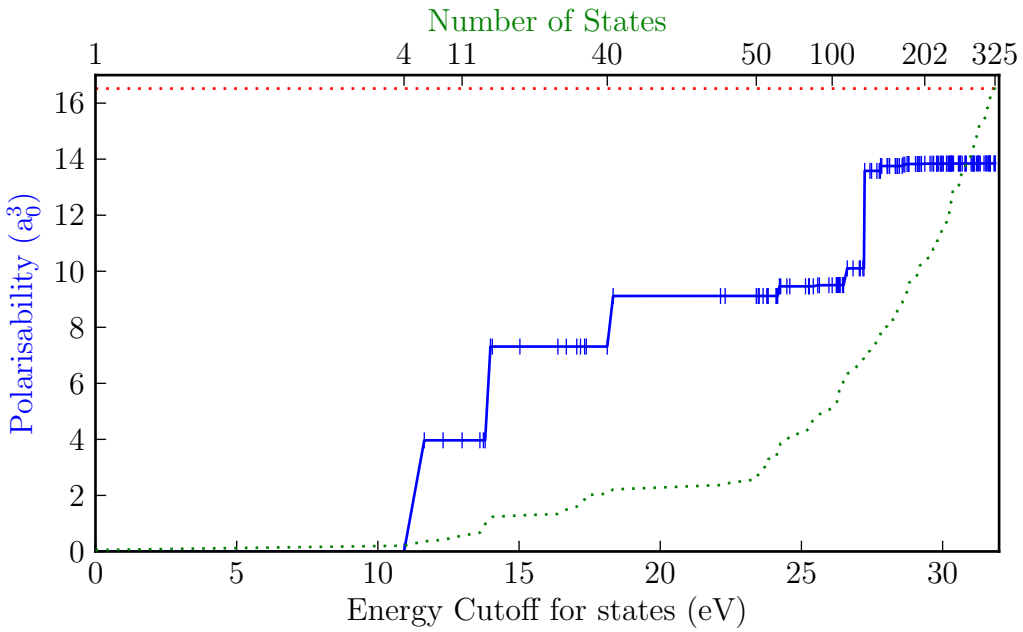

Figure 2.4: The spherical polarizability as a function of states included, where all states are included up to a specific energy cutoff. The numbers at the top show various specific numbers of states, to demonstrate the density of states as a function of energy. — Spherical polarizability, where | marks represent states; ···· experimental polarizability, 16.52 a_0^3, of Olney et al. (1997); ···· number of states included, as a function of energy;

The properties used to gauge the effect of including more states, and more orbitals, were the ground state energy, the excitation energies, and the spherical polarizability, where increasing the number of states increased the polarizability, and increasing the number of orbitals in the active space decreased the ground state energy, and *for the most part* decreased the excitation energies (although, since the excitation energies are differences between states, and some states are effected by including certain orbitals more than others, the excitation energies as functions of included orbitals were not monotonic, like the ground state energy).

If we look at the effect of including more states first, we see that it increases the spherical polarizability. Looking at fig. 2.4, there are a few things to note; firstly, the polarizability is zero when no states are included, this is because, within the SOS method, polarizability in the outer region is given by summing dipole transition moments: since there are no excited states, there are no terms in the sum, giving no polarizability. In reality, an HF wavefunction does have a polarizabilty. Since the HF wavefunction is typically a bad representation of the target, its polarizability is normally too high. The SOS method can also be used as a simple check of the completeness of a close-coupling (CC) expansion, and represents the polarizability of the CC model.

The second is that not all included states contribute; only the states reachable by dipole allowed transitions from the ground state contribute to the polarizability. These are not problematic though, and are to be expected. The problems arise when the additional polarizability added is considered as a function of the number of states included, and the implications these have on the calculation. In general, including additional states contributes a diminishing amount of polarizability, and each state added increases the size of the Hamiltonian to be diagonalized. These states also contribute to the number of channels in the outer region too, but by this point we have the option to exclude states above a certain energy if necessary so it is less of an issue. That the states become more dense at higher energies is not an issue for this particular facet of the calculation, but it is one of the reasons that **R**-matrix calculations above intermediate energies become difficult.

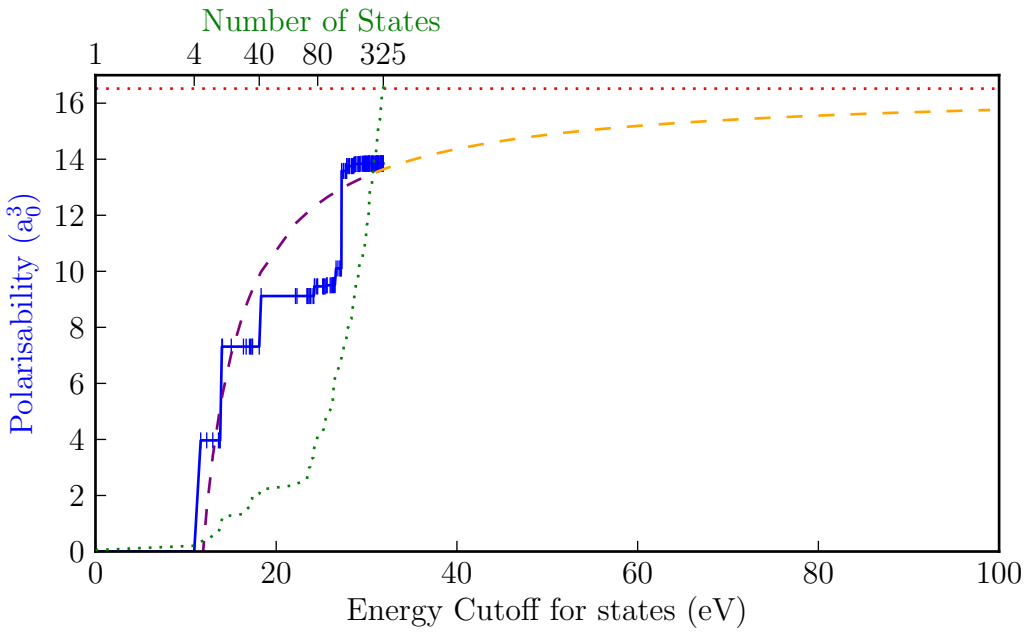

Figure 2.5: The same as fig. 2.4, except with the asymptotic fit extrapolated to higher energy. — Spherical polarizability, where | marks represent states; - - - asymptotic fit for the polarizability; - - - extrapolated asymptotic fit for the polarizability; ···· experimental polarizability, 16.52 a_0^3, of Olney et al. (1997); ···· number of states included, as a function of energy;

Figure 2.5 includes an asymptotic fit to the polarizability as a function of energy, where the fit is $\alpha(\text{states}) = a - {}^{b}/_{x-c}$, with b having been set to the correct polarizability. It is easy to see that reaching the experimental value could be difficult. The density of states also increases as a function of energy, and so including more and more states with the goal of replicating the experimental polarizability is likely to result in infeasibly large calculation. It is also important to note that simply including more states is not a guaranteed method for recovering the polarizability, though it should converge for RMPS type models (Jones and Tennyson, 2010).

Orbitals

Similar behaviour is seen with increasing the number of orbitals in the MRCI active space for the electrons to excite into, and also with freezing fewer orbitals for the ground state. Four models are looked at here;

$$\text{1 frozen, 2 excited} : [1a_1]^2[2, 3a_1, 1 - 2t_2]^{8-\{0,1,2\}}[\text{MRCI Orbs.}]^{\{0,1,2\}} \quad (2.1.2)$$

$$\text{1 frozen, 3 excited} : [1a_1]^2[2, 3a_1, 1 - 2t_2]^{8-\{0,1,2,3\}}[\text{MRCI Orbs.}]^{\{0,1,2,3\}} \quad (2.1.3)$$

$$\text{2 frozen, 2 excited} : [1, 2a_1]^4[3a_1, 1 - 2t_2]^{6-\{0,1,2\}}[\text{MRCI Orbs.}]^{\{0,1,2\}} \quad (2.1.4)$$

$$\text{2 frozen, 3 excited} : [1, 2a_1]^4[3a_1, 1 - 2t_2]^{6-\{0,1,2,3\}}[\text{MRCI Orbs.}]^{\{0,1,2,3\}} \quad (2.1.5)$$

where each of the models is either two, or three, sets of CSFs (for those invloving up to double excitations, and up to triple excitations, respectively). All of these models are subsets of a full CI calculation with a CAS of $[\text{MRCI Orbs.}]^{10}$, where as more orbitals are included, the calculation approaches being completely balanced. As with increasing the number of states, the issue here is again a hardware enforced limit, with more orbitals resulting in more configurations, which, as before, increases the size of the Hamiltonian.

The main effects of changing the number of included orbitals are to lower the ground state energy, and the excitation thresholds. It also changes the polarizability, but it's effect here is more to change the polarizability which the calculation seems to converge to, shown in fig. 2.6. For each of the four models described by eqs. (2.1.2) to (2.1.5), the MRCI Orbitals inclded were $[1-3a_1, 1t_2, 2t_2]$ multi reference active space with excitations to the following additional virtual orbitals (in order): $[3t_2]$; $[4a_1, 3t_2]$; $[4a_1, 3t_2, 4t_2]$; $[4a_1, 3t_2, 4t_2, 1e]$; and $[4a_1, 5a_1, 3t_2, 4t_2, 1e]$, except for eq. (2.1.3), which does not have a result for the $[4a_1, 5a_1, 3t_2, 4t_2, 1e]$ active space, as it took too long to run.

The three plots here, figs. 2.6 to 2.8, have the number of target CSFs on logarithmic scales, where this is related to the cpu time to diagonalize as mentioned previously, $\mathcal{O}(n^3)$, or $\mathcal{O}(kn^2)$, depending on the diagonalization scheme. The aim here is to avoid venturing over to the right hand sides of these plots, while either maximising, or minimising the quantities we want, simultaneously for all three properties.

It's also worth noting that all of these plots include all states up to 30 eV, which has an additional implication not shown here: when more orbitals are included, there

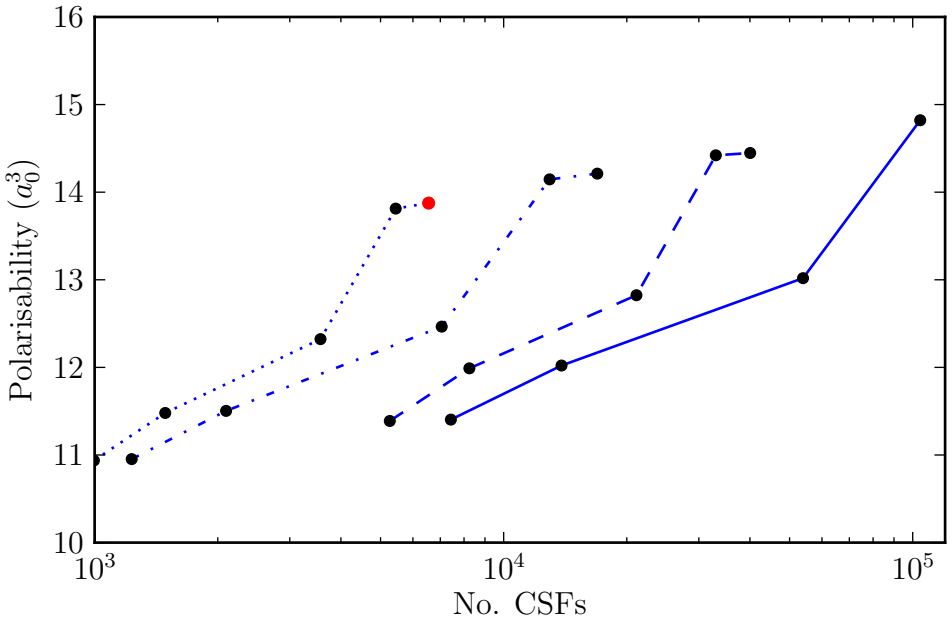

Figure 2.6: Spherical polarizability for increasing numbers of included orbitals for four MRCI models. This figure has the same convention of line style as figs. 2.7 and 2.8; — lines represent the largest models, with just a single frozen orbital, and up to three electrons excited out of the core active space. - - - lines have a single frozen orbital, and up to two excited electrons, – · – lines have two frozen orbitals, and up to three electrons excited, and the ···· lines have two frozen orbitals, and up to two excited electrons. Each line has up to five ● associated with it; the five active spaces, ordered by size, all augmenting the $[1-3a_1, 1t_2, 2t_2]$ multi reference active space with excitations to the following additional virtual orbitals (in order): $[3t_2]$; $[4a_1, 3t_2]$; $[4a_1, 3t_2, 4t_2]$; $[4a_1, 3t_2, 4t_2, 1e]$; $[4a_1, 5a_1, 3t_2, 4t_2, 1e]$. The largest model omits the last MRCI active space, as it was not a feasible calculation to run solely for the sake of this demonstration. The ● point represents the model that was selected.

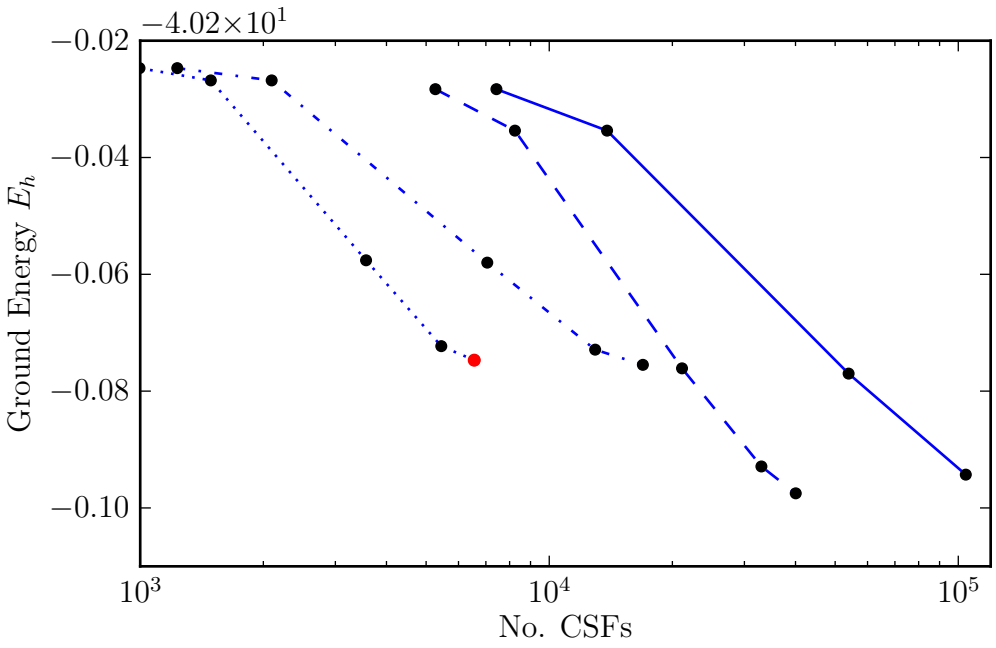

Figure 2.7: Ground state energies for increasing numbers of included orbitals for four MRCI models. This figure has the same convention of line style as figs. 2.6 and 2.8; — lines represent the largest models, with just a single frozen orbital, and up to three electrons excited out of the core active space. - - - lines have a single frozen orbital, and up to two excited electrons, – · – lines have two frozen orbitals, and up to three electrons excited, and the ···· lines have two frozen orbitals, and up to two excited electrons. Each line has up to five ● associated with it, the five active spaces, ordered by size, all augmenting the $[1-3a_1, 1t_2, 2t_2]$ multi reference active space with excitations to the following additional virtual orbitals (in order): $[3t_2]$; $[4a_1, 3t_2]$; $[4a_1, 3t_2, 4t_2]$; $[4a_1, 3t_2, 4t_2, 1e]$; $[4a_1, 5a_1, 3t_2, 4t_2, 1e]$. Again, the largest MRCI active space was omitted due to time / cpu restraints. The ● point represents the model that was selected.

are more possible configurations, the density of states is generally higher, that is, there are more states up to a given energy. These additional states have two primary effects, the first is that the Hamiltonian matrix, which is normally overwhelmingly sparse, becomes less sparse, where increasing the number of included states up to around 1000 made the Hamiltonian around 90% sparse, from an initial sparseness of around 99.9%. Originally, `scatci` simply used a dense matrix multiplier; profiling of `scatci` revealed that the matrix multiplication step was a major contributor to the total runtime (Zhang et al., 2011; Roberts, 2012), and so additional schemes were introduced, one of these was a sparse matrix multiplier. When a matrix contains many zeros, it can be more efficient to store it as a series of elements paired with their indices; i, j; this is the sparse matrix format. Depending on the precision of the matrix, the sparseness at which this becomes favourable changes ($^2/_3$ for single precision, $^1/_2$ for double precision, and $^1/_3$ for quad precision) - for example, a 90% sparse matrix of double precision, with dimension $100,000$ would take up $100000^2 \times 8\text{B} = 80\text{GB}$ if stored dense, but only $100000^2 \times 10\% \times (4+4+8)\text{B} = 16\text{GB}$ if stored as a sparse matrix (where 32 bit integers are used. `integers` use a single `word` or memory, and `doubles` use 2)[1].

At the time, the matrices being examined were very large, and very sparse; using a dense matrix multiplier on very large, very sparse matrices is both inefficient, and adds restrictions to which computers can be used (as the matrices are loaded into memory, adding large RAM requirements to the machine running the calculation). With this also comes a performance increase, as the multiplication algorithms are not wasting time reading many zeros from memory. Both the performance gain, and the memory savings are larger for more sparse matrices, with the larger matrices examined here being seemingly at the cross over point between the sparse and dense algorithms. For *small* matrices, the dense multiplier was always considerably faster.

Which method proved faster varied from machine to machine, with the dense schemes often proving faster. Unfortunately, due to a bug in the `dsyevd` routine of `LAPACK`, the dense algorimth cannot be used for dimensions $>\sim 100000$, and the sparse algorithms had to be used instead.

[1] In reality the storage size is not quite this simple, as more efficient data structures can be used, but this makes a good approximation

The next target for parallelisation of `scatci` will likely be the construction of the Hamiltonian, which should scale embarrassingly / pleasingly with cores, yet is still done serially.

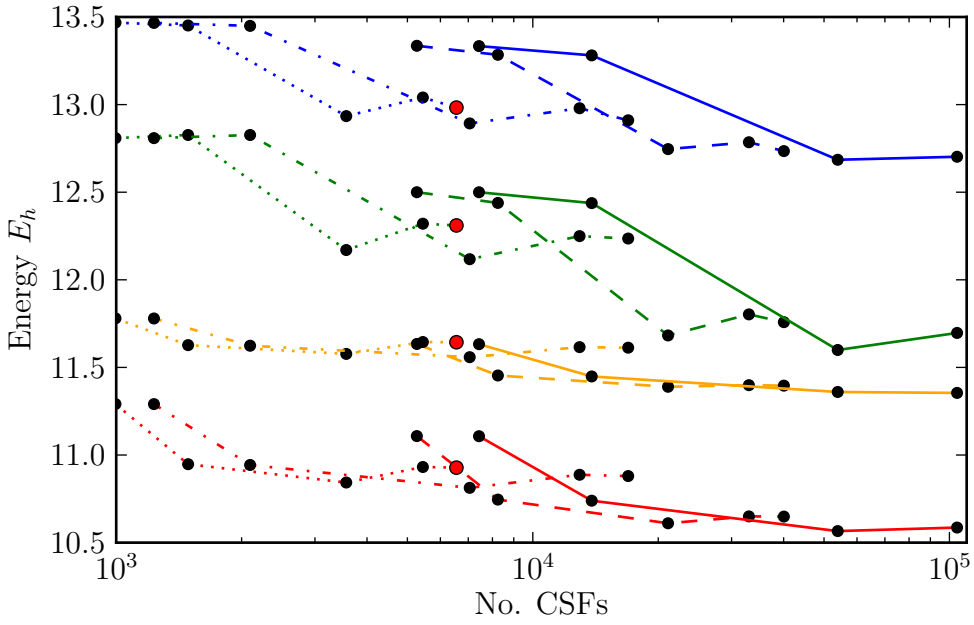

Figure 2.8: Excitation energies for increasing numbers of included orbitals for four MRCI models. This figure has the same convention of line style as figs. 2.6 and 2.7; — lines represent the largest models, with just a single frozen orbital, and up to three electrons excited out of the core active space. - - - lines have a single frozen orbital, and up to two excited electrons, – · – lines have two frozen orbitals, and up to three electrons excited, and the ···· lines have two frozen orbitals, and up to two excited electrons. There are four distinct groups of lines, the ■ lines are the X $\rightarrow 1^3T_2$ excitation; ■ X $\rightarrow 1^1T_2$; ■ X $\rightarrow 1^3A_1$; and ■ X $\rightarrow 2^3T_2$. The ● points simply point out where each model lies on the plot, where each line represents a specific excitation for a specific number of frozen orbitals and maximum number of excited electrons, along each line the number of virtual orbitals augmenting the active space, $[1-3a_1, 1t_2, 2t_2]$, increases as $[3t_2]$; $[4a_1, 3t_2]$; $[4a_1, 3t_2, 4t_2]$; $[4a_1, 3t_2, 4t_2, 1e]$; $[4a_1, 5a_1, 3t_2, 4t_2, 1e]$. As with figs. 2.6 and 2.7, the models with only a single frozen orbital, and up to three excited electrons do not have entries for the $[\ldots][4a_1, 5a_1, 3t_2, 4t_2, 1e]$ CAS. The ● points are the model which was used for the main calculations.

In the case of the models being examined here, for the larger models, the Hamiltonians became less sparse. Including more states reduced the overall sparseness of the Hamiltonian considerably, with the Hamiltonian of the final model selected being 87.34% sparse.

It is also important to note that the dense operations give all of the eigenvalues and vectors, by default; the sparse algorithms however are iterative, and provide the eigenvalues and corresponding vectors in descending order; where, as with many aspects of these calculations, each subsequent eigenvalue/vector pair contributes less to the total cross section. The number of **R**-matrix poles that need to be included to for convergence is approximately the number of target times continuum configurations. Other configuraions giving the higher poles correspond the slowly converging electron-electron correlation problem - these configurations are confined to the inner region, and so the fact that their contribution to the outer region is neglibigible is not surprising (Tennyson, 2004). In these calculations, around 20% (total $\sim 100,000$) of the **R**-matrix poles were used.

2.2 Results

A number of target basis sets and R-matrix radii were tested, however the calculations were not particularly sensitive to these. The final model used a cc-pVTZ GTO basis set, an R-Matrix sphere radius of 13 a_0. and the MRCI model with the core, active and virtual spaces defined by $[1a_1, 2a_1]^4$, $[3a_1, 1t_2, 2t_2]$ and $[4a_1, 5a_1, 3t_2, 4t_2, 1e]^1$, respectively. In the outer region R-matrices were propagated to 100.1 a_0, plus or minus $10 - 20$ a_0 for convergence tests. All subsequent results are from this model only, with 223 states included in the outer region (all states found up to 30 eV). Unless otherwise stated, the results are summed over the four symmetries given in a C_{2v} calculation: $^2A_1$, $^2B_1$, $^2B_2$ and $^2A_2$.

When comparing the results obtained in this thesis to others, it should be taken into account that all results presented as *present work* are the results of a single consistent model, which gives solutions to many aspects simultaneously. On the other hand, when gathering theoretical results for comparison, they are not subject to this constraint and so have more flexibility in the selection of model parameters - the behaviour of aspects not being measured are not required to behave correctly. While this is also the case with any properties of the system that have not been observed in this work, cross

sections for many processes are all calculated simultaneously and consistently[1] and compared to experiment, putting more constraints on the model. There are obviously benefits to having a single model which is able to replicate a broad range of results, first is consistency. Second, is the ability to extrapolate where you have some cross sections for one reaction type, but not necessarily another - in the situation where you have multiple models for different problems you cannot do this.

2.2.1 Eigenphases

Eigenphases are a useful diagnostic tool for comparing various models and theories. Sohn et al. (1986) provide some empircal eigenphases extracted from their measured *differential cross sections* (DCS) using phaseshift analysis due to Nesbet (1979). Their analysis assumed that only partial waves up to d are important which is a dubious assumption as they considered energies as high as 5 eV. Ferch et al. (1985) performed a modified effective range analysis of low-energy cross section measurements to give low-energy eigenphases. Very recently Fedus and Karwasz (2014) also performed an effective range analysis yielding a set of low-energy s, p and d eigenphases.

Figure 2.9 compares our results with those of Ferch et al. (1985), Sohn et al. (1986) and Fedus and Karwasz (2014) for energies below 1 eV. Our "A_1" calculations are actually for A_1 in C_{2v} symmetry so contain contributions from other symmetries in T_d. Considering only $\ell \leq 2$, these eigenphases correspond to s+p+2d. It can be seen that even at 0.1 eV, partial waves with $\ell > 0$ make a significant contribution. A comparison of our eigenphases with the "A_1" eigenphases of Fedus and Karwasz (2014) gives good agreement at higher energies, at low energy the peak in our eigenphase sum appears to slightly too low. This is consistant with the fact that this model still does not recover the full polarizability, as discussed further below.

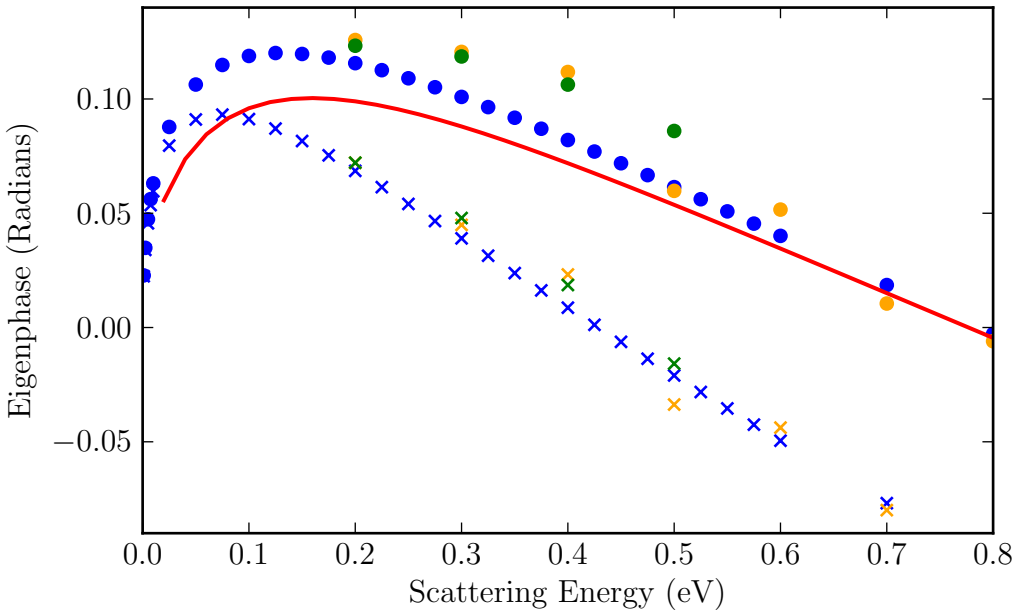

Figure 2.9: Low-energy $^2A_1$ eigenphases: — summed C_{2v} R-matrix A_1 eigenphases. For the empirical determinations × represents s wave only and ● summed s+p+2d; empirical data from ×,● Ferch et al. (1985); ×,● Sohn et al. (1986); ×,● Fedus and Karwasz (2014).

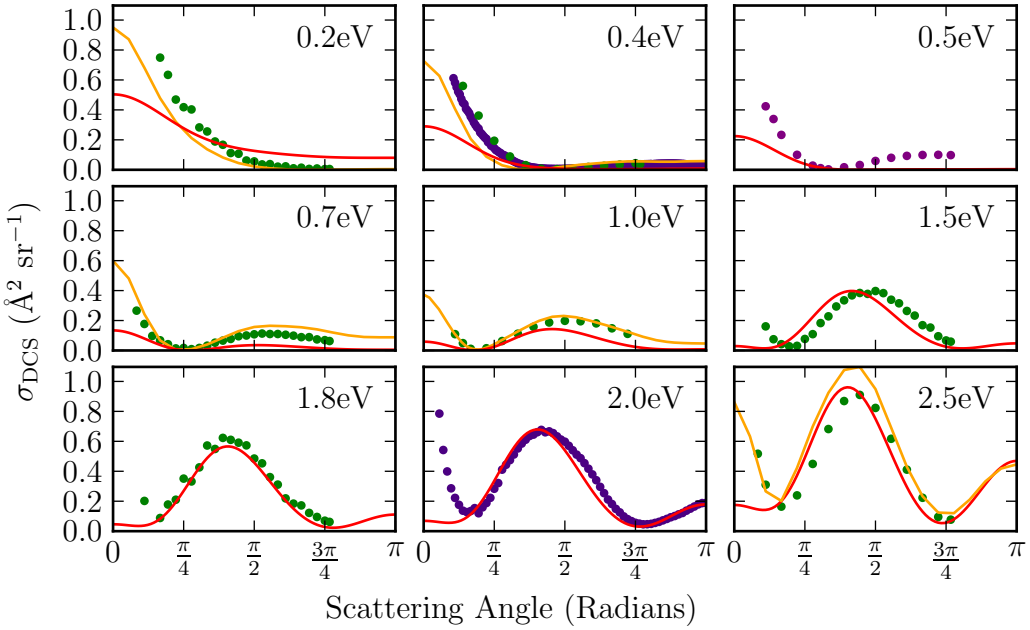

Figure 2.10: DCSs for energies between 0.2 and 2.5 eV. — Present work. — Machado et al. (2002); ● Müller et al. (1985); ● Sohn et al. (1986).

2.2.2 Differential Cross Sections

As seen in fig. 2.10, the DCSs do not agree well with experiment below 1 eV for a scattering angle below 30°. Above 1 eV, but below 5 eV, the agreement is good, but only above 30°. Above 5 eV, see fig. 2.11, the agreement with experiment is excellent, and all the theories agree with just small differences in the forward scattering.

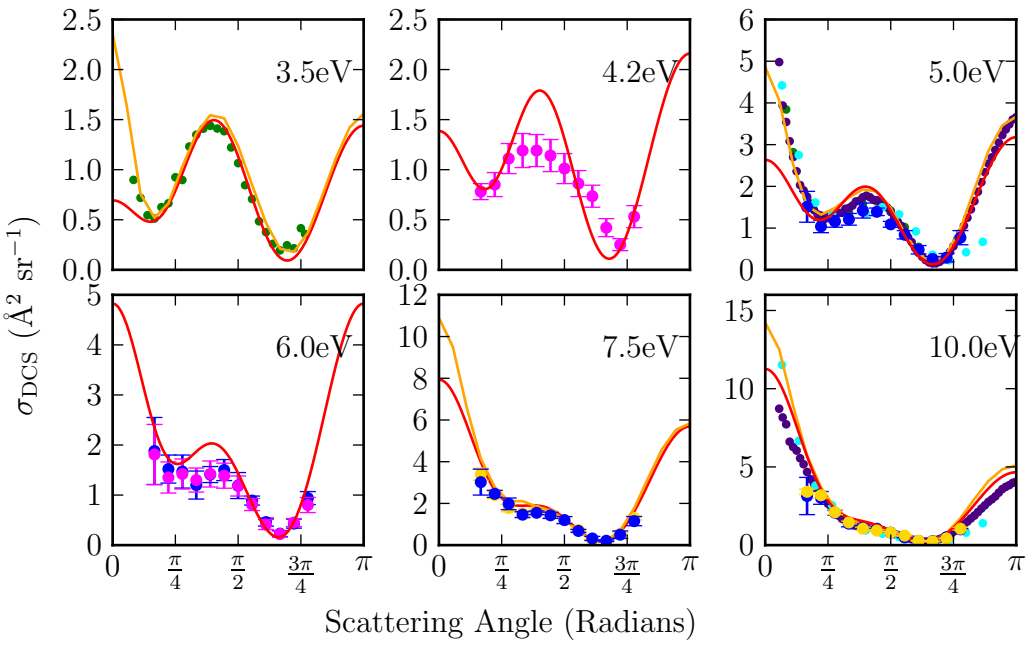

Figure 2.11: DCSs for energies between 3.5 and 10.0 eV. — Present work. — Machado et al. (2002); ● Sohn et al. (1986); ● Mapstone and Newell (1992); ● Müller et al. (1985); ● Shyn and Cravens (1990); ● Curry et al. (1985); ● Tanaka et al. (1982).

The behaviour for small angles at low energy, is almost certainly due to the still incomplete representation of polarization effects. Previous calculations have shown that it is indeed at low angles and low energies that are particularly sensitive to the inclusion of polarization effects (Fujimoto et al., 2014). The treatment of polarization could perhaps be improved by including more states in the calculation, or by freezing fewer electrons. The approaches are not exclusive, but both increase the computational cost. It was initially believed that including all of the channels in the outer region would

[1] this method calculates elastic, electronic and rotational excitation, differential, momentum transfer cross sections, and aligned cross sections.

help resolve this issue, but the differences proved to be minimal, and without the aid of PFARM, this would have come at an enormous computational cost.

Another potential explanation of the low energy, small angle, discrepancy is a lack of inclusion of the polarization effects of higher partial waves, rather than the underestimation of the polarizability. This was an issue raised by one of the referees of Brigg et al. (2014), with the suggestion of adding a $c_1 - c_2 \sin(\theta/2)$ contribution to the differential cross sections to obtain a better agreement, where the additional contirubtion comes from the description of low angle description of cross sections in O'Malley et al. (1962); O'Malley (1963); O'Malley and Crompton (1980); Buckman and Mitroy (1989). The result comes from the expansion of the differential cross section in powers of $k^2 \ln(ka_0)$;

$$\sigma(\theta) = A^2 + \pi/a_0 \; \alpha A k \sin(\theta/2) + 8/3a_0 \; \alpha A^2 k^2 \ln(ka_0) + O(k^2)$$

where A is the scattering length, a_0 the Bohr radius, α is the polarizability, and $k^2 = 2mE/\hbar^2$.

The validity of this depends on previous expressions in the papers, which are aimed at modeling electron-atom collisions, specifically for inert gasses, though that may not be an issue in the case of methane, due to it's high symmetry, and the fact that it is isoelectronic with Neon. Given the strength of the methane polarizability, this term (in the $\ell = 0$ phase shift) requires a collision energy less than 0.8 eV, making it only relevant for the very lowest energies in fig. 2.10.

As for the lack of contributions from higher partial waves, this is valid, and the **R**-matrix codes are currently being reengineered to be able to efficiently handle high ℓ partial waves. The state of the convergence of the integral cross sections is not a concern, they appear to be correct and converged, since the $\sin(\theta)$ contribution nullifies much of the issue here.

It should also be noted that there is some evidence that a flattening of low energy, small angle elastic cross sections may be a feature of close coupling calculations with inexact target states using pseudostates or other additional functions to model the long range polarization(Plummer et al., 2004; Zatsarinny et al., 2006).

The results of Machado et al. (2002) do not fall foul of this, as they use a model short range correlation potential at short range, and then swap to a long range potential at larger r.

2.2.3 Rotational Excitation

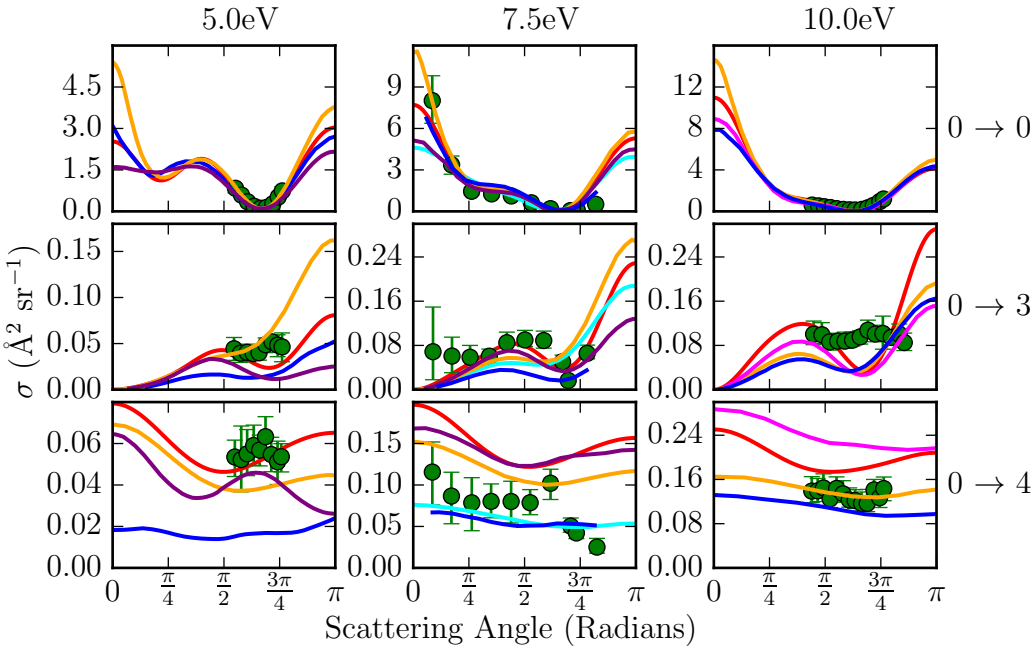

Figure 2.12: Comparison of rotationally resolved differential cross sections with experiment. The columns are comparisons at 5, 7.5, and 10eV, respectively. The rows distinguish between different transitions. — Present work; — Machado et al. (2002); — Brescansin et al. (1989); — Jain and Thompson (1983); — Varella et al. (2001); ● Müller et al. (1985).

Rotationally resolved differential cross sections are also calculated, and agree well with experimental results of Müller et al. (1985), as shown in fig. 2.12. The elastic 0 → 0 cross section is much larger than the excitation cross sections and the calculations show differences at low angles similar to those observed for the rotationally unresolved elastic DCS. The small excitation cross sections all have a relatively large experimental uncertainty and our calculations agree reasonably well with these measurements.

Figure 2.13 shows that our calculated rotational excitation cross sections are in good agreement with the measured ones due to Abusalbi et al. (1983) and Brescansin

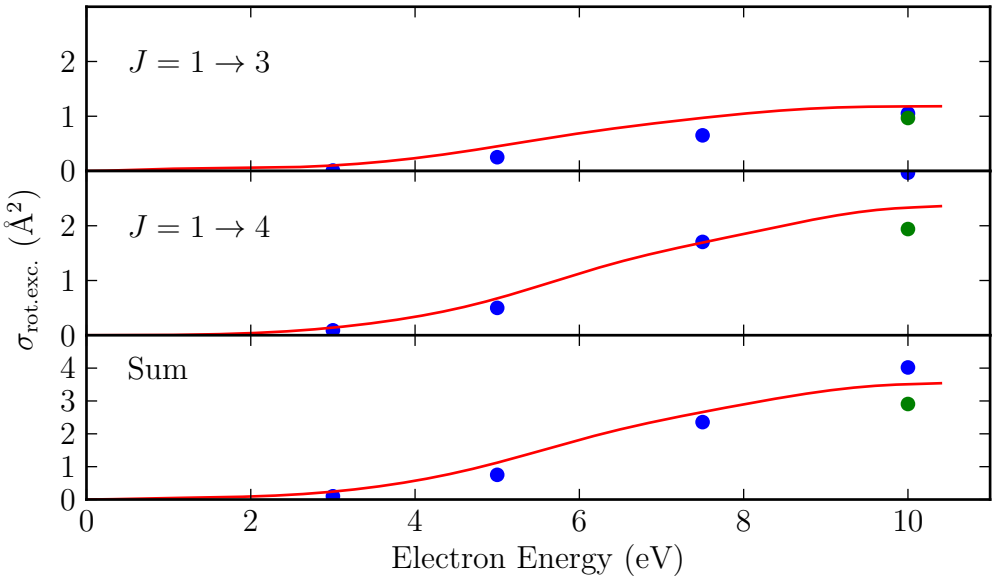

Figure 2.13: Rotational Excitations for $J = 0 \to 3, 4$ and their sum. — Present Work; ● Brescansin et al. (1989) ● Abusalbi et al. (1983).

et al. (1989).

2.2.4 Elastic cross section

As seen in fig. 2.14, the calculated elastic cross section agrees well with the various experiments, the RT minimum is present at the correct energy – albeit with a slightly lower minimum, which could be due to either to experimental cross sections being blurred by the energy resolution or our neglect of nuclear motion. Otherwise we obtain good agreement with the measured cross sections and in particular they agree with the recommendations of Song et al. (2015), which were compiled from consideration of multiple experiment results, at all energies.

Figure 2.15 compares the elastic cross section with various other theoretical results: the other R-Matrix calculations of Antony et al. (2004), Ziółlkowski et al. (2012), Vinodkumar et al. (2001), and Nestmann et al. (1994), as well as the Schwinger variational iterative method calculations by Machado et al. (2002). The recommended values of Song et al. (2015) are also given. We note that our cross section is smooth and monotonic in the energy range 1 to 10 eV, while the previous R-Matrix calculations gave

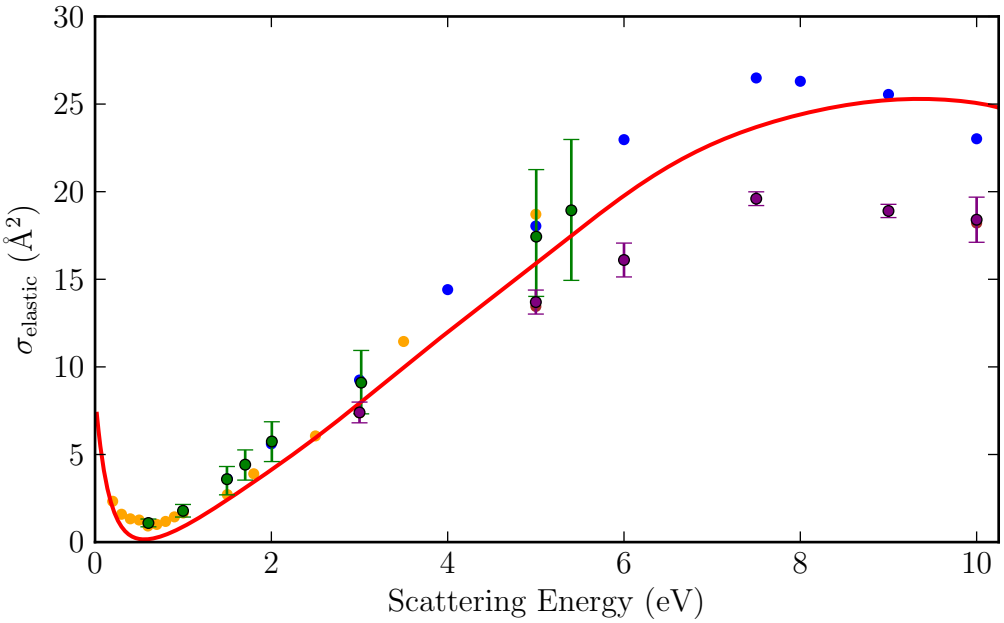

Figure 2.14: Elastic cross section compared with experimental results. — Present work; ● Sohn et al. (1986); ● Bundschu et al. (1997); ● Boesten and Tanaka (1991); ● Tanaka et al. (1982); ● Song et al. (2015). The results of Cho et al. (2008) can be seen at 5 and 10 eV, underneath the Tanaka et al. (1982) points.

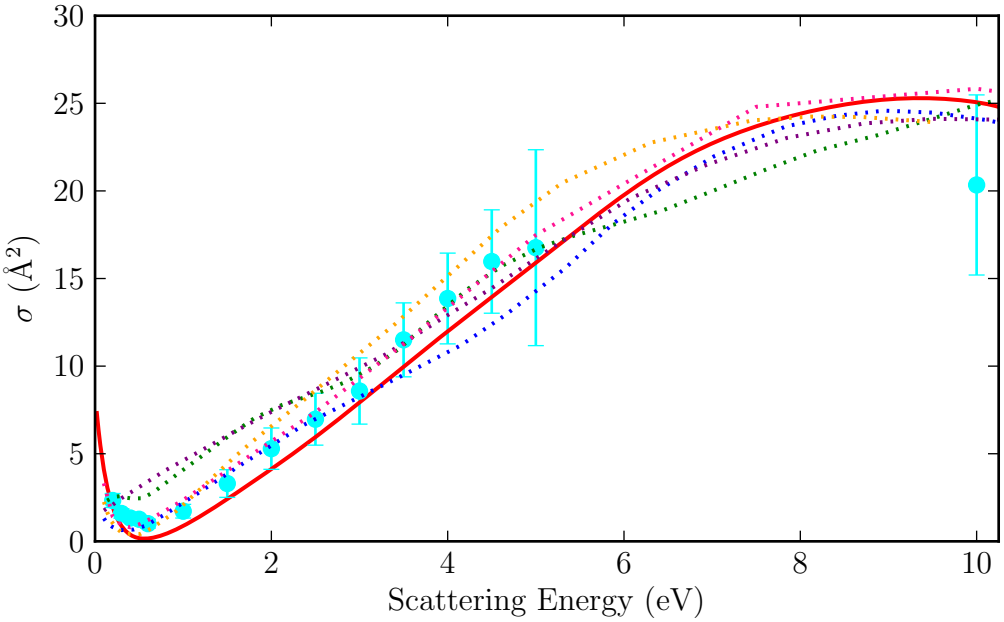

Figure 2.15: Elastic cross section compared with various other theories and the recommended results of Song et al. (2015). — Present work; · · · · Antony et al. (2004); · · · · Machado et al. (2002); · · · · Ziółkowski et al. (2012); · · · · Vinodkumar et al. (2001); · · · · Nestmann et al. (1994); ● Song et al. (2015).

undulant curves. Such undulations are not physical and almost certainly are the result of an incomplete representation of the continuum due to overly aggressive orthogonalisation. This illustrated in fig. 2.16 which shows the effect of changing the deletion threshold. The results with the higher threshold show the undulations characteristic of an incomplete basis.

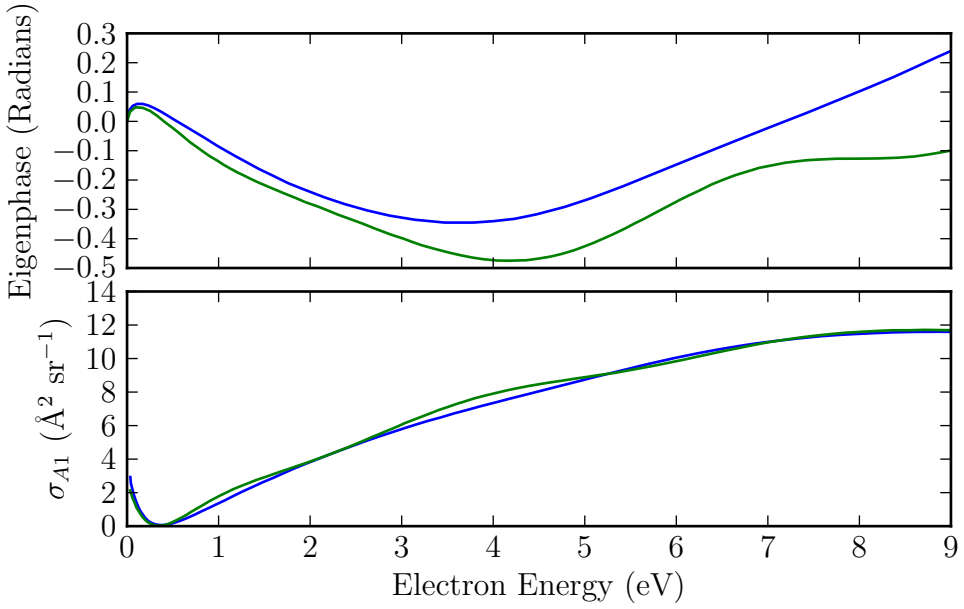

Figure 2.16: A_1 Eigenphase and Cross section for two different inner region orbital orthogonalisation deletion thresholds: — 2×10^{-9} and — 2×10^{-8}.

2.2.5 Momentum Transfer cross section

Figure 2.17 compares our momentum transfer cross section with the experimental results of Tanaka et al. (1982), and the theretical results of Machado et al. (2002). Both the present work, and Machado et al. (2002) show reasonable agreement with the experimental values recommended by Song et al. (2015), although in both cases the peak is shifted to higher energy.

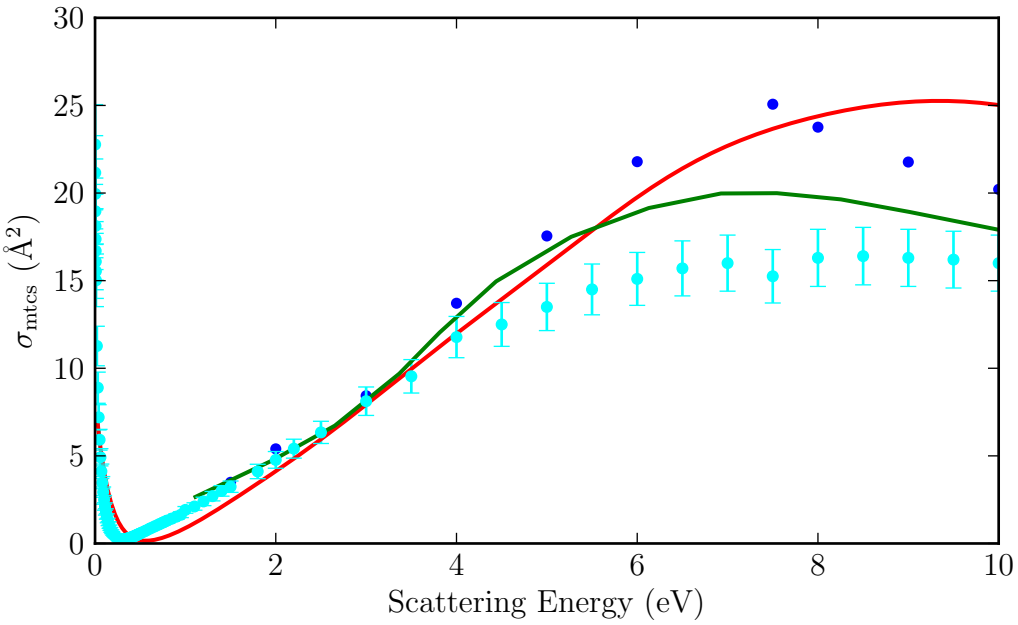

Figure 2.17: Momentum transfer cross section: — Present work; — theory by Machado et al. (2002); ● experiment by Tanaka et al. (1982); ● recommended by Song et al. (2015).

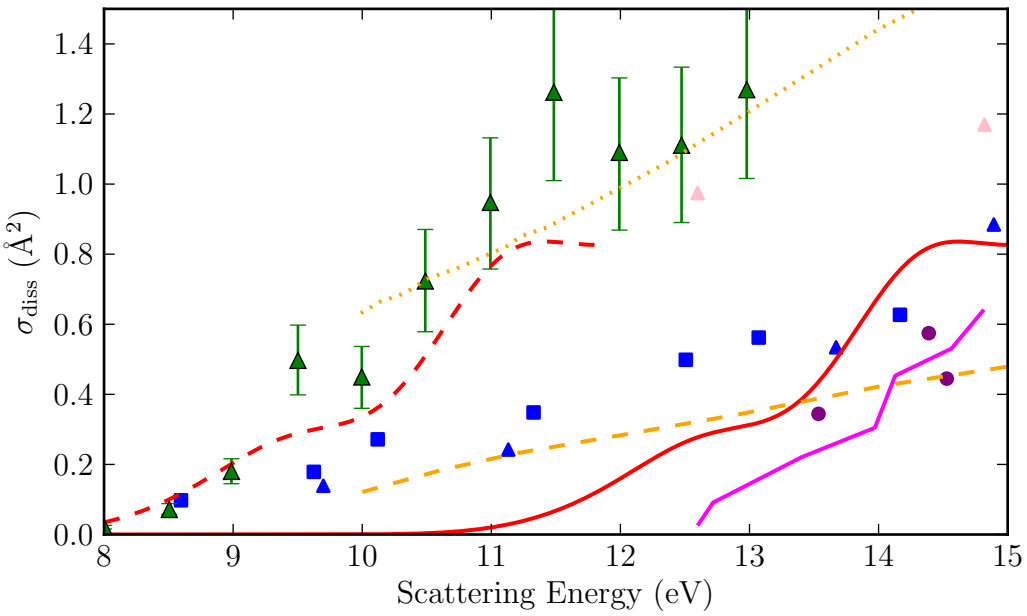

Figure 2.18: Electron impact dissociation cross section, Theory: — present work; - - - present work, shifted to lower energy by 3.2 eV; — Hayashi (1990); - - - CH_2 of Ziółlkowski et al. (2012); ···· CH_3 of Ziółlkowski et al. (2012). Experiment: ■ CH_2 of Nakano et al. (1991); ▲ CH_3 of Nakano et al. (1991); ▲ CH_3 of Makochekanwa et al. (2006); ▲ CH_3 of Motlagh and Moore (1998); ● Winters (1975).

2.2.6 Electron Impact Dissociation

All electronic excitations in methane lie above the dissociation limit and the low-lying excited states are all known to dissociative. Therefore the dissociation cross section calculated here is simply a sum of all of the excitation cross sections, as they are all assumed to be dissociative.

Figure 2.18 compares results for electron impact dissociation and that both experimental and theortical conflict. As seen earlier in fig. 2.15, the total cross section results differ only a small amount from one another; however the dissociation cross sections are much less consistent.

There are two issues with the near-threshold behaviour of the calculated electron impact dissociation cross sections. The first is that our theoretical model overestimates the vertical excitation energy for the lowest excited state. The second is that inclusion of nuclear motion effects is likely to significantly lower this threshold, see Stibbe and Tennyson (1998). Ziółlkowski et al. (2012) addressed these issues by shifting their cross sections to lower energy by 3.5 eV. As our vertical excitation energy is 0.3eV lower than theirs, fig. 2.18 also gives our cross sections shifted to lower energy by 3.2 eV. Our shifted results give excellent agreement with the near-threshold measurements of Nakano et al. (1991) and Makochekanwa et al. (2006); this must however be regarded as somewhat fortuitous.

3

Quantemol-N

Running an **R**-Matrix calculation is complicated. Typically, with much guidance from others already versed in the UKRmol suite, it is a large task to become competent with the codes - especially for a fresh PhD student. Each subsequent program requires several inputs, which may or may not depend on the outputs of previous programs, and may have particular quirks which are slowly discovered by the user through experience. To someone new to the codes, all of this would be overwhelming, providing a user manual and the UKRmol suite would be unlikely to yield results quickly, with students historically taking entire PhDs to study a single molecule.

Quantemol-N was created to address this entrance barrier, enormously reducing the effort required to set up and run a calculation. This is achieved through a GUI wizard, guiding the user through a series of calculation options - with a little bit of experience, Quantemol-N can reduce the amount of setup to a matter of minutes, rather than weeks to months. This is possible since many of the inputs to various programs in the suite are entirely based on outputs of previous programs, whether that be counting outputs, rearranging data, or selecting subsets of data based on other parameters - all tasks computers are better than humans at. As an example of the extreme saving in effort afforded to the user, a standard set of inputs for an UKRmol electron scattering calculation contains about 2000 lines of input. While a photoionization calculation has a few fewer, at around 1300 lines in total. On top of this, if differential cross sections, or aligned cross sections are wanted, then these programs must be run for every energy

point. For `polyDCS`, this requires transposing the **K**-matrices from a per symmetry set of files into a per energy set of files - and then the input for each energy must point to the correct file, while having the correct dimensions of the various files - this amounts to ~ 15 extra lines of input per energy point. There is a similar addition for the aligned module. This is reduced to a standardised input file defining the calculation in fewer than 50 lines, where many can be omitted and default options used.

Quantemol-N removes all of the tedious and error prone steps of setup, leaving only the more subjective inputs, such as which basis set to use, how many orbitals to include, the range of energies to examine, and then, whether to run additional modules to give extra data. Quantemol-N then also provides a convenient in program plotting utility, to make it easy to quickly view ones' results, and perform various sanity checks on the results.

The need to perform these calculations in the first place stems from a lack of experimental data, since for many species, the experiments are difficult to perform (Tennyson et al., 2007). This issue is summarised nicely by Cukras et al. (2013):

> "Absolute cross section measurements are however difficult and tiresome, as extreme care has to be devoted to the control of experimental conditions, including density of the sample, geometry of the interaction region, detector efficiency, and the like. So actually rather few data are available for fundamental gaseous targets, notably the noble gases, with a stated accuracy of a few percent. The situation is much more difficult for less volatile or unstable species, many of scientific or technological importance, because of the above mentioned difficulty of precisely characterizing the density of the sample and focal volume."

My work on Quantemol-N has included incorporating software fixes, and physics additions (many of which are listed below), and also producing cross sections in a consultancy undertaking.

3.1 Software Changes

3.1.1 BE*f* scaled Born cross sections

Plane Wave Born (PWB) cross sections are good approximations at high energy, but at low energy they tend to be too large. This method provides a method of scaling these PWB cross sections, specifically at low energy, to improve the agreement with experiment Kim (2001).

The first improvement to the cross sections come from:

$$\sigma_{\mathrm{BE}} = \sigma_{\mathrm{PWB}} \frac{T}{T + B + E} \tag{3.1.1}$$

where σ_{BE} is the BE scaled born cross section (given by σ_{PWB}). T, B, and E are the incident electron energy, the binding energy, and the excitation energy, respectively. This simple scaling converges to 1 for large T, and has the effect of reducing the peak and shifting it to higher energy. This is already a significant improvement on a standard Born cross sections, for both atoms (Kim, 2001) and molecules (Kim, 2007) - for an idea of the improvement provided by this method, see these two papers, where examples of the better agreement with experiment are provided.

Originally, the task was to incorporate a small C++ program into Quantemol-N, adding BE scaled cross sections to the range of outputs. Quantemol-N is written in Java, running the Fortran UKRmol suite; the idea of including a third language into this mix was not appealing, and so the original program was rewritten in Java.

The original code obtained Born cross sections using equations from Kim (2007), eqs. (3.1.2) to (3.1.5):

$$\sigma_{\mathrm{PWB}} = \frac{4R\pi a_0^2}{T} \int_{Q_{\mathrm{min}}}^{Q_{\mathrm{max}}} \frac{RG_{fi}(Q)}{T} \mathrm{d}(\ln Q) \tag{3.1.2}$$

where the Born cross section is written in terms of the *generalised oscillator strength* (GOS), $G_{fi}(Q)$. R is the Rydberg energy, and Q is the momentum transfer, with its

minimum and maximum defined in eqs. (3.1.3) and (3.1.4).

$$Q = (Ka_0)^2 = a_0^2(k_i^2 + k_f^2 + 2k_i k_f \cos\theta) \tag{3.1.3}$$

$$Q_{\min/\max} = (K_{\min/\max} a_0)^2 = 2\frac{T}{R}\left[1 - \frac{E}{2T} \mp \sqrt{1 - \frac{E}{T}}\right] \tag{3.1.4}$$

where $Q_{\min}$ and $Q_{\max}$ take the $-$ and $+$ branches of the $\mp$.

The generalised oscillator strength, $G_{fi}(Q)$, is defined by

$$G_{fi}(Q) = \frac{E}{R}\frac{\left|\langle\psi_f| \sum_{j=1}^{N} \exp(i\mathbf{K}\cdot\mathbf{r}_j) |\psi_i\rangle\right|^2}{Q} \tag{3.1.5}$$

where the sumation is over all bound electrons, and ψ_i and ψ_f are the initial and final states of the target. An alternative to this was proposed by Vriens (1967), giving the GOS as a power series:

$$G_{fi}(x) = \frac{f}{(1+x)^{l+l'+5}}\left[1 + \sum_{m=1}^{\infty}\frac{c_m x^m}{(1+x)^m}\right] \tag{3.1.6}$$

where l and l' are the orbital angular momenta of the initial and final staes, c_m are expansion coefficients, and $x = Q/\alpha$, where α is a constant relating to the excitation and binding energies of the target electron (Lassettre, 1965). When multiconfiguration, or correlated target wavefunctions are used, the meaning of α is less apparent, and in some cases the same can be said for the angular momenta of the states. In these cases they can be used as fitting parameters, as done in Liu and Hagstrom (1993), matching experiment within 0.1% (for $Q \leqslant 1$) using only the leading term of eq. (3.1.6).

The scaling can be improved even further by using a more accurate oscillator strength, and scaling the cross section accordingly:

$$\sigma_{\mathrm{BE}f} = \frac{f_{\mathrm{accu}}}{f_{\mathrm{Born}}}\sigma_{\mathrm{BE}} \tag{3.1.7}$$

where the scaling accounts for the approximate oscillator strength used in the Born approximation. The *accurate* oscillator strengths can be taken from experiment, or a calculation, or in the case of Quantemol-N, they would be derived from the dipole

transition moments.

The original C++ code implemented this method of obtaining a PWB, numerically integrating in eq. (3.1.2) using the trapezium rule with a million trapeziums, and just the first term in eq. (3.1.6). Instead of this, the Born approximation described by Chu and Dalgarno (1974), as implemented in the `BORNCROSS` routine (Baluja et al., 2000) was used; eq. (3.1.8). This approximation has no power series, nor does it require an integration, significantly improving on the performance of the original method. It also uses the dipole transition moments directly, removing the requirement to manually include these later, for the final f scaling.

$$\sigma_{fi\ \mathrm{Born}} = \frac{8\pi d_{fi}^2}{3k_i} \ln\left[\frac{k_i + k_f}{k_i - k_f}\right] \tag{3.1.8}$$

where d_{fi} is the dipole transition moment for the $f \to i$ transition, and k_i and k_f are $\sqrt{T/R}$ and $\sqrt{T-E/R}$.

While the **R**-Matrix calculations are good at low and intermediate energies, these cross sections do not give accurate behaviour at low energy, where the Born approximation fails: they are explicitly for high energy. The solution to this is to match the cross sections at intermediate energies to provide a much broader energy range than either solution can provide individually. They are also only non-zero for dipole allowed transitions, for forbidden transitions the cross sections can be matched to exponentially decaying functions.

3.1.2 PolyDCS

The original inception of `polyDCS`, as described in Sanna and Gianturco (1998), was take the necesary elements from the scattering **K**-matrix, and then use them to calculate the the various cross sections. This is essentially a program which takes the calculation down a parallel route to the UKRmol outer region subroutines after the **K**-matrices have been created.

There are two important distinctions though, the first is the reason for implementing `polyDCS`: it provides cross sections rotationally and scattering angle resolved cross

sections, and the momentum transfer cross section. Unfortunately electronic excitation is not provided. On the other hand, `IXSECS` provides electronic excitations, but the cross sections are not resolved in angle or rotational excitation.

`polyDCS` is not a single routine for calculating the differential cross section, but a small collection of routines for different cases, where Sanna and Gianturco (1998) started with a subset of the final code for linear molecules, and extended it to a general code to deal with non linear molecules; the program has 4 paths, for linear, symmetric, asymmetric, and spherical top molecules, and then additionally applies a Born correction to the polar targets. This structure is potentially the cause of an issue with the low energy methane results, as discussed in the Methane Differential Cross Sections subsection, page 76, since approximations are applied to all molecules of a certain type.

Implementation

The inner workings of `polyDCS` are not important when creating a wrapper around it, only the creation of the inputs and parsing of the outputs. This is what Quantemol-N does with polyDCS, running it for each energy, having crafted the inputs for each energy.

There were two main steps in creating the necessary inputs, the first was transforming the **K**-matrices into the appropriate format. This was simply a case of taking the UKRmol outer region upper triangle **K**-matrices, and transforming them to be square, and also splitting the file containing all **K**-matrices for all energies into one for each.

The second task was less trivial, and involved obtaining the b_{lm} coefficients[1]: a required input, described in Sanna and Gianturco (1998). The process is now automated

[1]In much of the literature, the convention of whether the various labels of the $b_{\ell m}$ are superscript or subscript, as well as whether they are even included, changes regularly, both between papers, and inside individual papers. It is never mentioned why, and seems to be entirely aesthetic. Here they are referred to only as $b_{\ell m}$ since it is only the ℓ and m labels which concern us, but when being described in terms of quantities from various definitions, all labels are included as in the source material.

for each point group. They are referenced in part of a more specific coefficient,

$$\bar{b}^{p\mu}_{\ell hm} = \begin{cases} {}^{1}/_{\sqrt{2}} \; - 1^{m} \exp({}^{i\pi q(q-1)}/_{4}) b_{\ell hm} & m > 0 \\ b_{\ell hm} & m = 0 \\ {}^{1}/_{\sqrt{2}} \; - 1^{m} \exp({}^{i\pi q(q-1)}/_{4}) b_{\ell h|m|} & m < 0 \end{cases} \tag{3.1.9}$$

where the μ and p labels refer to the μ^{th} component of the p^{th} *Irreducible Representation* (IR), with h distinguishing between different bases.

Molecular orbitals can be written in terms of these (Gianturco and Thompson, 1976),

$$\phi_{\kappa}(\mathbf{r}_{\kappa}; R) = {}^{1}/_{r} \sum_{s}^{\infty} u^{\kappa} \alpha_{s}(\mathbf{r}_{\kappa}; R) X^{p\mu}_{\ell h}(\hat{r}_{\kappa}) \tag{3.1.10}$$

where X is a linear combination of spherical harmonics,

$$X^{p\mu}_{\ell h} = \sum_{m=-\ell}^{\ell} b^{m}_{\ell h} S^{mp}_{\ell}. \tag{3.1.11}$$

The $b_{\ell m}$ (ignoring the h labels here) coefficients are just the coefficients which describe the molecular orbitals in terms of the spherical harmonics, where in the case of Abelian point groups, they are always 1 or 0, and just specify which spherical harmonics comprise each IR (Altmann, 1957; Altmann and Bradley, 1963; Altmann and Cracknell, 1965; Altmann and Bradley, 1965)[1]. Comparing the IRs of the point groups to the real spherical harmonics, and collecting the relevant S^{m}_{ℓ} functions together for each IR, the $b_{\ell m}$ coefficients can be found, and a simple method for creating them with arbitrary ℓ and m was found. A full set of coefficients for $\ell <= 4$ is included in appendix A, along with rules for creating them for any arbitrary ℓ and m. The real spherical harmonics, are additionally included for reference in appendix B.

For examples of `polyDCS` being used, see figs. 2.10 to 2.13 and 2.17.

[1] These papers give some, but not all, of the $b_{\ell m}$ coefficients, and have varying sign conventions. They also provide some coefficients for non Abelian point groups.

3.1.3 Align

Before `Align`, the **R**-Matrix codes would give cross sections averaged over all molecular orientations. Several experimental observables are strongly dependant on the molecular alignment, such as *high harmonic generation* (HHG) and *re-scattering* (Harvey and Tennyson, 2009; Harvey, 2010). Studying the two processes together can give both nuclear and electronic dynamics resolved on the subfemptosecond timescale, with spatial resolution of an Ångstrom (Lein et al., 2002; Spanner et al., 2004; Zuo et al., 1996; Niikura et al., 2002, 2003).

Theory

The function of `align` can be explained by starting at the stationary wave function Ψ_i^+;

$$\Psi^+_{\Lambda_i S_i M_{S_i} \nu_i}(x'_1, \ldots, x'_N \sigma' \boldsymbol{r}) = \psi_i(x'_1, \ldots, x'_N)\chi_{\frac{1}{2}m_{s_i}}(\sigma')e^{i\boldsymbol{k}_i \cdot \boldsymbol{r}} + \Sigma_{\Lambda_j S_j M_{S_j} \nu_j m_{s_j}} \psi_j(x'_1, \ldots, x'_N)\chi_{\frac{1}{2}m_{s_j}} F_{\Lambda_i S_i M_{S_i} \nu_i m_{s_i} \Lambda_j S_j M_{S_j} \nu_j m_{s_j} \boldsymbol{k}_i \boldsymbol{k}_j}(\alpha, \beta, \gamma) e^{j\boldsymbol{k}_j \cdot \boldsymbol{r}}/|r| \tag{3.1.12}$$

where Λ_i, S_i, M_{S_i}, and ν_j are the quantum numbers describing the electronic state of the N electron target, and the same set plus m_{s_j} describe the $N+1$ electron system. Λ_i is the angular momentum projected on the molecular axis, S_i and M_{S_i} the spin and its molecular axis projection. ν_j is the symmetry of the state (gerade or ungerade), and m_{s_j} is the spin projection of the scattering electron. α, β, and γ are the Euler angles, defining the orientation of the molecule. The quantum numbers Λ_i, S_i, M_{S_i}, and ν_i are invariant through the collision, and will be represented simply by single label, I (or J, depending on the subscript) in subsequent equations for simplicity.

This is linked to the **T**-matrix by the standard relation (Morrison and Sun, 1995):

$$F_{I\boldsymbol{k}_i J\boldsymbol{k}_j} = 2\pi i T_{I\boldsymbol{k}_i J\boldsymbol{k}_j}(\alpha, \beta, \gamma)$$

The **T**-matrix given by the UKRmol codes is in the molecular frame, with an angular

momentum basis, and uses invariants to simplify the problem. The main legwork done by `Align` is this transformation from molecular frame to the lab frame.

Implementation

As for adding this functionality to Quantemol-N, it was simply a matter of providing `Align` with the relevant **T**-matrices, and a molecular orientation, and then sorting the substantial output - which is a cross section resolved in energy, α, β, γ, θ, and ϕ. There are not many quintuply differential results available to compare the results against, with the only one found being that of Senftleben et al. (2010), which is only at a single energy point of 200eV - at which a UKRmol calculation would not be appropriate. Integrating the provided results does reproduce the total cross sections, which while obviously not sufficient to prove correctness, is promising.

3.1.4 Photoionization

The removal of an electron from an atom, or molecule, by light - photoionization - is an important process in a wide range of natural phenomena. It can for example be the plasma initiator in a number of environments, or play a key role in radiative transport and ionization balance within plasmas.

Modeling these plasma processes requires accurate cross sections for the species in the plasma. Experimental results are, generally, widely available for stable species; but far less data is available for the radicals and ions which compose the typical plasma chemistry (Brigg et al., 2015).

Additionally, recent developments in experimental techniques, including *High Harmonic Generation* (HHG) spectroscopy (Baker et al., 2006; Smirnova et al., 2009; Haessler et al., 2010), the attosecond streak camera (Schultze et al., 2010), the *reconstruction of attosecond bursts by interference of two photon transitions* (RABBIT) method (Paul et al., 2001; Klünder et al., 2011), and laser induced electron diffraction (Spanner et al., 2004; Meckel et al., 2008; Blaga et al., 2012), have improved scientists' ability to observe non-equillibrium electron dynamics on their natural attosecond timescales. These processes often involve intense IR or XUV bursts, usually ionizing

the targets. The attosecond dynamics of the systems can then break the process down into distinct steps, such as ionization, continuum dynamics, recombination/scattering (Ivanov et al., 1996; Jin et al., 2009; Ivanov and Smirnova, 2011). Modelling the dynamics of these stages requires a description of the photoionization dipoles, resolved in both energy and orientation, along with scattering amplitudes (Harvey et al., 2014a,b).

Theory

The diatomic implementation of the UK molecular **R**-matrix codes was adapted a long time ago to study photoionisation(Tennyson et al., 1986; Tennyson, 1987; Tennyson and Chandra, 1987). However, this adaption was not included in the development of either the UK (Morgan et al., 1998) or Bonn (Pfingst et al., 1994) polyatomic codes. Subsequently, implementations were developemed by Hiyama and Kosugi (2005); Tashiro (2010), which have been used successfully to study X-ray photoionization (Hiyama and Kosugi, 2015; Tashiro et al., 2012). Recently the polyatomic UKRmol codes have been adapted by Harvey et al. (2014b) to treat photoionization, allowing for the calculation of observables resolvable in the final state of the resultant ion, the photon polarisation and energy, the molecular orientation, and the electron emission direction. This required considerable new technical developments (Rouzée et al., 2014) because of the use of an efficient, but non standard formalism used to generate the wave functions in the modern implementation of the codes (Tennyson, 1996a). It is these modifications and additions which were incorporated into Quantemol-N, giving it the ability to calculate photoionization observables.

There are also other theoretical methods available for calculating these observables. These methods include use of single-centre expansions (Tao et al., 2009; Demekhin et al., 2011), and *time-dependent density functional theory* (TDDFT) (Gross and Kohn, 1990; Stener et al., 2007), both of which struggle to account fully for Feshbach resonances (Krueger and Maitra, 2009). Closer in spirit to the **R**-matrix method used here are the complex Kohn (Lynch and Schneider, 1992; Orel and Rescigno, 1997) and Schwinger (Lucchese et al., 1986; Stratmann and Lucchese, 1995; Stratmann et al., 1996) variational methods - for which numerous cross comparisons, for both electron

scattering (Baluja et al., 1985; Schneider and Collins, 1985; Lima et al., 1985) and photoionization (Jose et al., 2014), have been carried out and suggest that there is little difference n the attained results. The **R**-matrix method is particularly efficient when considering a large nubmer of energies, which is important when resolving structures due to resonances.

The photoionization cross section is, ultimately described by, within the length gauge approximation, the following equation, described in full in Harvey et al. (2013, 2014b) and Tennyson (1988);

$$\frac{\mathrm{d}\sigma_{if}}{\mathrm{d}\boldsymbol{k}_f} = 4\pi^2 \alpha a_0^2 \omega |\boldsymbol{d}_{if}(\boldsymbol{k}_f) \cdot \hat{\boldsymbol{\epsilon}}|^2 \tag{3.1.13}$$

where α is the fine structure constant, a_0 is the Bohr radius, ω the photon energy in atomic units, and $\hat{\boldsymbol{\epsilon}}$ is the polarisation direction of the incident photon in the molecular frame. $\boldsymbol{d}_{if}(\boldsymbol{k}_f)$ is the molecular frame transition dipole between the initial state, i, and a single continuum state, f, as a function of the ejected electron momentum, $\boldsymbol{k}_f$;

$$\boldsymbol{d}_{if}(\boldsymbol{k}_f) = \langle \Psi^{(-)}_{f\boldsymbol{k}_f} | \boldsymbol{d} | \Phi^N_i \rangle \tag{3.1.14}$$

where $\Psi^{(-)}_{f\boldsymbol{k}_f}$ is the final continuum state, Φ^N_i is the intial bound state, and $\boldsymbol{d}$ is the dipole operator, which, again in the length gauge, in spherical vector form is:

$$\boldsymbol{d}_q = \left(\frac{4\pi}{3}\right)^{\frac{1}{2}} \sum_{i=1}^{N} r_i Y_{1,q}(\hat{\boldsymbol{r}}_i) \tag{3.1.15}$$

where $\boldsymbol{d}_q$ is the dipole operator for polarisation $q = \pm 1$ for circularly polarised photons, and $q = 0$ for linear polarisation.

For bound / initial states confined to the inner region, the integral in eq. (3.1.14) can be restricted to the inner region, and both the initial and final state can be expanded in terms of their inner region, energy independent, solutions $\psi^{(N)}_k$.

$$\Psi^{(-)}_{f\boldsymbol{k}_f} = \sum_k A_{fk}(\boldsymbol{k}_f) \psi^{(N)}_k \tag{3.1.16}$$

$$\Phi_i^N = \sum_k B_{ik}\psi_k^{(N)} \tag{3.1.17}$$

Substituting these into eq. (3.1.14), we obtain

$$\boldsymbol{d}_{if}(\boldsymbol{k}_f) = \sum_{kk'} A^*_{fk}(\boldsymbol{k}_f)\langle\psi_k^{(N)}|\boldsymbol{d}|\psi_{k'}^{(N)}\rangle B_{ik'} \tag{3.1.18}$$

In the R-Matrix formulation, this is defined in the angular momentum basis for the ejected electron, expanding this in terms of partial waves gives:

$$\boldsymbol{d}_{if}(\boldsymbol{k}_f) = \sum_{kk'}\sum_{l_f m_f} i^{-l_f} e^{i\sigma_{l_f}} Y_{l_f,m_f}(\hat{\boldsymbol{k}}_f)\langle S_f M_{S_f} \frac{1}{2} m_{s_f}|SM_S\rangle$$
$$A^*_{fl_f m_f k}(E)\langle\psi_k^{(N)}|\boldsymbol{d}|\psi_{k'}^{(N)}\rangle B_{ik'} \tag{3.1.19}$$

Where σ_{l_f} is the Coulomb phase; $\arg(\Gamma(l_f+i\eta_f+1))$, where $\eta_f = -\frac{Z-N+1}{k_f}$ and $Z-N+1$ is the residual charge of the system. The Clebsch-Gordon coefficient deals with the spin coupling of the continuum electron and the ion.

All of the above equations are in the molecule frame, to obtain scattering variables we need to transform to the lab frame, which is done using the Wigner rotation matrices, $\boldsymbol{D}^l(\alpha,\beta,\gamma)$.

$$\boldsymbol{d}'_{if}(\boldsymbol{k}'_f) = \sum_{l_f m'_f m_f} i^{-l_f} e^{i\sigma_{l_f}} Y_{l_f,m'_f}(\hat{\boldsymbol{k}}'_f)\langle S_f M_S \frac{1}{2} m_{s_f}|SM_s\rangle D_{m'_f m_f}\boldsymbol{d}_{fl_f m_f i}(E)\boldsymbol{D}^l \tag{3.1.20}$$

Where $\boldsymbol{d}_{fl_f m_f i}$ is the partial wave dipole;

$$\boldsymbol{d}_{fl_f m_f i}(E) = \sum_{kk'} A^*_{fl_f m_f k}(E)\langle\psi_k^{(N)}|\boldsymbol{d}|\psi_{k'}^{(N)}\rangle B_{ik'} \tag{3.1.21}$$

Using this, the angularly resolved photoionization cross section can be produced, or it can be averaged, to give partial photoionization cross sections;

$$\sigma_{fi}(E) = \frac{4}{3}\pi^2\alpha a_0^2\omega \sum_{q l_f m_f} |d_{q f l_f m_f i}(E)|^2 \tag{3.1.22}$$

Computationally, the process is broken down into a few steps, with eqs. (3.1.13) and (3.1.18) summarising the situation nicely. First, the energy independent transition

dipoles are calculated by `cDenprop`(Harvey et al., 2013), with the option of including the bound coefficients; $\langle\psi_k^{(N)}|\boldsymbol{d}|\psi_{k'}^{(N)}\rangle B_{ik'}$. The bound coefficients, $B_{ik'}$, are, unsurprisingly, produced by `Bound`. These are then provided as input to `RSolve`, and the new outer region routine: `CompAK`, which calculates the $A^*_{fk}(\boldsymbol{k}_f)$ coefficients, and then the partial wave dipoles, $\boldsymbol{d}_{fi}(\boldsymbol{k}_f)$. `DipElm` then gives $\frac{\mathrm{d}\sigma_{if}}{\mathrm{d}\boldsymbol{k}_f}$ via eq. (3.1.13).

The photoionization cross section has a convenient property; when averaged over molecular orientation and spin, the following is true:

$$\left(\frac{\mathrm{d}\sigma}{\mathrm{d}\Omega}\right)_{\text{Av.}} = \frac{\sigma}{4\pi}\left[1+\beta P_2(\cos\theta)\right] \tag{3.1.23}$$

where β is the asymmetry parameter, and P_2 is the second Legendre polynomial (Tennyson et al., 1986). As a result of this, if the measurement is performed at at an angle such that $P_2(\cos\theta)$ is zero, and so the measured result is independent of β. This angle is $\sim 54.74°$ and known as the *magic angle*. This greatly reduces the experimental difficulty compared to electron scattering, as discussed in section 1.2.1.

Examples

Having implemented `cDenprop` and `DipElm` in Quantemol-N, it was just a matter of testing everything was in order. Several examples of QN run photoionization follow, the following calculations are quick examples, to demonstrate the simplicity of the newly implemented functionality.

The results below all include a Quantemol-N calculated curve, compared to experiment. As these calculations involve ions, they all involve an infinite number of resonances leading up to each threshold; these are not seen in the same form experimentally, as nuclear motion broadens the resonances, merging them into broader, smaller features. The UKRmol codes, sitting on a fixed nuclei approximation, cannot account for this, though a reasonable approximation can be made by applying a Gaussian convolution, though if the filter width (i.e. σ in the convolution) is too large, then all resonances will be removed, which may or may not be preferable, and is dependant of the specifics of the system (Gorfinkiel and Tennyson, 2005; Meyer et al., 1995).

One aspect of photoionization calculations is that they seem to converge much more

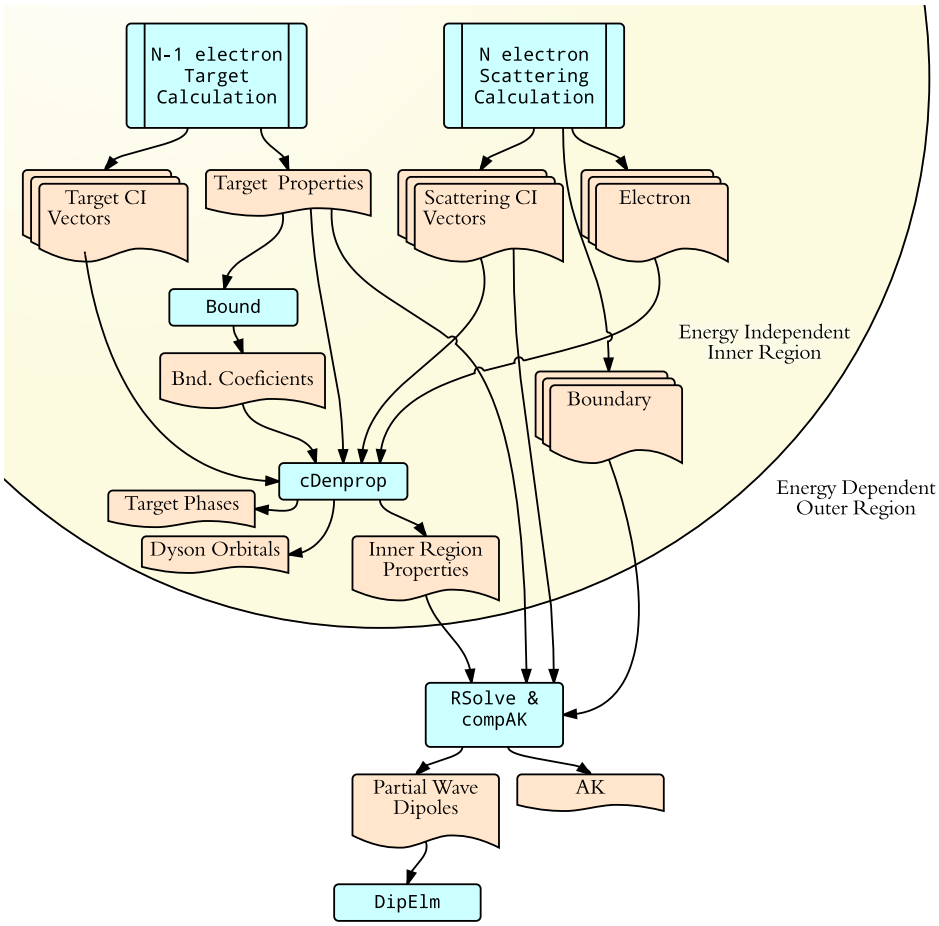

Figure 3.1: Additional routines for a photoionization calculation. Blue rectangles represent programs, blue rectangles with a double border represent a collection of programs, with arrows denoting input and output files used, or created during the calculation. The final program run, `DipElm`, produces the photoionization cross sections, both averaged and resolved for molecule orientation, photon polarisation, and electron ejection angle. It should also be noted that use of the `RSolve & CompAK` program also requires the Inner/Outer region interface program, `SwInterf`.

slowly as a function of increasing model size than equivalently sized electron-molecule scattering calculations. This is demonstrated in the CN^- and C_2H^- sections below - the anion photodetachment calculations are used as the scattering calculation is from a target absent one electron, which means that for a neutral photoionization calculation the target would be an ion, and there would be an infinite series of resonances before each threshold - demonstrating the convergence when the cross sections are littered with resonances is difficult, from a visualisation standpoint.

The results here for N_2 and CH_4 have also been presented in Brigg et al. (2015).

H_2

Being the simplest molecule available, Hydrogen was an obvious first choice test case, and so a simple model utilising an active space of [1-5 σ, 1 π]^2 for both the neutral, and ionic system, and augmenting the continuum basis with 10 virtual orbitals. The calculation was done with the cc-pVQZ basis set, with an R-Matrix radius of 12 $a.u.$ and taking the first 10 states per symmetry. Ionization to the first 7 states of the H_2^+ ion are considered, as above this the contribution is negligible.

The results are presented in fig. 3.2. In general, the agreement with experiment is good. There is a discrepancy however; at low energy, the cross section should fall to zero at the ionization threshold - a possible explanation for this is that the R-Matrix calculations use a fixed nuclei approximation, the effect of which can be seen in Flannery and Öpik (1965), with the ratio of charges and masses involved in H_2 and H_2^+, it is likely this is the case where the effect is most prominent. The Gaussian convolved curve, – –, in fig. 3.2, agrees excellently with the experimental results of Samson and Haddad (1994).

N_2

Figure 3.3 presents the photoionization cross sections and compares them with experiment. The agreement with the experimental results is generally good. Both theory and experiment show sharp features which are caused by quasi-bound states lying in the continuum generally called resonances. Here the resonances are slightly different

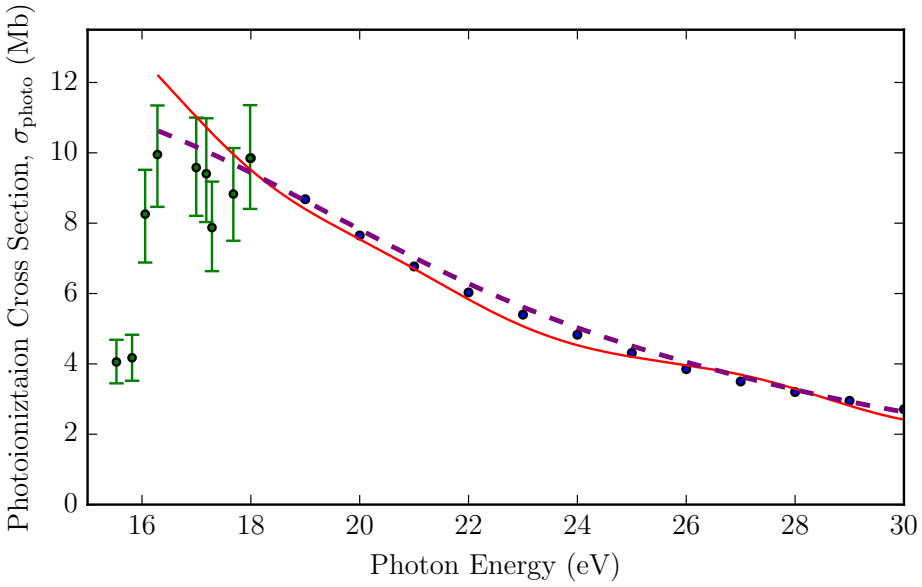

Figure 3.2: H_2 photoionization cross section, —, and Gaussian convolved PI cross section ($\sigma = 3$eV), – –; and two sets of experimental results: • Wainfan et al. (1955); and • Samson and Haddad (1994). The Samson and Haddad (1994) experimental results are actually photoabsorption cross sections; the Wainfan et al. (1955) results include the photoionization efficiency, which tends to 100% at the top end of the energies they examined, so it is not a problem above 18eV.

from those shown in fig. 3.2, with considerable resonance series' appearing in the lower 0.5 eV of the energy ranges in figs. 3.3 and 3.4. At higher energy, a correct handling of the resonances is less important - by merit of there being fewer of them, but at the lower end of the scale there are many, and so since the Gaussian convolution is more of an approximation the agreement is not as good for the first few eV above threshold.

N_2 partial cross sections

Figures 3.4 and 3.5 show partial cross sections for photoionizaiton parallel and perpendicular to the molecular axis, respectively. Of the the two partial cross sections contributing the majority one overestimates, and the other under estimates, when compared with the experimental results (Samson et al., 1977; Wainfan et al., 1955).

There are several possible explanations for this. One potential explanation, made evident by the fact that the total cross section is in good agreement with experiment, which suggests that the issue could be explained by the deconvolution of the total cross section into the relevant partial cross sections (the method used is described in Samson

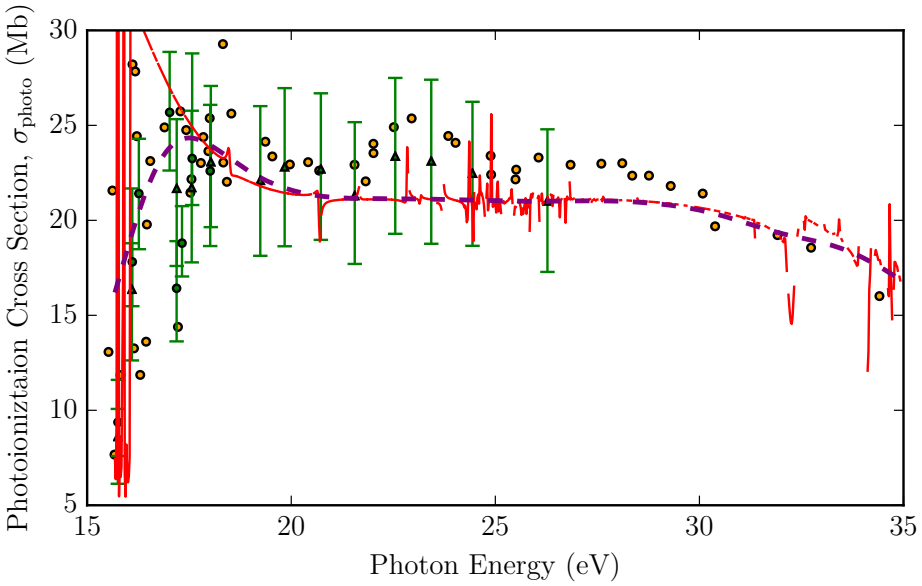

Figure 3.3: N_2 photoionization cross section, —, and Gaussian convolved PI cross section (σ = 0.5eV), – –; and the experimental results: 5cm ion chamber, with 10Å^2 resolution ▲; and 3cm ion chamber, with 5Å^2 resolution •, both from Wainfan et al. (1955). Plus the experimental results of Samson et al. (1977): •.

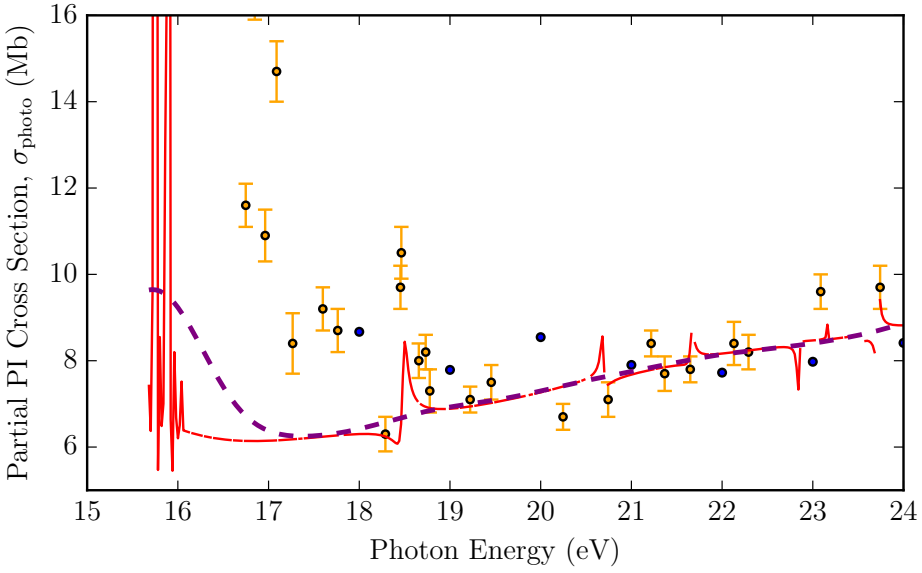

Figure 3.4: N_2 Partial photoionization cross section to final ionic state $X^2\Sigma_g^+$, —, and Gaussian convolved PI cross section ($\sigma = 0.5$eV), – –, compared with the experimental results of Samson et al. (1977), •; and • of Hamnett et al. (1976)

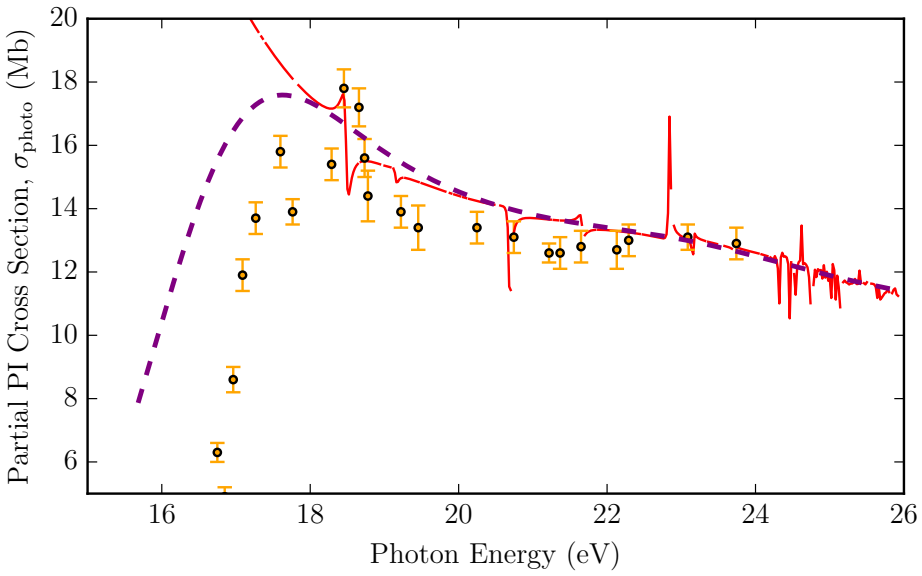

Figure 3.5: N_2 Partial photoionization cross section to final ionic state $X^2\Pi_u^+$, —, and Gaussian convolved PI cross section ($\sigma = 0.5$eV), – –; and the experimental results of Samson et al. (1977): •.

et al. (1975)), is that the branching ratios used in Samson et al. (1977) are slightly wrong. It is also possible that calculation is wrong - though that the errors on the two partial cross sections cancel each other out perfectly seems unlikely, and would be too serendipitous. A more likely explanation of an error in the calculation would be that the two channels are strongly coupled, and this coupling is not fully represented in the model.

The calculation was done using the cc-pVTZ basis set, an R-matrix radius of 12.0 a_0, an active space of [1 σ_g, 1 σ_u]^2[2-4 σ_g, 2-3 σ_u, 1 π_u, 1 π_g]^{12}, taking the first 105 states.

CH_4

Figure 3.6 shows our results for methane, and comparisons with experiment. A total cross section was not presented in the literature, but the X→T_2 partial cross section is the only contributing to the total cross section until the next threshold at approximately 25 eV, above which it makes up >90%. These partial cross sections leaving the ion in higher excited states were also presented in Backx and Van der Wiel (1975) and Van der Wiel et al. (1976), and are also accurately reproduced by Quantemol-N.

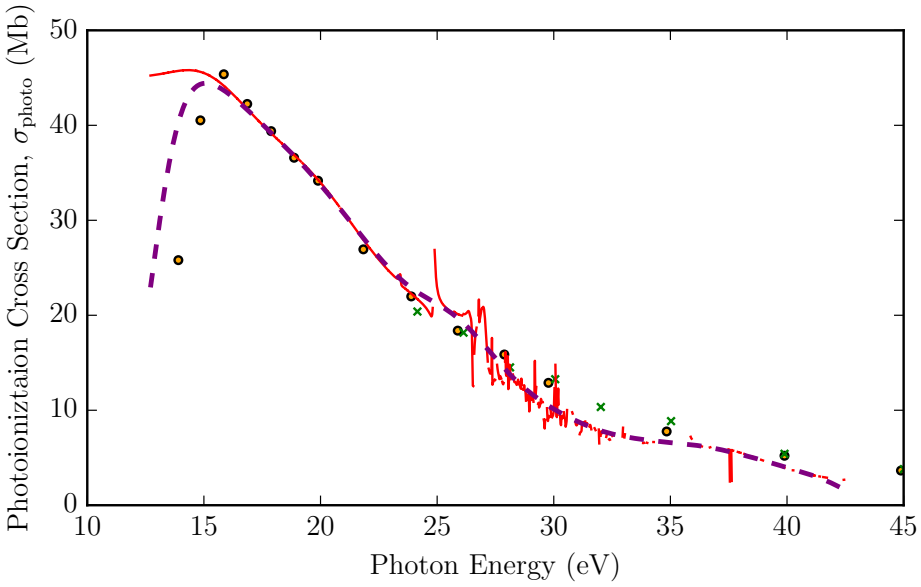

Figure 3.6: CH_4 Partial photoionization Cross Section to final ionic state T_2, —, and Gaussian convolved cross section (σ = 1eV), – –; and the experimental results of Backx and Van der Wiel (1975): •; and Van der Wiel et al. (1976): ×.

The calculation used an active space of [1-2 a_1]^4[3 a_1, 1-3 t_1]^6 with all states up to 20 eV, with an **R**-matrix radius of 12.0 a_0, and using the cc-pVTZ basis set.

3.1.5 Photodetachment

The following anions were examined as part of a series of tests on the new routines, and to test the adaptation of Quantemol-N to treat anions. Electron scattering from anions is fully possible with the UKRmol codes (Halmová and Tennyson, 2008), but

Quantemol-N's implementation did not include this as a possibility. In the same way a UKRmol photoionization calculation requires that a regular electron scattering calculation be performed first - to obtain the necessary scattering variables used to describe the dipoles - a photodetachment calculation requires that electron scattering from an anion be performed. The procedure is otherwise the same. This subsection and the following one contain photodetachment cross sections, and demonstrations of the nature of the convergence of photoionization / photodetachment calculations.

The molecules CN^- and C_2H^- are two small anions found in the interstellar medium. Little experimental or theoretical data for photodetachment of these species exist (Best et al., 2011), though the simple asymptotic (empirical) formula of Millar et al. (2007):

$$\sigma_{\text{det.}}(\epsilon) = \sigma_\infty \sqrt{1 - {}^{E_A}/_{\epsilon}} \tag{3.1.24}$$

where ϵ is the photon energy, E_A the electron affinity or the corresponding neutral species / photodetachment threshold, and σ_∞ the cross section as $\epsilon \to \infty$, can be used to describe the photodetachment cross section in the threshold region, where the range of validity has been discussed before (Farley, 1989). This formula converges to the Wigner threshold law for $\ell = 0$ photodetachment (Best et al., 2011). In the absence of more data, this empirical formula is often fit to experimental data to obtain E_A, and/or extend the data from the measured cross section down to threshold for use in models. Problems present themselves however when the data contains resonances, so if the experiments' measurement energies are only a small amount larger than threshold, where resonances are common, fitting data with this model will not necessarily be valid. Additionally, σ_∞ is also required, which is estimated (in the original paper of Millar et al. (2007) it is estimated to be 10 Mb for all C_nH^- where $2 \leqslant n \leqslant 10$). The results present for CN^- (Kumar et al., 2013) and C_2H^- (Best et al., 2011) are exclusively around threshold, owing to the use of UV lasers[1].

[1]Though Best et al. (2011) at least were able to study the threshold behaviour in more detail, where the energy range is within the tuning range of a single laser.

CN^-

In an absence of an abundance of experimental or theoretical data to compare against, it is important to test that calculations are in a converged state - that changing the various input parameters does not illicit a large change. When an experimental cross section is known, it is actually possible to use calculation input parameters as fitting parameters[1] - electron scattering codes have *many* inputs, and so there is an enormous range of inputs that could be explored to obtain a fit to wildly differing data. This flexibility means that when there is little to compare results to it can be difficult to be confident with the results. The solution to this is a similar process as was used in testing the convergence of the model in sections 1.5 and 2.2 - only one cannot aim for known results, only a convergence of the model.

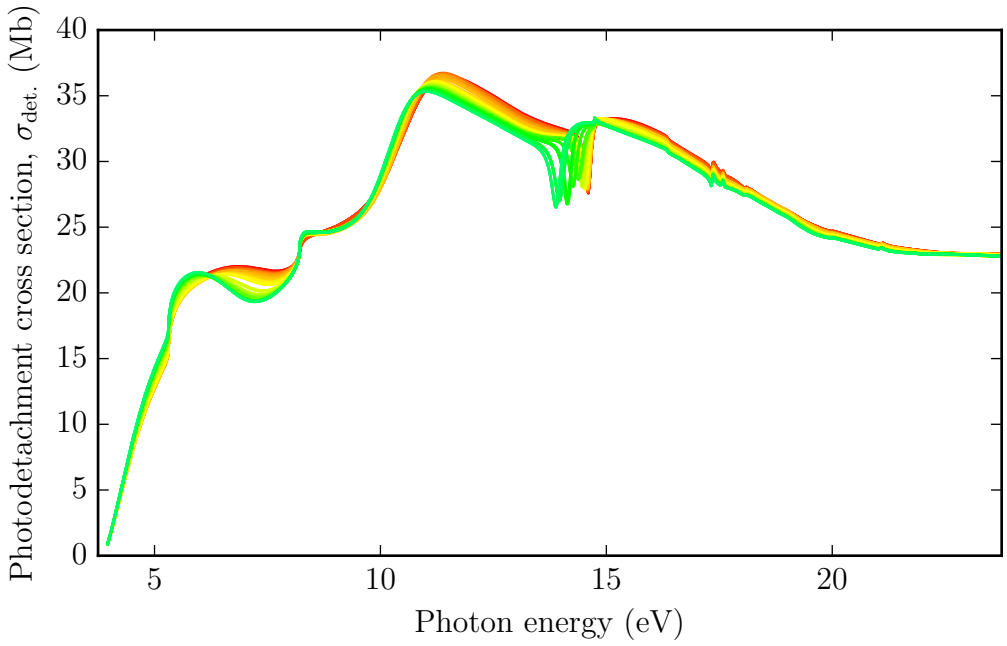

Figure 3.7: A series of CN− photo detachment cross sections, all with the active space [1-3σ]^6[4-7σ, 1-2π]^7, using the cc-pVQZ basis set. The lines follow the colour gradient representing the number of states included, ranging from 60 to 140.

Two examples of convergent calculations presented here, figs. 3.7 and 3.8, examining

[1] Although the effect is often non linear and complicated.

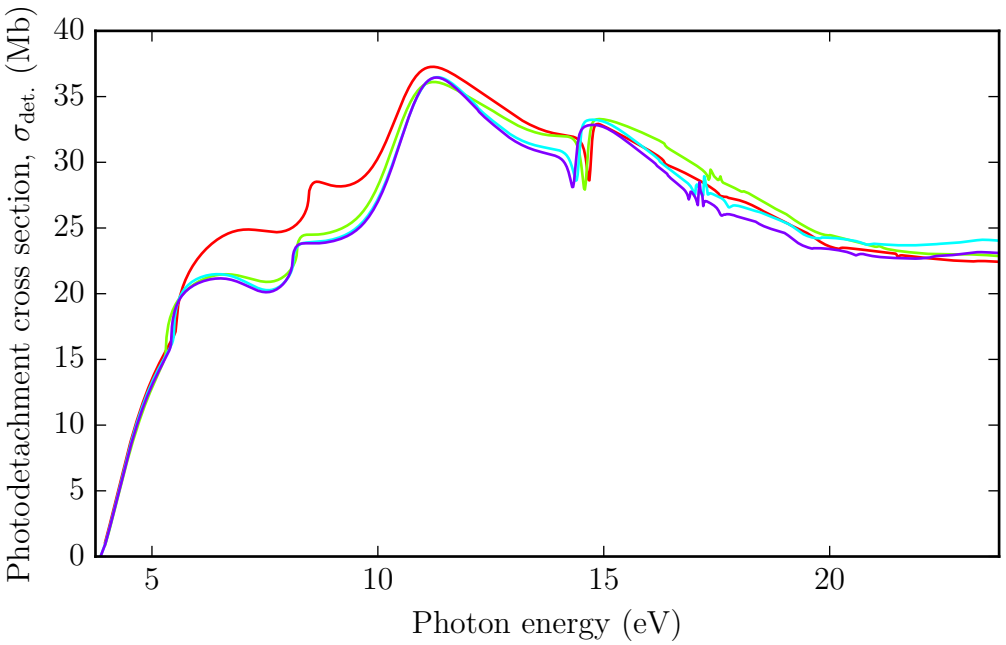

Figure 3.8: A series of CN− photo detachment cross sections, each including all states present up to 25.0 eV, for 4 different CAS sizes: ■ [1-3σ]^6[4-6σ, 1-2π]^7; ■ [1-3σ]^6[4-7σ, 1-2π]^7; ■ [1-3σ]^6[4-7σ, 1-3π]^7; ■ [1-3σ]^6[4-8σ, 1-3π]^7.

the total cross section as a result of varying the number of states included (fig. 3.7) and the number of orbitals included in the CAS (fig. 3.8). 80 separate calculations were performed with a CAS of [1-3σ]^6[4-7σ, 1-2π]^7 with the number of states being varied from 60 to 140[1] (the tediousness of this task is greatly reduced via Quantemol-N). Additionally, 4 calculations were performed for CASs of [1-3σ]^6[4-5σ, 1π]^7 up to [1-3σ]^6[4-8σ, 1-3π]^7. All calculations used the photodetachment threshold energy of 3.862 ± 0.004 eV from Bradforth et al. (1993). Similar tests were also done to examine the dependence on the basis set, with different sets giving rise to differences of about 15% - however this is a difference between the smaller and larger basis sets, as one tests the cc-pVnZ sets, increasing n, the result converges, with a similar result for the Pople sets. The final basis set used was cc-pVQZ. The number of deleted orbitals was also checked for the larger active space tests, to make sure none of the features were non physical remnants of an incomplete continuum basis (as in fig. 2.16), and no issues were found.

Figure 3.9 gives the total photodetachment cross section along with the single ex-

[1] Which is all states up to 30.5 eV above the ground state.

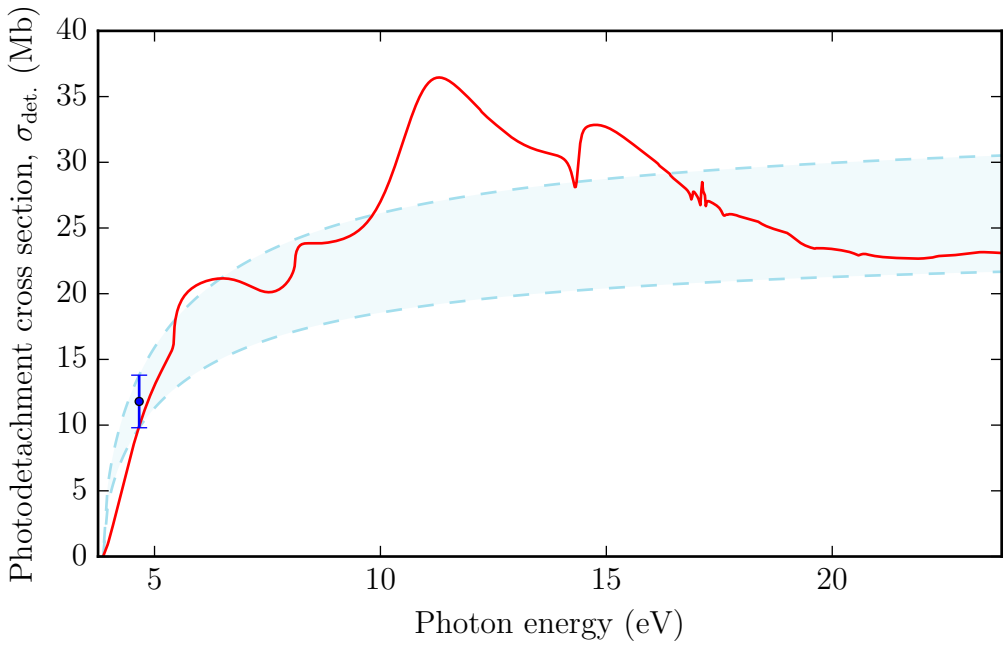

Figure 3.9: CN^- total photodetachment cross section. Quantemol-N result: ■; and experimental result of Kumar et al. (2013): •, and the ▭ region shows the potential range of fits to eq. (3.1.24) matching the experimental data and the known threshold.

perimental data point of Kumar et al. (2013): $11.8 \pm (0.3)_{\text{stat}}\ (1.7)_{\text{sys}}$ Mb at 266 nm (4.66 eV). Fitting[1] eq. (3.1.24) to the extremes of the errorbar for this point demonstrates a range of σ_∞ suggested by the experimental data, which seems to agree with the calculated cross section. In addition to this the partial photodetachment cross sections are included in fig. 3.10 (though there is unfortunately no data to compare against).

C_2H^-

There is slightly more data available for C_2H^-, in that there is more than one data point. Additionally there are other theoretical results to available to compare with. All of the same convergence tests performed for CN^- were also performed here, with the same results - roughly the same number of states and size of active space gave satisfactory convergence of the model, which is not surprising, as the molecules are iso-electronic.

[1] Fitting is done simply by minimizing the L^2 norm of the differences. It should be noted that fitting a simple form such as in eq. (3.1.24) to a small number of data points and using it for extrapolation could have a limited use in complex system - i.e. it will never include features due to resonances.

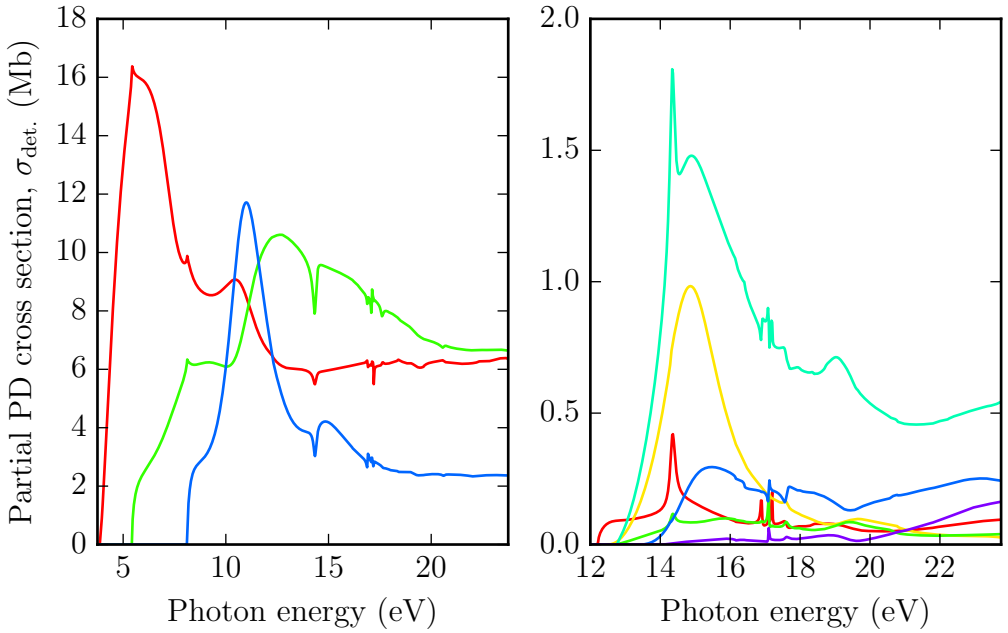

Figure 3.10: CN^- partial photodetachment cross sections, leaving the neutral in the following states, for the left panel: X $^2\Sigma^+$ ■; A $^2\Pi$ ■; B $^2\Sigma^-$ ■; and right: C $^2\Pi$ ■; D $^2\Sigma^+$ ■; E $^2\Pi$ ■; F $^2\Sigma^+$ ■; G $^2\Pi$ ■; H $^2\Sigma^+$ ■;

The final calculations performed, presented in figs. 3.11 and 3.12, used the cc-pVQZ basis set, an active space of [1-3σ]^6[4-8σ, 1-3π]^7, and all states included up to 25 eV. An additional 3000 energy points were studied for the first 1.5 eV above threshold, as this region contains the experimental data, and a resonance feature - an advantage of the energy independence of the outer region of the UKRmol codes.

The cross sections obtained here contain a prominent resonance feature - also replicated by the complex Kohn results of Douguet et al. (2014) - which seems to match up almost perfectly with the single experimental point at the same energy. This is not necessarily a sign that everything else is correct, as the sharp feature will be smoothed by a. nuclear motion, and b. an additional smoothing effect coming from the difference in geometries of the neutral and anionic states of C_2H. Best et al. (2011) also discuss a potential invalidity of the empirical formula here, as the C_2H^- ($^1\Sigma^+$) $\rightarrow$ C_2H ($^2\Sigma^+$) transition is forbidden for an s-wave electron, which they argue is not important due to the strong vibronic coupling of the A $^2\Pi$(which can be produced with s-wave scattering) to the ground state may explain this though. In addition to this though,

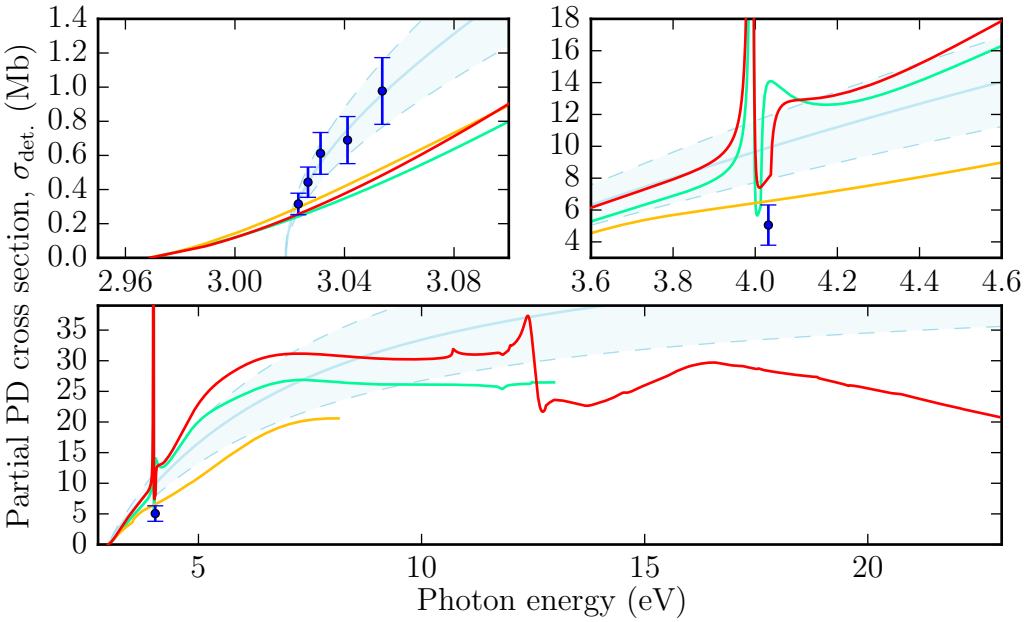

Figure 3.11: C_2H^- total photodetachment cross section, Quantemol-N result ■; compared to the results of the complex Kohn method with ■ and without ■ a Franck-Condon factor (Douguet et al., 2014), and experimental results of Best et al. (2011): •. The ■ region shows the potential range of fits to eq. (3.1.24).

the neutral molecule has a dipole moment, and so p-wave scattering is considerably more important, perhaps even dominant at very low energy - it is not clear whether eq. (3.1.24) is valid here, and perhaps a contribution from the p-wave scattering should be included instead;

$$\sigma_{\text{det.}}(\epsilon) = \sigma_\infty \left[a(1 - {}^{E_A}/_{\epsilon})^{1/2} + (1-a)(1 - {}^{E_A}/_{\epsilon})^{3/2} \right] \tag{3.1.25}$$

this can be fit to the experimental data near threshold to agree very well with the calculated results, but with the data points being so close together, with relatively large error bars, it is easy to fit many different curves within the uncertainties - more experimental points would be needed to determine the form.

The uncertainty in the applicability of the threshold laws, along with the lack of results available for other species makes the ability to calculate these cross sections a useful addition, and while results may not be perfect, with it being difficult to validate calculated cross sections in the absence of any other data, it is almost certainly better

than approximating all photodetachment processes using eq. (3.1.24) and setting $\sigma_\infty =$ 10Mb in all cases.

As before, the partial photodetachment cross sections are also provided in fig. 3.12, where the majority of the total photodetachment cross section comes from the first 2 states.

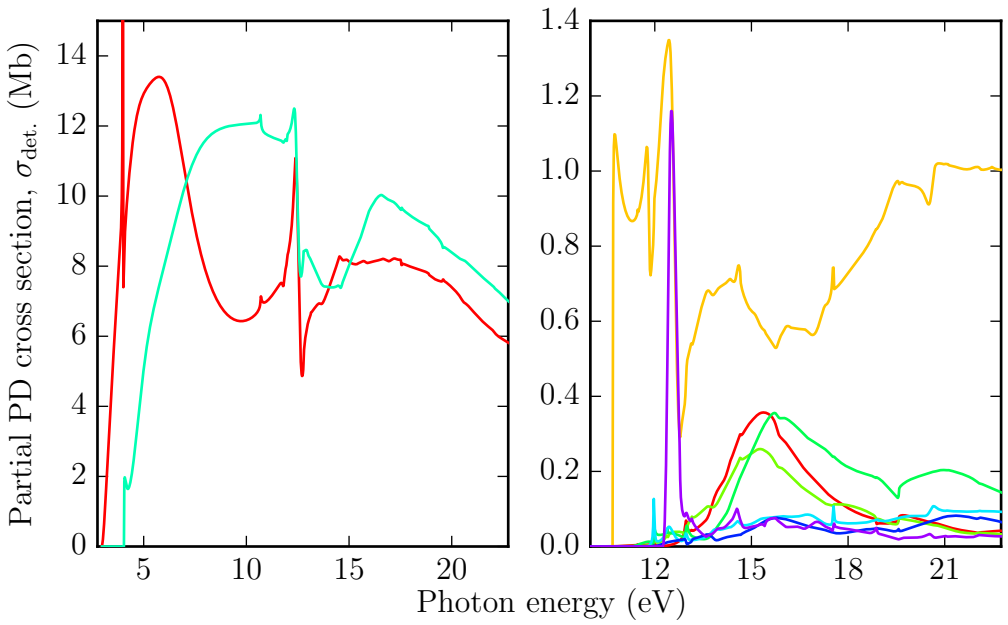

Figure 3.12: C_2H^- partial photodetachment cross sections, leaving the neutral in different neutral states. In the left panel: X $^2\Sigma^+$ ■; and A $^1\Pi$ ■, and right: B $^2\Pi$ ■; C $^2\Sigma^+$ ■; D $^2\Sigma^+$ ■; E $^2\Pi$ ■; F $^2\Pi$ ■; G $^2\Sigma^+$ ■; H $^2\Pi$ ■;

3.1.6 QN Express

One of the key inputs for Quantemol-N, and indeed the R-Matrix suite, is a description of the molecular geometry (and along with this the symmetry). Typically, the symmetry input is taken from some source on the internet, with several databases existing. Of these, a very popular one is the *NIST Computational Chemistry Comparison and Benchmark Database* (Johnson III, 2013), which as of writing, contains 1591 species, ranging from H^- to Coronene ($C_{24}H_{12}$). For each species available, there is a wealth of information, such as various enthalpies, entropies, molecular properties, and geometries

- for both ground states and excited states, along with vibrational energies, frequencies, and electrostatic properties. The range of available data does vary from molecule to molecule, but it is generally high.

For users less familiar with molecular geometry, correctly orienting a molecule and selecting the symmetrically non-redundant atoms is not always trivial, but at the same time is a problem which can be solved programatically, this was the driving force behind the creation of this tool.

If there is a geometry available, then it is retrieved from the database. If there is no geometry available, then one needs to be generated. the program `MolPro` (Werner et al., 2012) is capable of minimising molecular geometries, using various different algorithms, but it does require a somewhat sensible initial guess. This is done by taking a set of bonds from the user (a simple list of the form `C1 H1, C1 H2, ..., etc.`) to build a graph of the molecule, to which a Fruchterman-Reingold force directed graph layout algorithm is applied (Kobourov, 2012) in three dimensions. This is algorithm essentially appoints repulsive charges to each of the graph nodes (the atoms), and a spring contant, k, to each of the bonds, and then minimises the energy of the system. It is designed to be used to space graphs out aesthetically, but works very well for this purpose too. Unfortunately the same repulsive charge is applied to each node, this does not matter, as it is only an initial guess for a more thorough quantum chemistry optimisation; this geometry is then provided as the input for `MolPro` to do a robust geometry optimisation.

Now we have the geometry of the molecule. The next input in an `UKRmol` calculation is to determine the molecular symmetry (and select the non redundant atoms). Because the codes are limited to Abelian groups only, there is a relatively simple chain of tests which leads us to the correct symmetry for any given molecule - shown in fig. 3.13. When the molecule is already aligned correctly for the various symmetry operations, this is trivial. When it is not, it is a little bit more involved, a breakdown of the process follows.

Starting with an unoriented molecule, create a set of new orientations, rotated such that the vector $\overrightarrow{OX}$ is along the z axis, where O is the origin, and each orientation has

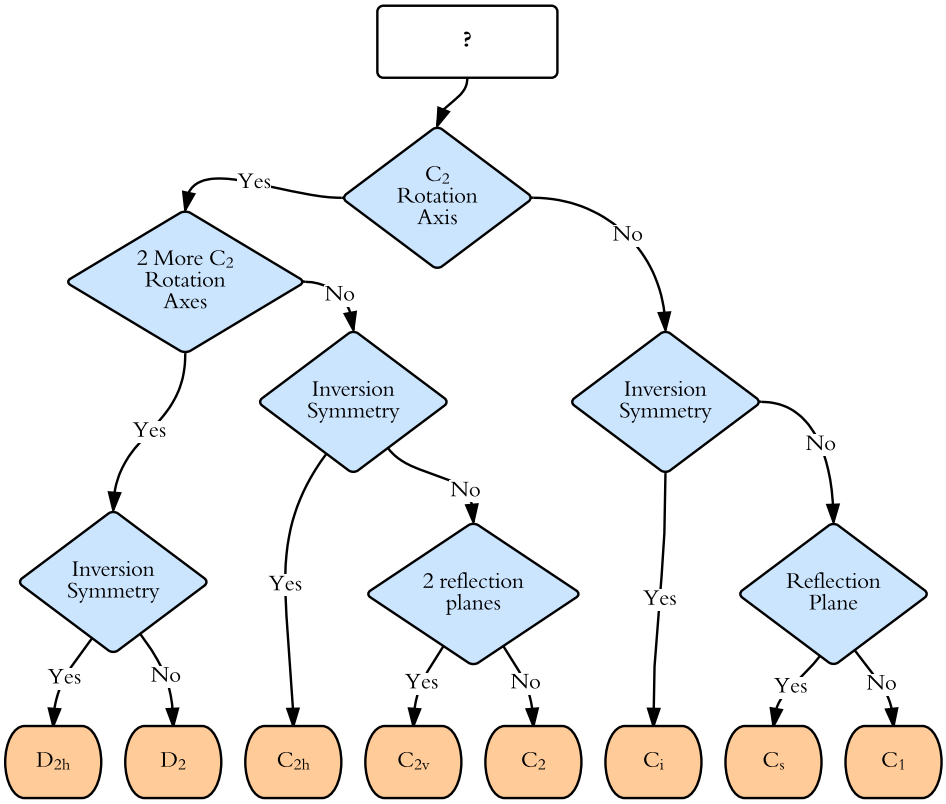

Figure 3.13: To determine the highest Abelian point group of a molecule, up to four fairly simple checks must be made.

a different X, the X points are each of the atomic centres, and the midpoints of each pair of alike atoms. Each one of these geometries is then tested to see if it has a C_2 rotation axis, and passed on to the next tests[1]. Each test creates new geometries, based on similar principals, with each geometry being passed to further tests down the line. After all of the tests, each geometry will have been assigned a particular symmetry (according to the tests it passed and failed), it is simply a matter of selecting the geometry with the highest symmetry, where the order is shown in the final row of fig. 3.13, from left to right.

Once the symmetry is determined, the non redundant atoms must be selected. This is fairly straightforward, and just requires iterating through the list of atoms, adding the atom to the list, and simultaneously removing all subsequent atoms which can be related to by any of the symmetry operations of the point group, or indeed any combination of them. Normally the *any combination of them* caveat could be problematic, as it could include infinitely long combinations, but since point groups have a finite size, and any product of any two group operations is also another group operation (both by merit of being a group), each operation only need be tested once.

These two pieces of information are then used to build a *skelton input* for Quantemol-N, which was altered to provide sensible defaults for a few other simple inputs.

3.1.7 Small Additional changes

Various other small changes, other than fixing bugs in the code, have also been made to Quantemol-N. The changes discussed here are all relatively small, simple changes which individually do not merit entire sections to themselves.

Disabling the long range multipoles

At one point there was interest in calculating cross sections for liquids. When the neighbouring molecules are close, the long range forces from neighboring molecules cancel each other out, and so a reasonably approximation for scattering from a liquid is simply to remove the long range forces. This was simply a matter of adding the

[1]The full set of tests, and some related code is included in appendix A and appendix C.

`ismax` variable to the `RSolve` namelist `RSLVIN`, which sets the maximum multipole to be used in the expansion of the asymptotic potentials in eq. (1.3.28).

Virtual Orbital count

Previously, Quantemol-N included 3 Virtual Orbitals for every calculation. While this normally suffices for smaller systems, for larger molecules, or systems with lower symmetry, it may not be sufficient. While this is especially true of SEP type calculations, as shown in Fujimoto et al. (2012), it is not as much an issue for SE or CASCI calculations. Despite this, the calculations are not always converged with just 3 virtual orbitals though, and so the ability to include more was added.

In the examples below, the point is to show that the calculations are not converged at the inclusion of just 3 virtual orbitals in all cases. As discussed previously, setting up large calculations to produce good results across a wide range of energies is time consuming - even when aided by Quantemol-N, and as such, the models used below are simple ones, chosen purely to demonstrate the need for the changes made. The work which prompted this addition (Fujimoto et al., 2012) provides an example of a full calculation having selected the number of virtual orbitals by analysing the convergence.

For small systems, e.g. H_2O, the calculation converges very quickly, the change from including additional virtual orbitals is negligible, as seen in fig. 3.14, though it can be seen a by examining the eigenphases (fig. 3.15), it clearly converges very quickly.

The same is not true when there are more non-redundant atomic centres off the centre of mass, so the problem can be exacerbated by choosing a larger molecule with low symmetry, for example propanol - $CH_3CH_2CH_2OH$. shown in figs. 3.16 and 3.17.

While the contribution from the long range dipole drowns out much of the difference coming from the lack of convergence, it is still clearly visible, and in the eigenphases even more obvious. This can be demonstrated even more distinctly in a system such as Pentane, see figs. 3.18 and 3.19; as there is no dipole to overwhelm the smaller contributions, the unconverged state of the calculation for low numbers of virtual orbitals is very clear.

Pentane was examined in C_{2v} symmetry, and has three symmetrically non-redundant

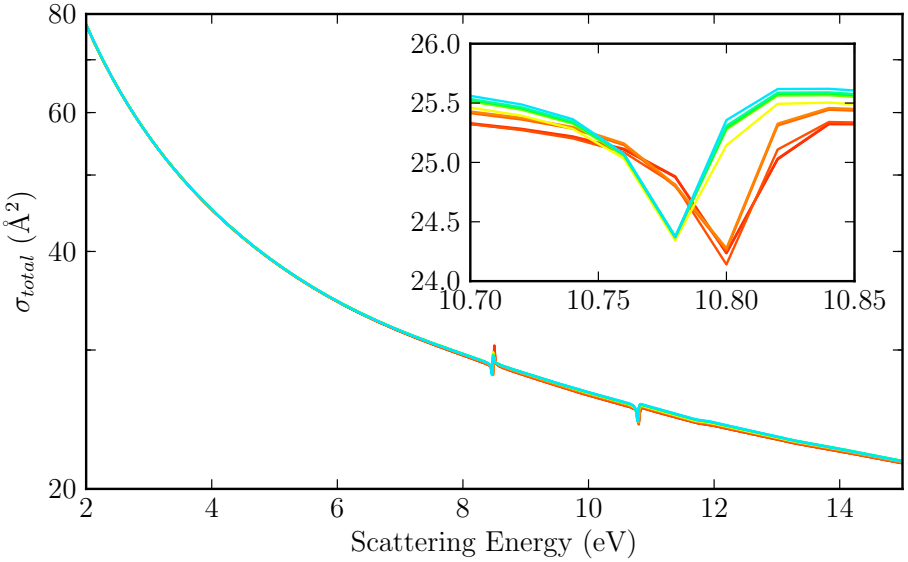

Figure 3.14: Water total cross section with the number of virtual orbitals varied. The line colours follow the gradient as the number of virtual orbitals varies from 1 to 30. Clearly the calculation has converged for just a single included virtual orbital. The resonances move only a little too. Overall, the effect is negligible, barely noticeable.

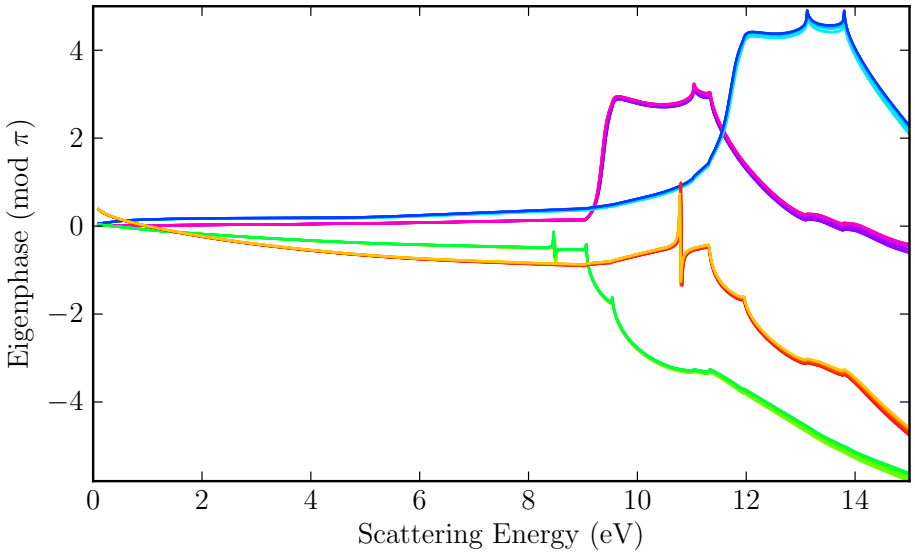

Figure 3.15: Water eigenphases with the number of virtual orbitals varied. The four sets of lines are the four symmetries of H_2O in C_{2v}, which each have colour ranges; A_1: ; B_1: ; B_2: ; and A_2: , again with the number of virtual orbitals increasing from 1 to 30. It is easier to see the difference here, but it is still very small.

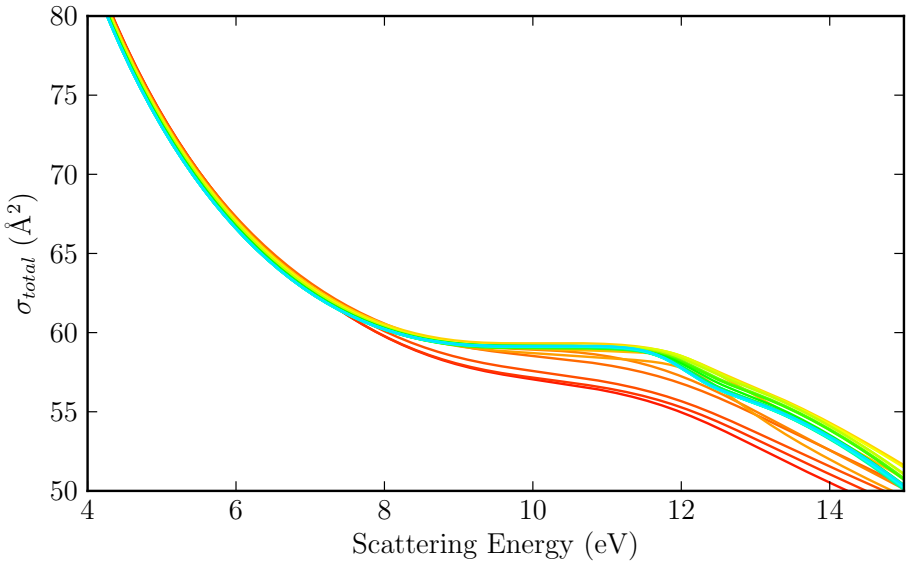

Figure 3.16: Propanol total cross section with the number of virtual orbitals varied. The line colours follow the gradient as the number of virtual orbitals varies from 1 to 30. Here there is clearly a change in the cross section as the number of included virtual orbitals changes, but at low energy it is dwarfed by the large dipole contribution.

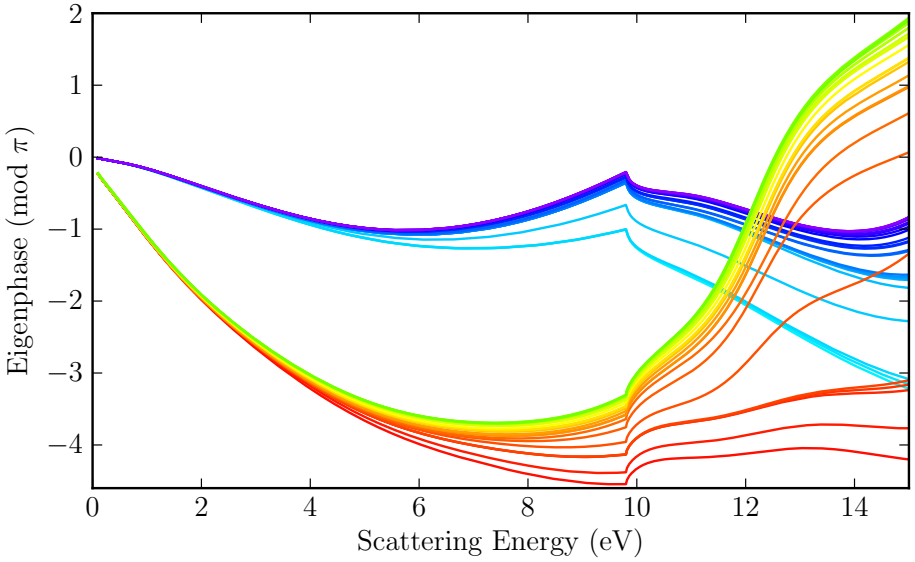

Figure 3.17: Propanol eigenphases with the number of virtual orbitals varied. The four sets of lines are the four symmetries of Propanol in C_s, which each have colour ranges; A′: ; A″: ; again with the number of virtual orbitals increasing from 1 to 30. The dependence of the eigenphases on the number of included virtual orbitals here is much more pronounced.

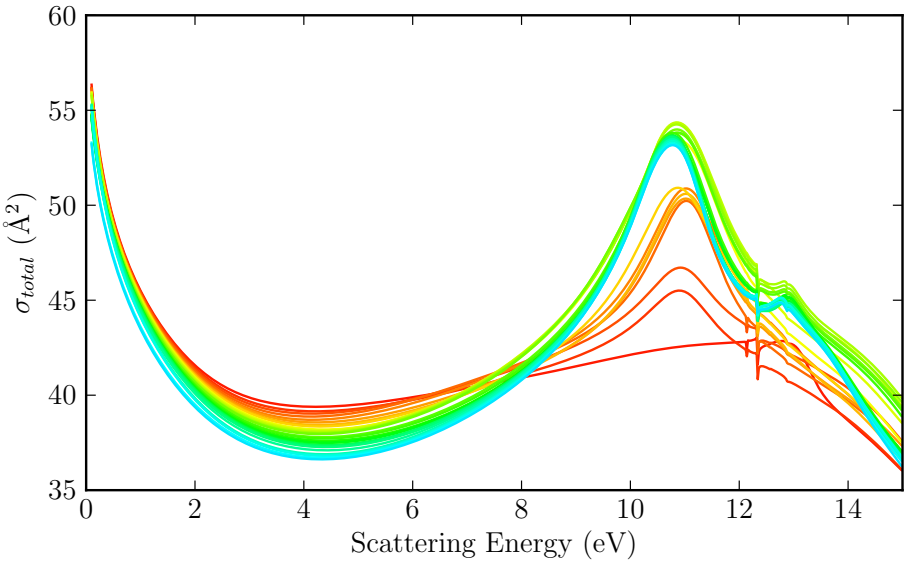

Figure 3.18: Pentane total cross section with the number of virtual orbitals varied. The line colours follow the gradient as the number of virtual orbitals varies from 1 to 30. The increased number of virtual orbitals needed for convergence here is clearly visible. The change in the height of the peak is only slightly more than seen in fig. 3.16 for propanol, but the lack of the dipole contribution makes it much more obvious.

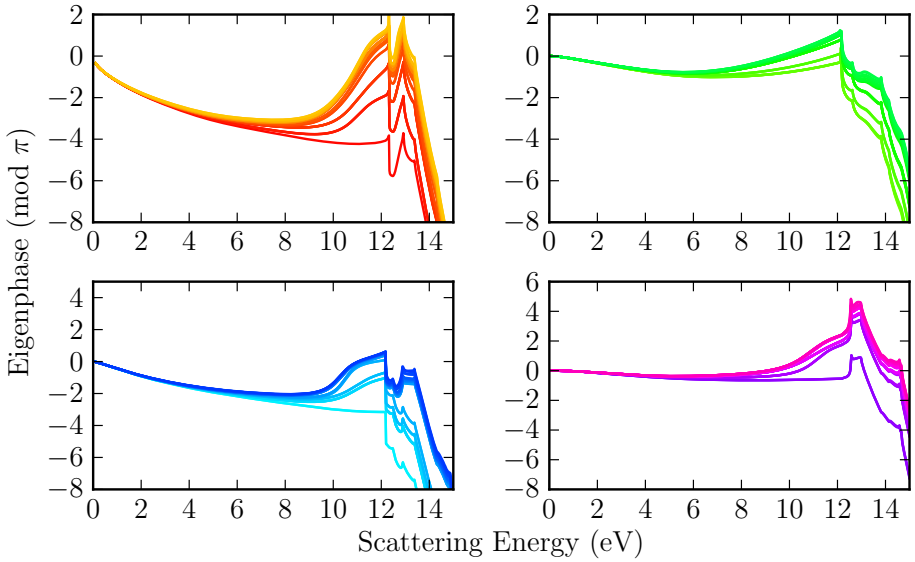

Figure 3.19: Pentane eigenphases with the number of virtual orbitals varied. The four sets of lines are the four symmetries of H_2O in C_{2v}, which each have colour ranges; A_1: ; B_1: ; B_2: ; and A_2: , again with the number of virtual orbitals increasing from 1 to 30. The rate of convergence with respect to the number of virtual orbitals is about the same as seen for propanol, in fig. 3.17.

carbon atoms, non of which are on the centre of mass, though one is close, and Propanol also has 3 symmetrically non-redundant carbon atoms, but also an additional oxygen atom, both have several hydrogen atoms, although these pose less of a issue in relation to convergence with respect to included virtual orbitals. So the two systems are not enormously dissimilar; and the there is little difference in convergence - it is simply less obvious for propanol due to the dipole.

It is also necessary to point out that there are a few further complications when it comes to deciding the number of virtual orbitals required. In the methane calculations discussed in the Methane chapter, page 53, no virtual orbitals are used at all. If the active space used is large, and contains many orbitals above the ground state, then the same orbitals which are being used as virtual orbitals in the scenarios discussed here are already included, they are just contained within the L^2 terms of eq. (1.3.12), rather than the continuum terms, χ, in eq. (1.3.11). All of these factors must be taken into account to create a balanced, and converged R-Matrix calculation.

Each calculation used the 6-311G basis set, with an active space including the first 3 HOMOs and first 3 LUMOs. The three molecules were examined over ranges from 1-30 virtual orbitals. All the models used an R-Matrix radius of 12 *a.u.*.

Open Orbitals in the Active Space

Again, this was a matter of adjusting the older *one default setting suits all* ideology to provide more flexibility to the user. Originally, Quantemol-N froze only a very small number of orbitals, meaning that as the size of the molecule increased, the number of configurations generated very quickly grew out of hand, which limited the possibility of using Quantemol-N for larger molecules.

To avoid ambiguity, the phrase “open orbitals” in this section refers solely to orbitals occupied in the ground state configuration. Increasing the number of open orbitals is functionally equivalent to decreasing the number of frozen core orbitals.

By altering this behaviour to increase the number of frozen orbitals, performing calculations for large molecules becomes much more feasible. Now, the program will scan through the orbitals, and on the first pass, open all orbitals within 15 eV of the

ground state. Orbitals are added in energy order - preserving degeneracy - until at least the number requested is reached, where the default is three. This means that all orbitals within 15eV of the ground state are always included, which has proven to be a more sensible default.

Comparing the nature of the convergence seen in fig. 3.21 to those seen when changing the number of virtual orbitals, figs. 3.17 and 3.19; it's clear that unlike with the number of virtual orbitals, the dependence of the eigenphases on the number of open orbitals is not continuous: the addition of orbitals to the CAS allows for more possible excitation channels. When these channels open, the eigenphases change qualitatively, which in turn leads to more drastic changes in the total cross section fig. 3.20.

As a result of the introduction of extra CSFs, and unlike increasing the number of included virtual orbitals, increasing the number of open orbitals can come at a substantial computation time cost, demonstrated in fig. 3.22, unlike when including more virtual orbitals.

OCS: Each calculation used the 6-311G basis set, with an active space including the first 3 HOMOs (except in the case of OCS, for which this varied from 1-8), and first 3 LUMOs. OCS included 3 virtual orbitals, and the other three molecules were examined over ranges from 1-30 virtual orbitals. All the models used an R-Matrix radius of 12 $a.u.$.

Generally speaking, increasing the number of open orbitals shifts features of the cross section to lower energy. This is not surprising, as it is essentially sliding the calculation towards (the usually infeasibly large) full CI model. When comparing the computational demand of fig. 3.22 and the total cross sections in fig. 3.20 it is evident that at some point a compromise must be made on with respect to the number of orbitals opened in the CAS; this kind of decision is common for parameters in R-Matrix calculations. Also note that certain numbers of open orbitals lack data points. This is because of degeneracy in the orbital energies, since the calculations were carried out in the $C_{\infty v}$ subgroup; C_{2v}.

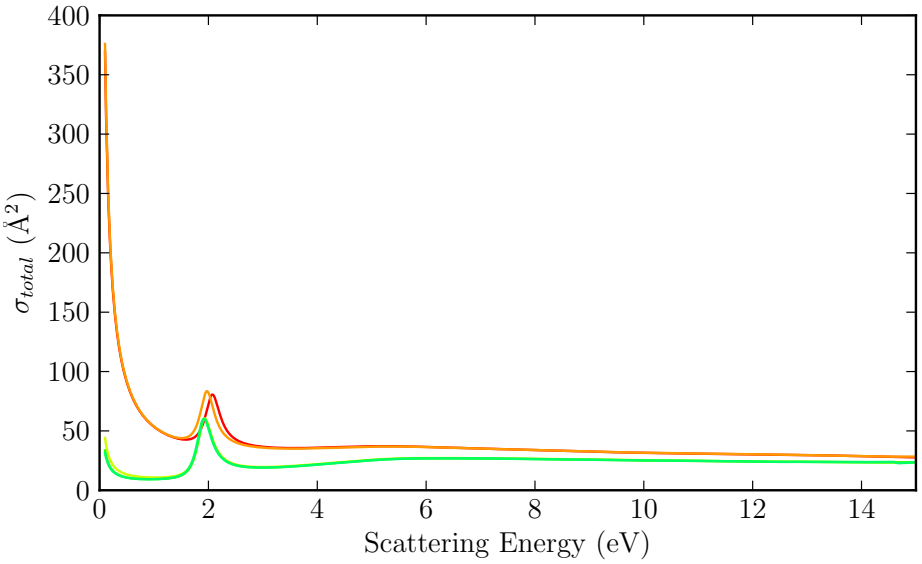

Figure 3.20: As more orbitals are included in the CAS, the energy of features in the cross sections are, generally speaking, reduced, because a more flexible active space allows a better representation of the target. The curves follow the colour gradient, as the number of open orbitals increases from 2 to 7..

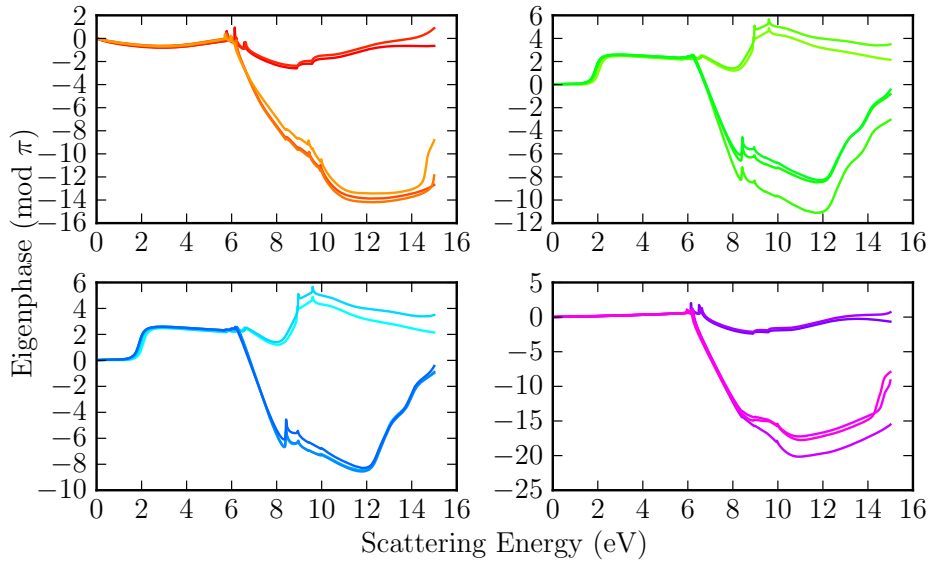

Figure 3.21: OCS eigenphases for varying numbers of open orbitals in the CAS. The four sets of lines are the four symmetries of OCS in C_{2v}, which each have colour ranges; A_1: ; B_1: ; B_2: ; and A_2: .

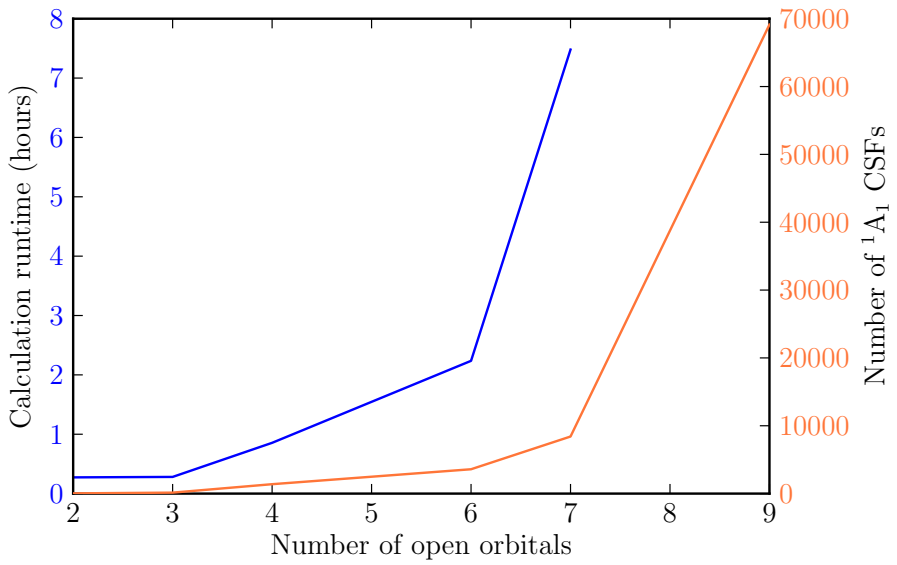

Figure 3.22: Calculation *size* and runtime (on an modern desktop machine, intel i7-3770 processor). The runtime is the ■ line, and the number of CSFs is in ■. The latter entries do not have run times because the calculations were not finished - primarily, because the time frames would have been outside of the scope of this example, but also, the model with 8 open orbitals required more than 16GB of ram, which was the limit of the work station, changing machines would not have made for a fair comparison of runtimes.

`MolPro` orbitals

Normally the orbitals used in Quantemol-N are produced by the Sweden Molecule code `SwSCF`. This routine sometimes struggles to converge, and when it does converge, the orbitals it creates are only simple HF orbitals. `MolPro` on the other hand is much more robust, and can be used to generate orbitals of considerably higher quality, for example state averaged natural orbitals, or CASSCF orbitals. By incorporating `MolPro` orbitals into Quantemol-N, using the `MPoutRd` routine, the quality of results produced is improved, and the range of molecules it is possible to run calculations for is increased.

Ground State Optimisation

Another small change to Quantemol-N was a change in the algorithm used to find the electronic configuration of the ground state. Previously, the code would use an initial guess for the ground state, and then select the lowest $^N/_2$ orbitals, and then repeat, until the configuration selected was the *ground state*. While in theory this is

perfectly adequate, in practice it neglected a two key issues with `SwSCF`. These issues are degenerate orbitals, and `SwSCF` failing, either to converge, or any other errors. If there were degenerate orbitals, this technique splits the symmetry of the molecule, and will give different cross sections for processes which, by symmetry, are identical.

The issue of `SwSCF` failing is not something which should need mentioning in any description of the process, it is just a side note. When `SwSCF` fails, then a different initial guess is selected, and the algorithm starts again. This simply made the algorithm more robust.

Table 3.1: Example of orbital energies or O_2. The D_{2h} columns give the degenerate orbitals of the Abelian D_{2h} subgroup of $D_{\infty h}$, with the $D_{\infty h}$ irreducible representation shown in the rightmost column.

Orbital Energy (eV)	D_{2h} Symmetry	$D_{\infty h}$ Symmetry
-562.50	a_g	σ_g
-562.48	b_{1u}	σ_u
-44.01	a_g	σ_g
-29.29	b_{1u}	σ_u
-19.23	a_g	σ_g
-18.52	b_{2u} b_{3u}	π_u
-15.07	b_{2g} b_{3g}	π_g
12.68	b_{1u}	σ_u
25.31	b_{2u} b_{3u}	π_u
26.96	b_{1u}	σ_u
...	...	...

The degeneracy issue is more important though. Because of the Abelian point group limitation of the UKRmol codes, any molecule being dealt with in a subgroup for it's true symmetry - for example any linear molecule - is liable to have degenerate orbital energies. This is only an issue if the *highest occupied molecular orbital* (HOMO)

is degenerate, and there are not enough electrons left to fill all the degenerate subgroup orbitals. For example, take the orbital energies described in table 3.1; these are the orbital energies of O_2, which has 16 electrons. The first 14 can be inserted into the first 7 orbitals, but then the next two must be split, with one going to each of the b_{2u} and b_{3u} orbitals, producing the well documented oxygen triplet, with a ground state of $1\sigma_g^2, 1\sigma_u^2, 2\sigma_g^2, 2\sigma_u^2, 3\sigma_g^2, 1\pi_u^4, 2\pi_g^2$. The original algorithm did not take degeneracy into account, and so both electrons would have been placed into whichever orbital happened to appear first in the `SwSCF` output.

State Selection

Every possible configuration of electrons within an active space results in a state which can be included in the calculation. For large active spaces, the number of states can become very large. From figs. 2.4 to 2.8 it is easy to see that including every state in calculations would be wasteful, but at the same time a certain number do have to be included to accurately model the energy region of interest.

The original method of including states was to request a number of states per symmetry, and then an energy cut off is supplied, such that in the outer region all states above this are removed. Since the states are not distributed evenly across the symmetries, this could lead to certain symmetries being represented relatively more or less than others.

This has been updated: once again an energy cut off is supplied, but now all states up to this energy are included, allowing for consistent models to be created easily, and making comparisons between varied models easier to construct. There is still an option to request a particular number of states, but it has be altered so that it is the total number of states, fixing the inconsistent treatment of different symmetries. Supplying both will use the larger number in the inner region, and the smaller as a cut off in the outer region, where a large number of states can be computationally expensive. Excluding states in the outer region causes pseudo resonances at the energies all channels involving the excluded states open - if these thresholds are above the energy region of interest, then excluding them has no effect on the results, while decreasing

the runtime (in some cases significantly).

3.2 QN consulting use

3.2.1 InI

As mentioned in section 1.3, lighting is one of the many areas of active research in the field of plasmas. A specific type of light is a *High Intensity Discharge* (HID) lamp, where an electric arc passes through a tube filled with gas, and metal salts. The gas eases the initial arc, which then heats up, evaporating the metal salts forming a plamsa. This plasma both emits considerably more light than the arc, and also increases the efficiency of the discharge. There are several subtypes of HID lamps, in this case we are considering a *metal-halide* lamp.

A metal-halide lamp contains a mixture of mercury vapour and metal-halide salts. The addition of the metal-halides serves to increase the luminous efficacy, and improve the *colour rendition*[1] of the lamp. The additive investigated here is InI_3, which improves the colour rendition while decreasing the efficiency, but not as much as other additives, such as LiI and ThI_4 (Bencze et al., 1993).

Professor Mark Kushner, the director of the Department of Electrical and Computer Engineering at the University of Michigan, and a member of the Quantemol Advisory Board requested electron scattering cross sections for InI, for use in the *Hybrid Plasma Equipment Model* (HPEM). When creating a chemistry for a plasma model, cross sections are required for all reactions included in the model, and these often include radicals and other short lived species - for which there are often a very limited quantity of results in the literature. This is covered nicely by Cukras et al. (2013); quoted at the beginning of chapter 3.

This is one of the main selling points of Quantemol-N, allowing gaps in chemistry data sets to be filled. InI electron scattering cross sections are provided to augment data available in the literature for other In_xI_y species.

[1] A quantitative measure of a light source's ability to reproduce colours accurately, as a natural light source would, where a black body source obtains a perfect score.

Of the relatively little amount of data on this molecule, one properties for which there were comparisons available in the literature is the dipole moment, where that obtained in Quantemol-N was 3.412D, compared to 3.489D and 3.33D of Banerjee and Das (2011) and Zou et al. (2003), respectively.

This calculation also made use of the dissociative attachment estimator, as implemented in Quatnemol-N, fully explained in Munro et al. (2012). This option requires two additional inputs: the vibrational frequency, 177 cm^{-1}, and the dissociation energy, 3.296 eV, both taken from Girivheva et al. (1989). The dissociative attachment cross section produced is shown in fig. 3.23, where the contributions from three resonance features are clearly visible.

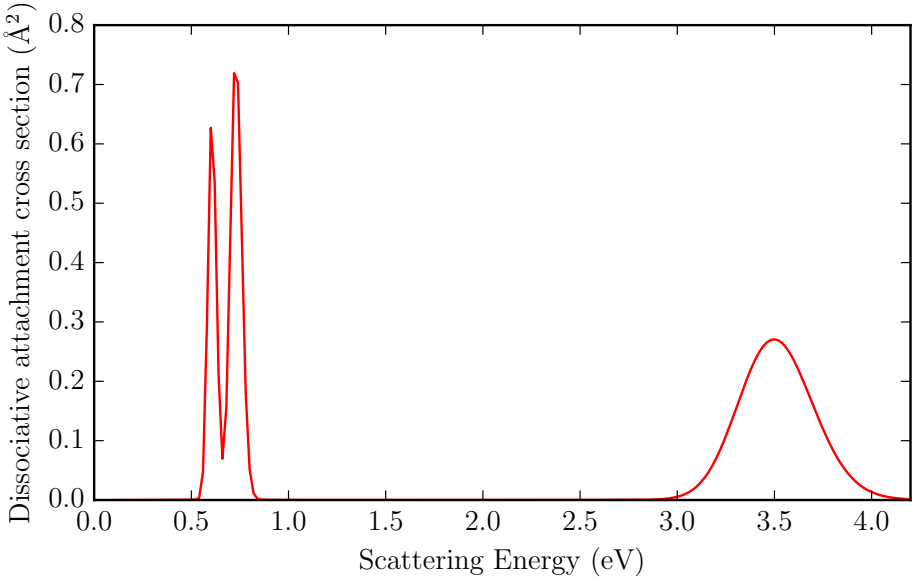

Figure 3.23: InI estimated dissociative attachment cross section

The cross sections in figs. 3.24 and 3.25 come from different programs - the former from the `UKRmol` suite, and the latter from `polyDCS` - which is the source of the qualitative differences is the curves (i.e. the close coupling curve from `polyDCS`). When the differential cross sections are integrated though (and any artefacts ignored) the same total cross section is recovered. It is also worth noting that the close coupling contributions in each of the two plots are just that - they are the isolated contribution

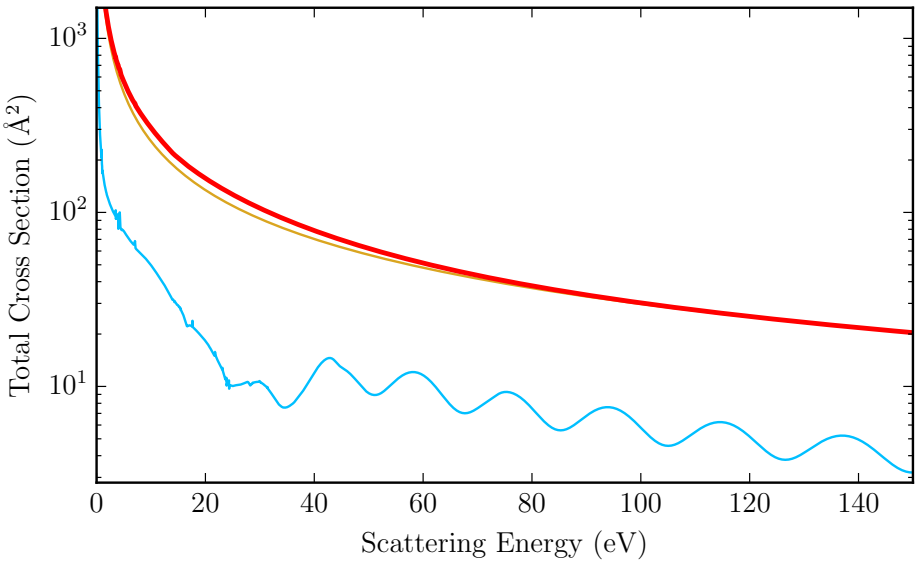

Figure 3.24: Total cross section for InI. Total cross section matched to Born cross section above 15 eV, ■; Born cross section, ■; Close coupling contribution, ■.

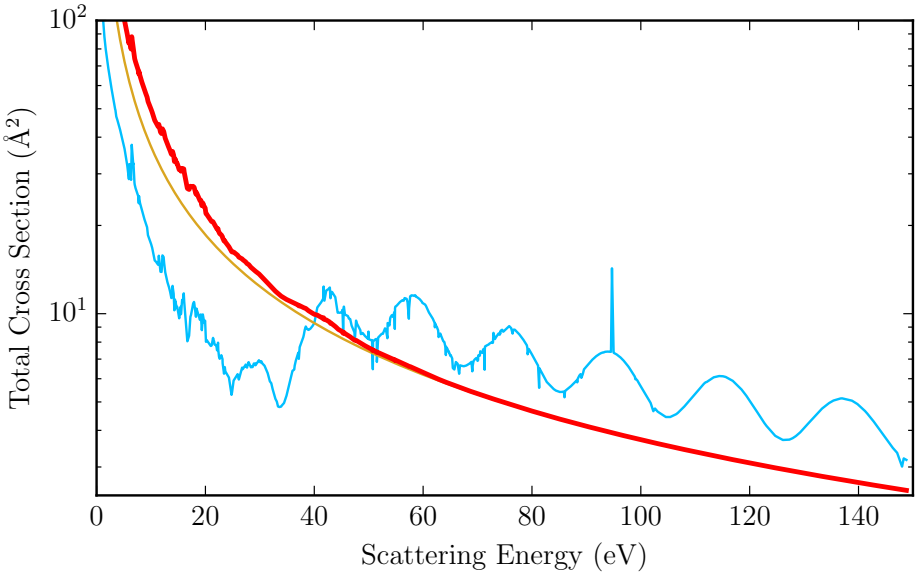

Figure 3.25: InI momentum transfer cross section. Total cross section matched to Born cross section above 15 eV, ■; Born cross section, ■; Close coupling contribution, ■. The close-coupling contribution is small at low energy, and so the Born cross section line is difficult to see - it lies almost exactly underneath the matched cross section line.

to the cross sections arising from close coupling. In each plot, the total cross sections are the sums of the born cross sections and close coupling contributions.

The close coupling contributions in the same two figures (figs. 3.24 and 3.25) become oscillatory above 25eV. This is not something that any information can be gleaned from - states were only included in the calculation up to 25eV, so any close coupling cross sections above this are meaningless artefacts. The statement here is that we cannot infer cross sections from any energy after we have neglected to include a state, since we are now missing terms from the calculations. This is a simplification though - careful considerations of the distribution of the included states, and the manner in which they span the R-matrix box can allow cross sections to be calculated in regions where not all states are accounted for: an in-depth explanation of this can be found in Gorfinkiel and Tennyson (2005).

4

Conclusions

4.1 Methane

It is difficult to develop a completely *ab initio* theoretical model for low-energy electron collisions with methane which recovers all the key properties of the system, such as the Ramsauer-Townsend minimum and the electronic excitation energy of low-lying, diffuse excited states. Here, a number of possible collision models were tested, and find that the best results are obtained using a target representation which involves use of a complete active space for the valence electron and excitations of up to two electrons from this valence space into an extended set of virtual orbitals. By analogy with quantum chemical electronic structure calculations, we call this a multireference configuration interaction (MRCI) model. This model gives a good representation of the RT minimum. It also appears to give a good fixed-nuclei treatment of the electron-impact dissociation problem, although a full study of this would require considering both a better treatment of the excited Rydberg states and of nuclear motion.

The MRCI model represents a move beyond either the use of a complete active space target of or the standard R-matrix with pseudo states representation, although it has some similarities with the latter approach. Whether it works equally well for low-energy electron collisions with other molecules will be a matter for further study. However it is clear that use of the MRCI model is computationally demanding and its

application to electron collisions with targets with many active electrons will require further algorithmic developments to make the method generally tractable.

The use of *better* molecular orbitals may also go some way to improving these calculations, as a parallel route to the examination of the configuration space used, as defined by the model. Combining the two approaches is perhaps the best route forwards.

The results presented here come from a single model, able to reproduce results for many processes simultaneously, producing results for processes where no experimental ones exist, validated (somewhat) by the processes where they do. As a result of this, perhaps unsurprisingly, they do not produce the *best* results for all of these processes - that is, the best agreement with experiment, when compared to other theoretical treatments, however agreement where comparisons do exist lend credence to results where comparisons (and hence additional validation) are not available. For these exact reasons our rotational excitation cross sections were selected as the recommend results published in Song et al. (2015), while the other cross sections are mentioned as agreeing with the other results present already. All of the methane results presented in this thesis were also published in Brigg et al. (2014), attached in appendix D.

There are a few directions the work here could be taken further. A trivial way to improve the results here is simply to increase the various model parameters describing the active space. The numbers chosen in this thesis were selected on a cost versus reward basis, taking into account the number of states generated and the energies of the states (see, for example, figs. 2.5 to 2.7). While these numbers won't change, the computers they run on do. Simply increasing the model size will gain better results, in the same amount of time through both the simple improvement in processing power of computers, and enhancements to the code, such as the parallelization of the outer region of the codes (Sunderland et al., 2002, 2009; Burke et al., 2002).

And then there is also a more complex improvement; we treat the electronic states comprehensively, but we are still in the fixed-nuclei approximation, such that any excited states are not necessarily in their equilibrium geometries, resulting in incorrect (i.e. approximate) energies. Including a consideration for nuclear motion after excita-

tion would eb a welcome addition to the model, as well as some treatment of nuclear motion with respect to electron impact dissociation, as in Ziółlkowski et al. (2012), would improve the cross sections for this process - including this can be expected to increase the cross sections (Stibbe and Tennyson, 1998).

We also have ways in which the underlying UK **R**-matrix codes can be improved - with two examples having been developed since the completion of this work. The first is being another improvement in the `SCATCI` code, and being another example of a pure performance increase: the work of Al-Refaie and Tennyson takes advantage of modern computer architectures to construct the Hamiltonians in parallel, yielding significant performance gains, which not only reduces computation time, but allows larger systems to become numerically feasible.

The second is in the so called UKRmol+ suite, which adds the ability to define basis functions using B-splines, enabling much larger **R**-matrix spheres (up to 35 Bohr, as opposed to the $\tilde{1}5$ Bohr limit of the UKRmol codes) to be utilized. This opens the doors to calculations on systems exhibiting more diffuse electronic states; a first demonstration of these new codes is provided in Darby-Lewis et al. (2017) with a study of BeH, providing a significant improvement over previous results.

4.2 CASE / Quantemol

The work contributing to this thesis has been done as part of a collaboration with the Quantemol company, as part of a CASE studentship, with the aim of being mutually beneficial. Obviously work done on behalf of the company is beneficial to them, as well as the advances made to the various pieces of software. For me, the experience has been extremely beneficial, for a combination of reasons: primarily, using Quantemol-N to either outright run calculations, or as a springboard, enabling the input files to be quickly created is a huge productivity boost - the time investment in setting up a calculation is reduced from several days - where if the user is not experienced in running the UKRMol codes, then this will likely be a considerable underestimate - to several minutes. Secondly, writing software to automate the decisions that would normally be made according to some experience based thought process encourages one to really

understand how the programs work, and demands that this understanding is there in order to make the program robust - this was an invaluable learning experience.

The continued development of Quantemol-N is something that I believe will help the theoretical electron-scattering community grow, as well as those in industry searching for difficult to obtain scattering cross sections. It is also an invaluable tool for students looking for a leg up in the realm of the UKRmol suite.

The additions provided in this thesis serve to further this ease of use, with each of the new modules requiring only a single option be checked to include the extra results - all required input can be found in the outputs of the previous routines, for example the updating of the ground state optimisation, removing this as a required input, and the `QN Express` software removes the need to input the molecule's geometry by either fetching it from the NIST database, or minimising the geometry from an initial guess using MolPro. Along with the previous functionality, these reduce the entry curve of **R**-matrix calculations even more, giving it a far more manageable gradient and significantly increasing the number of potential active users. Two examples of this are the N_2 and CH_4 photoionization cross sections produced using the software and published in Brigg et al. (2015), where the only additional option needed over a normal calculation is that the *photoionization* option is checked, everything else is taken care of automatically.

On the topic of future development, there are a few branches: the first is the removal of user input - more automisation, as demonstrated by the `QN Express` software. Going down the *less is more* path, the model could be picked simply by a convergence threshold, with the program running until a satisfactory level of convergence is arrived at. An alternate route is to provide tests of this convergence simply as an option - after a calculation, we can probe the nearby parameter space since a well converged model should have small sensitivities to its parameters. The third branch is simply adding additional features as they are requested by customers, or become useful for in house use (as was the case for many of the improvements in the Software Changes section, p. 86).

A specific improvement which would be useful would be the ability to select different

types of model; currently the choices are full CI, or static exchange - all or nothing, being able to select a model somewhere between the two would be very useful, for example adding RMPS or the MRCI models would be very beneficial, since the correct creation of inputs for these models is far from trivial, and prone to error - errors which are difficult to detect. This is exactly the area Quantemol-N was designed to improve, and so definitely should hold a significant proportion of the direction it continues to move in.

4.3 Summary

In this thesis, I have provided a thorough investigation of excited electronic states of methane using the UKRMol codes, landing on a *Multi Reference Configuration Interaction* model to provide multiple properties and cross sections simultaneously, while still remaining computationally tractable, with a subset of the produced results being selected as the recommended data set in a comprehensive overview of electron-methane scattering results (Song et al., 2015). The model can of course be replicated for other species.

I have also contributed several additions to the Quantmol-N software as part of a CASE studentship, where the software is provided to academic institutions to aid in the uptake of the UKRMol codes, as well as to industry to further research requiring the created cross sections. The software greatly decreases the learning curve and subsequent calculation setup time, increasing user productivity. The additions I contributed lie in two distinct camps; the first being additions of features in the UKRMol codes which had not yet filtered through into Quantemol-N, and the second being further reducing the user time cost involved in setup, automating several steps. Quantemol-N is an invaluable tool to those who do not already have the required expertise to benefit from the UKRMol suite, nor the time required to acquire said expertise, and while two two pieces of software continue to grow, the benefits will continue to grow too.

A

$b_{\ell m}$ Coefficients

The $b_{\ell m}$ coefficients are an important input to `polyDCS`, as discussed in section 3.1.2. They are tabulated here, for $\ell \leqslant 4$, and rules are provided for higher ℓ.

The $b_{\ell m}$ coefficients for Abelian point groups are either 0 or 1. While `polyDCS` is not limited to abelian point groups, the UKRmol codes are; and so they are all that is considered below. A truncated example of a `polyDCS` $b_{\ell m}$ input is shown here:

C2v.blm

```
A1                          9
          0          1
   0    1.0000000000
          1          1
   0    1.0000000000
          2          1
   0    1.0000000000
          2          1
   2    1.0000000000
          3          1
   0    1.0000000000
          3          1
   2    1.0000000000
          4          1
   0    1.0000000000
          4          1
   2    1.0000000000
          4          1
   4    1.0000000000
B1                          6
          1          1
   1    1.0000000000
          2          1
   1    1.0000000000
          3          1
   1    1.0000000000
          3          1
   3    1.0000000000
          4          1
   1    1.0000000000
```

Table A.1: D_{2h} $b_{\ell m}$ coefficients for $\ell \leqslant 4$.

ℓ	A_g	B_{1g}	B_{2g}	B_{3g}	A_u	B_{1u}	B_{2u}	B_{3u}
0	0							
1						0	-1	1
2	0, 2	-2	1	-1				
3					-2	0, 2	-3, -1	1, 3
4	0, 2, 4	-4, -2	1, 3	-3, -1				

Table A.2: D_2 $b_{\ell m}$ coefficients for $\ell \leqslant 4$.

ℓ	A	B_1	B_2	B_3
0	0			
1		0	-1	1
2	0, 2	-2	1	-1
3	-2	0, 2	-3, -1	1, 3
4	0, 2, 4	-4, -2	1, 3	-3, -1

While the input example is truncated, the format is simple and easy to extrapolate for the remaining symmetries. The file is divided into blocks: one for each symmetry; with each block then further divided into a header line, containing a name for the IR, and the number of groups of $b_{\ell m}$ coefficients. The remainder of the block, two lines at a time, give the $b_{\ell m}$ coefficients. For each pair of lines, the first number is ℓ, and the second the number of m values (in the format chosen here, it is always 1 coefficient at a time). The second line of each pair contains first m, and then $b_{\ell m}$. Since the coefficients are always 1 for the Abelian groups, it is easy to tabulate them such that the pattern is obvious. In tables A.1 to A.8 the values are the m coefficients for which the coefficients exist (that is, are 1, and not zero).

Table A.3: C_{2h} $b_{\ell m}$ coefficients for $\ell \leqslant 4$.

ℓ	A_g	B_g	A_u	B_g
0	0			
1			0	-1, 1
2	-2, 0, 2	-1, 1		
3			-2, 0, 2	-3, -1, 1, 3
4	-4, -2, 0, 2, 4	-3, -1, 1, 3		

Table A.4: C_{2v} $b_{\ell m}$ coefficients for $\ell \leqslant 4$.

ℓ	A_1	B_1	B_2	A_2
0	0			
1	0	1	-1	
2	0, 2	1	-1	-2
3	0, 2,	1, 3	-3, -1	-2
4	0, 2, 4	1, 3	-3, -1	-4, -2

Table A.5: C_2 $b_{\ell m}$ coefficients for $\ell \leqslant 4$.

ℓ	A	B
0	0	
1	0	-1, 1
2	-2, 0, 2	-1, 1
3	-2, 0, 2	-3, -1, 1, 3
4	-4, -2, 0, 2, 4	-3, -1, 1, 3

Table A.6: C_s $b_{\ell m}$ coefficients for $\ell \leqslant 4$.

ℓ	A′	B″
0	0	
1	-1, 1	0
2	-2, 0, 2	-1, 1
3	-3, -1, 1, 3	-2, 0, 2
4	-4, -2, 0, 2, 4	-3, -1, 1, 3

Table A.7: C_i $b_{\ell m}$ coefficients for $\ell \leqslant 4$.

ℓ	A_g	A_u
0	0	
1		-1, 0, 1
2	-2, -1, 0, 1, 2	
3		-3, -2, -1, 0, 1, 2, 3
4	-4, -3, -2, -1, 0, 1, 2, 3, 4	

Table A.8: C_1 $b_{\ell m}$ coefficients for $\ell \leqslant 4$.

ℓ	A
0	0
1	-1, 0, 1
2	-2, -1, 0, 1, 2
3	-3, -2, -1, 0, 1, 2, 3
4	-4, -3, -2, -1, 0, 1, 2, 3, 4

Table A.9: Descent correlation tables for Abelian groups. This table allows comparisons between different symmetries. Irreducible representations of the same symmetry are in the same rows in the table - where an IR represents functions of multiple symmetries is appears in multiple rows.

D_{2h}	D_2	C_{2v}	C_{2h}	C_2	C_s	C_i	C_1
A_g	A	A_1	A_g	A	A'	A_g	A
B_{1g}	B_1	A_2	A_g	A	A'	A_g	A
B_{2g}	B_2	B_1	B_g	B	A''	A_g	A
B_{3g}	B_3	B_2	B_g	B	A''	A_g	A
A_u	A	A_2	A_u	A	A''	A_u	A
B_{1u}	B_1	A_1	A_u	A	A''	A_u	A
B_{2u}	B_2	B_2	B_u	B	A'	A_u	A
B_{3u}	B_3	B_1	B_u	B	A'	A_u	A

Table A.10: Rules to create $b_{\ell m}$ coefficients for Abelian point groups.

	m even		m odd	
	$m < 0$	$0 \leqslant m$	$m < 0$	$0 < m$
ℓ even	B_{1g}	A_g	B_{3g}	B_{2g}
ℓ odd	A_u	B_{1u}	B_{2u}	B_{3u}

Higher ℓ

All of the Abelian groups are subgroups of D_{2h}, and so by defining rules to give the $b_{\ell m}$ coefficients for D_{2h}, the descent correlation rules can be used to give the coefficients for all of its subgroups - that is, all of the Abelian groups. The descent correlation rules give the relationship of one point group to another, and are detailed in table A.9.

There are several ways of describing the process which gives the $b_{\ell m}$ values, one way would be to give a table with the rules for each symmetry, but it turns out that many of the rules are redundant, and so can be simplified, shown in table A.10. To get the coefficients for a lower symmetry, simply take the rules for each of the corresponding symmetries in D_{2h}, and combine them; for example, to work out which coefficients are non-zero for A_g of C_{2h}, look down the C_{2h} column in table A.9, and then take the corresponding D_{2h} symmetry each time A_g is seen - in this case, A_g and B_{1g}. Then, looking at table A.10, the rules for these two IRs are ℓ even, m even, and either $m < 0$ or $m \geqslant 0$; when combined, this just says that the $b_{\ell m}$ for C_{2h} A_g are one when m and ℓ are even, and zero otherwise. Checking back with table A.3, this logic agrees.

B

Spherical Harmonics

The real (or *tesseral*) spherical harmonics were used to determine the $b_{\ell m}$ coefficients used in `PolyDCS`. They are included here, along with he corresponding irreducible representations for each of the Abelian point groups. The coefficients provided to `PolyDCS` tell it which of the real spherical harmonics are accounted for by each IR.

Table B.1: Real spherical harmonics (using the Condon-Shortley phase convention) and the corresponding m_ℓ, values, split by ℓ values, mapped to the corresponding irreducible representations of the Abelian point groups. In the plots, orange and blue represent positive and negative lobes, respectively. The axis orientations are kept consistent for all plots, with the x, y, and z axes being those shown by the p_x, p_y, and p_z harmonics' plots.

Cubic Harmonic	m_ℓ	Irreducible Representation						
		D_{2h}	D_2	C_{2h}	C_{2v}	C_2	C_s	C_i	C_1
$\ell = 0$									
$s = Y_0^0 = \frac{1}{\sqrt{4\pi}}$ 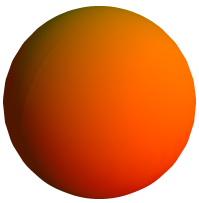	0	A_g	A	A_g	A_1	A	A′	A_g	A
$\ell = 1$									
$p_x = \frac{1}{\sqrt{2}}(Y_1^{-1} - Y_1^1) = \sqrt{\frac{3}{4\pi}} \cdot \frac{x}{r}$ 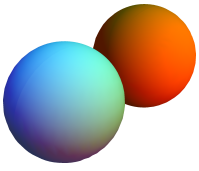	1	B_{3u}	B_3	B_u	B_1	B	A′	A_u	A

Continued on next page

Cubic Harmonic		m_ℓ	Irreducible Representation						
			D_{2h}	D_2	C_{2h}	C_{2v}	C_2	C_s	C_i	C_1
$p_z = Y_1^0 = \sqrt{\frac{3}{4\pi}} \cdot \frac{z}{r}$		0	B_{1u}	B_1	A_u	A_1	A	A″	A_u	A
$p_y = \frac{i}{\sqrt{2}}(Y_1^{-1} + Y_1^1) = \sqrt{\frac{3}{4\pi}} \cdot \frac{y}{r}$	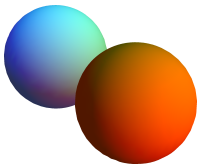	-1	B_{2u}	B_2	B_u	B_2	B	A′	A_u	A
$\ell = 2$										
$d_{x^2-y^2} = \frac{1}{\sqrt{2}}(Y_2^{-2} + Y_2^2) = \frac{1}{4}\sqrt{\frac{15}{\pi}} \cdot \frac{x^2-y^2}{r^2}$	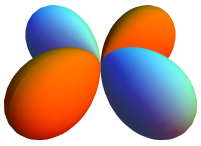	2	A_g	A	A_g	A_1	A	A′	A_g	A
$d_{xz} = \frac{1}{\sqrt{2}}(Y_2^{-1} - Y_2^1) = \frac{1}{2}\sqrt{\frac{15}{\pi}} \cdot \frac{xz}{r^2}$	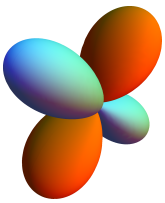	1	B_{2g}	B_2	B_g	B_1	B	A″	A_g	A
$d_{z^2} = Y_2^0 = \frac{1}{4}\sqrt{\frac{5}{\pi}} \cdot \frac{2z^2-x^2-y^2}{r^2}$	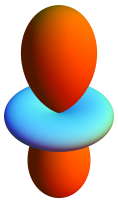	0	A_g	A	A_g	A_1	A	A′	A_g	A
$d_{yz} = \frac{i}{\sqrt{2}}(Y_2^{-1} + Y_2^1) = \frac{1}{2}\sqrt{\frac{15}{\pi}} \cdot \frac{yz}{r^2}$	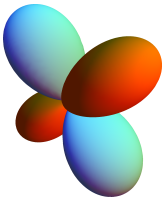	-1	B_{3g}	B_3	B_g	B_2	B	A″	A_g	A
$d_{xy} = \frac{i}{\sqrt{2}}(Y_2^{-2} - Y_2^2) = \frac{1}{2}\sqrt{\frac{15}{\pi}} \cdot \frac{xy}{r^2}$	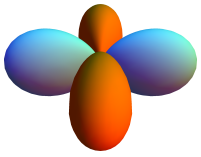	-2	B_{1g}	B_1	A_g	A_2	A	A′	A_g	A
$\ell = 3$										

Continued on next page

Cubic Harmonic		m_ℓ	Irreducible Representation						
			D_{2h}	D_2	C_{2h}	C_{2v}	C_2	C_s	C_i	C_1
$f_{x(x^2-3y^2)} = \frac{1}{\sqrt{2}}(Y_3^{-3} - Y_3^3) = \frac{1}{4}\sqrt{\frac{35}{2\pi}} \cdot \frac{x(x^2-3y^2)}{r^3}$	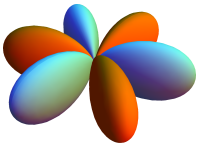	3	B_{3u}	B_3	B_u	B_1	B	A′	A_u	A
$f_{z(x^2-y^2)} = \frac{1}{\sqrt{2}}(Y_3^{-2} + Y_3^2) = \frac{1}{4}\sqrt{\frac{105}{\pi}} \cdot \frac{z(x^2-y^2)}{r^3}$	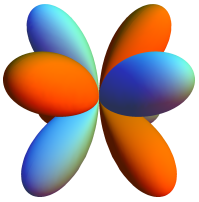	2	B_{1u}	B_1	A_u	A_1	A	A″	A_u	A
$f_{xz^2} = \frac{1}{\sqrt{2}}(Y_3^{-1} - Y_3^1) = \frac{1}{4}\sqrt{\frac{21}{2\pi}} \cdot \frac{x(4z^2-x^2-y^2)}{r^3}$	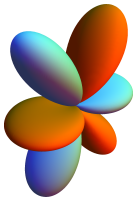	1	B_{3u}	B_3	B_u	B_1	B	A′	A_u	A
$f_{z^3} = Y_3^0 = \frac{1}{4}\sqrt{\frac{7}{\pi}} \cdot \frac{z(2z^2-3x^2-3y^2)}{r^3}$	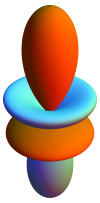	0	B_{1u}	B_1	A_u	A_1	A	A″	A_u	A
$f_{yz^2} = \frac{i}{\sqrt{2}}(Y_3^{-1} + Y_3^1) = \frac{1}{4}\sqrt{\frac{21}{2\pi}} \cdot \frac{y(4z^2-x^2-y^2)}{r^3}$	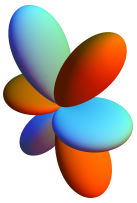	-1	B_{2u}	B_2	B_u	B_2	B	A′	A_u	A
$f_{xyz} = \frac{i}{\sqrt{2}}(Y_3^{-2} - Y_3^2) = \frac{1}{4}\sqrt{\frac{105}{\pi}} \cdot \frac{xyz}{r^3}$	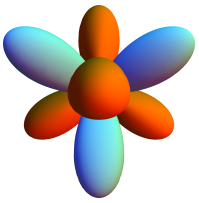	-2	A_u	A	A_u	A_2	A	A″	A_u	A
$f_{y(3x^2-y^2)} = \frac{i}{\sqrt{2}}(Y_3^{-3} + Y_3^3) = \frac{1}{4}\sqrt{\frac{35}{2\pi}} \cdot \frac{y(3x^2-y^2)}{r^3}$	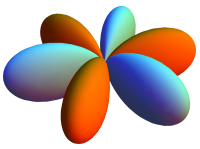	-3	B_{2u}	B_2	B_u	B_2	B	A′	A_u	A

$\ell = 4$

Continued on next page

Cubic Harmonic		m_ℓ	Irreducible Representation							
			D_{2h}	D_2	C_{2h}	C_{2v}	C_2	C_s	C_i	C_1
$g_{x^4+y^4} = \frac{1}{\sqrt{2}}(Y_4^{-4} + Y_4^4) = \frac{3}{16}\sqrt{\frac{35}{\pi}} \cdot \frac{x^2(x^2-3y^2)-y^2(3x^2-y^2)}{r^4}$	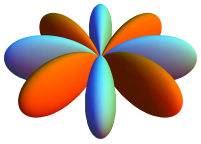	4	A_g	A	A_g	A_1	A	A′	A_g	A
$g_{x^3z} = \frac{1}{\sqrt{2}}(Y_4^{-3} - Y_4^3) = \frac{3}{4}\sqrt{\frac{35}{2\pi}} \cdot \frac{xz\cdot(x^2-3y^2)}{r^4}$	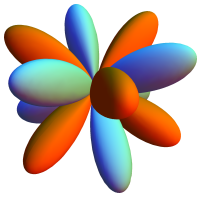	3	B_{2g}	B_2	B_g	B_1	B	A″	A_g	A
$g_{(x^2-y^2)z^2} = \frac{1}{\sqrt{2}}(Y_4^{-2} + Y_4^2) = \frac{3}{8}\sqrt{\frac{5}{2\pi}} \cdot \frac{(x^2-y^2)\cdot(7z^2-r^2)}{r^4}$	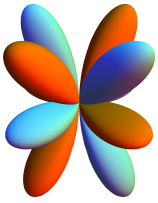	2	A_g	A	A_g	A_1	A	A′	A_g	A
$g_{xz^3} = \frac{1}{\sqrt{2}}(Y_4^{-1} - Y_4^1) = \frac{3}{4}\sqrt{\frac{5}{2\pi}} \cdot \frac{xz\cdot(yz^2-3r^2}{r^4}$	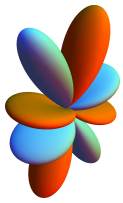	1	B_{2g}	B_2	B_g	B_1	B	A″	A_g	A
$g_{z^4} = Y_4^0 = \frac{1}{4}\sqrt{\frac{35}{2\pi}} \cdot \frac{}{r^4}$	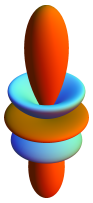	0	A_g	A	A_g	A_1	A	A′	A_g	A
$g_{yz^3} = \frac{i}{\sqrt{2}}(Y_4^{-1} + Y_4^1) = \frac{3}{4}\sqrt{\frac{5}{2\pi}} \cdot \frac{yz\cdot(yz^2-3r^2}{r^4}$		-1	B_{3g}	B_3	B_g	B_2	B	A″	A_g	A
$g_{xyz^2} = \frac{i}{\sqrt{2}}(Y_4^{-2} - Y_4^2) = \frac{3}{4}\sqrt{\frac{5}{\pi}} \cdot \frac{xy\cdot(7z^2-r^2)}{r^4}$	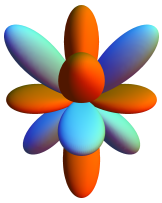	-2	B_{1g}	B_1	A_g	A_2	A	A′	A_g	A
$g_{y^3z} = \frac{i}{\sqrt{2}}(Y_4^{-3} + Y_4^3) = \frac{3}{4}\sqrt{\frac{35}{2\pi}} \cdot \frac{yz\cdot(3x^2-y^2)}{r^4}$	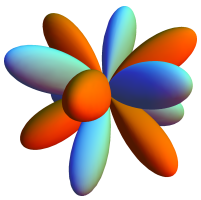	-3	B_{3g}	B_3	B_g	B_2	B	A″	A_g	A

Continued on next page

Cubic Harmonic	m_ℓ	Irreducible Representation						
		D_{2h}	D_2	C_{2h}	C_{2v}	C_2	C_s	C_i	C_1
$g_{xy(x^2-y^2)} = \frac{i}{\sqrt{2}}(Y_4^{-4} - Y_4^4) = \frac{3}{4}\sqrt{\frac{35}{\pi}} \cdot \frac{xy(x^2-y^2)}{r^4}$ 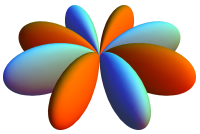	-4	B_{1g}	B_1	A_g	A_2	A	A′	A_g	A

C

Pointgroup Determination

The main section of the python code which determines the point group of the molecule. The function is essentially a set of if statements following the tests in fig. 3.13, and is described in source 1.

Table C.1: Geometries provided by the QN Express functions. The functions return a set of all orientations of all the input geometries which have all of the listed symmetry operations. If there are no possible orientations, then an empty set is returned.

`getC2Geoms`	$C_2(z)$
`getTripleC2Geoms`	$C_2(x)$, $C_2(y)$, $C_2(z)$
`getInversionGeoms`	i
`getDoubleReflectionGeoms`	σ_{xz}, σ_{yz}
`getXYReflectionGeoms`	σ_{xy}

The code uses numerous functions not defined here, such as `getC2Geometries()` and `getInversionGeoms()`; the specific implementation of these functions is not important, just the knowledge of their function, they have been named so that this is self explanatory, the functions `getC2Geoms`, `getTripleC2Geoms`, `getInversionGeoms`,

`getDoubleReflectionGeoms`, and `getXYReflectionGeoms` take as an input either a `Molecule` object, a molecular geometry, or a list of molecular geometries. They return a set of molecular geometries which have the relevant symmetries, or an empty set if there are none. The sets of geometries they return are described in table C.1.

Note that the order the tests are carried out in is important, as it defines which branch of the graph in fig. 3.13 is traversed.

The source to `getC2Geoms` is also included, as it is the most complex of the `get*Geoms` functions, and the others either omit, or reuse much of its functionality. It is listed in source 2, and can be described as such:

1. For each atom, and all the midpoints of pairs of atoms of the same type:
2. Create a new geometry, where the point has been rotated onto the Z axis, and add them to the list `allGeoms`.
3. Create a new list, `c2Geometries`. Iterate through `allGeoms`, testing each geometry to see if it has C_2 symmetry, adding those which pass to the list `c2Geometries`.
4. Return `c2Geometries`.

Step 1 here is the key step, ultimately, there are two situations which can happen when a molecule has C_2 symmetry, either an atom is on the rotation axis, and so does not need a *partner* to map onto, or it has said partner atom to map to - in which case, the midpoint has to be on the rotation axis. By taking every atom and every midpoint of pairs of like atoms, and creating a geometry for each, we create geometries prepared for this requirement. The tests then simply remove molecules which don't posses the symmetry.

Once this first test is done, only rotations about the Z axis need be done to ensure higher symmetry (if the molecule does not have C_2 rotation symmetry, then may need to be rotated about X (or Y) to fit the reflection plane $\sigma(xy)$, which is done in much the same way - rotating about X (or Y, it does not matter) to place midpoints of pairs of molecules on the xy plane. The fact that only Abelian point groups need to be considered simplifies this, as only C_2 rotations need to be considered, so only pairs of atoms need to be considered.

```python
def getC2Geometries(geoms):

    if type(geoms) is list:
        geoms = [geom for geom in geoms]
    else:
        geoms = [geoms]

    allGeoms = geoms[:]

    for mol in geoms:
        for atom in mol:
            if norm(atom.coords()) > 1e-5:
                alpha = atan2(atom.y, atom.x)
                beta = atan2(sqrt(atom.x**2 + atom.y**2), atom.z)

                newMol = Molecule(mol)

                newMol.rotZ(-alpha)
                newMol.rotY(-beta)
                allGeoms.append(newMol)


        for atom1 in mol:
            for atom2 in mol:
                if atom1.name == atom2.name
                   and (norm(atom1.coords()) - norm(atom2.coords()) < 1e-5)
                   and atom1 != atom2:
                    x,y,z = Atom.midpoint(atom1, atom2)

                    # check it's not already on the z axis
                    if abs(x) > 0.0 and abs(y) > 0.0:
                        alpha = atan2(y, x)
                        beta = atan2(sqrt(x**2 + y**2), z)

                        newMol = Molecule(mol)
                        newMol.rotZ(-alpha)
                        newMol.rotY(-beta)
                        allGeoms.append(newMol)

    c2Geometries = []
    for geom in allGeoms:
        for atom in geom:
            rotatedAtom = Atom(atom)
            rotatedAtom.rotZ(pi)
            if rotatedAtom not in geom:
                break
        else:
            c2Geometries.append(geom)

    return c2Geometries
```

Source Code 1: QN Express `getPointGroup` (python) source code.

```
def getC2Geoms(geoms):

  if type(geoms) is list:
    geoms = [geom for geom in geoms]
  else:
    geoms = [geoms]

  allGeoms = geoms[:]

  for mol in geoms:
    for atom in mol.soloAtoms():
      if norm(atom.coords()) > 1e-5:
        alpha = atan2(atom.y, atom.x)
        beta = atan2(sqrt(atom.x**2 + atom.y**2), atom.z)

        newMol = Molecule(mol)

        newMol.rotZ(-alpha)
        newMol.rotY(-beta)
        allGeoms.append(newMol)

    for atom1 in mol:
      for atom2 in mol:
        if atom1.name == atom2.name
          and (norm(atom1.coords()) - norm(atom2.coords()) < 1e-5)
          and atom1 != atom2:
          x,y,z = Atom.midpoint(atom1, atom2)

          # check it's not already on the z axis
          if abs(x) > 0.0 and abs(y) > 0.0:
            alpha, beta = atan2(y, x), atan2(sqrt(x**2 + y**2), z)

            newMol = Molecule(mol)
            newMol.rotZ(-alpha)
            newMol.rotY(-beta)
            allGeoms.append(newMol)

  c2Geometries = []
  for geom in allGeoms:
    for atom in geom:
      rotatedAtom = Atom(atom)
      rotatedAtom.rotZ(pi)
      if rotatedAtom not in geom:
        break
    else:
      c2Geometries.append(geom)

  return c2Geometries
```

Source Code 2: QN Express `getC2Geoms` (python) source code.

D

Published Papers

OPEN ACCESS
IOP Publishing
Journal of Physics B: Atomic, Molecular and Optical Physics
J. Phys. B: At. Mol. Opt. Phys. **47** (2014) 185203 (11pp)
doi:10.1088/0953-4075/47/18/185203

R-matrix calculations of low-energy electron collisions with methane

Will J Brigg[1], **Jonathan Tennyson**[1] **and Martin Plummer**[2]

[1] Department of Physics & Astronomy, University College London, Gower St., London WC1E 6BT, UK
[2] Scientific Computing Department, STFC Daresbury Laboratory, Sci-Tech Daresbury, Cheshire WA4 4AD, UK

E-mail: will@theory.phys.ucl.ac.uk, j.tennyson@ucl.ac.uk and martin.plummer@stfc.ac.uk

Received 7 May 2014, revised 22 June 2014
Accepted for publication 26 June 2014
Published 11 September 2014

Abstract

R-matrix calculations are performed for electron collision with CH_4 at energies between 0.02 and 15 eV using a series of different *ab initio* models for both the target and the full scattering system. A target model similar to the standard multi-reference configuration interaction used in electronic structure calculations is found to give the best results. Results are presented for elastic scattering, with particular emphasis on the Ramsauer–Townsend miminum, and for rotational excitation, momentum transfer and electron impact dissociation. Extensive comparisons are made with previous studies.

Keywords: elastic scattering, rotational excitation, electron impact dissociation, eigenphases

(Some figures may appear in colour only in the online journal)

1. Introduction

Cross sections for electron collisions with methane are important for a number of different applications including combustion (Goodings *et al* 1979, Prager *et al* 2007) and plasma-enhanced combustion (Wisman *et al* 2007), the atmosphere of Titan (Cravens *et al* 2010) and chemical vapour deposition (Baek *et al* 2013). As a result a number of compilations of recommended values for these cross sections have been performed (Morgan 1992, Shirai *et al* 2002, Kato *et al* 2009, Reiter and Janev 2010, Fuss *et al* 2010, Song *et al* 2014). Individual experimental studies are discussed later in the paper.

Methane has become a standard system for testing theoretical methods (Lengsfield III *et al* 1991, Winstead *et al* 1993, Bettega *et al* 1993, Nestmann *et al* 1994). However it is well-established that close-coupling based methods have difficulty converging the polarization potential (Gil *et al* 1994, Varambhia *et al* 2008). Theoretical treatments have considered elastic scattering (Boesten and Tanaka 1991, Jain and Baluja 1992, Machado *et al* 2002), as well as electron impact rotational (Jain and Thompson 1983, Brescansin *et al* 1989, Machado *et al* 2002), vibrational (Althorpe *et al* 1995, Čurík *et al* 2008) and electronic excitation (Gil *et al* 1994, Bettega *et al* 1998, Winstead *et al* 1993, Kato *et al* 2009). Recently Ziółkowski *et al* (2012) used a close-coupling R-matrix calculation to obtain electronically inelastic collisional excitation cross sections; they then used a high-level electronic structure calculation to determine excited state energies and derivative couplings, and trajectory surface hopping to determine branching in the dissociation of the methane. None of these theoretical treatments provide a comprehensive solution to the low-energy electron scattering problem. Such a solution would, for example, provide a good representation of the well-known Ramsauer–Townsend minimum, which is very sensitive to the treatment of polarization, and at the same time consider electron impact electronic excitation which, in the case of methane, means representing diffuse electronically excited states which have a significant Rydberg character.

Rydberg states are not usually well represented in close-coupling expansions based upon standard treatments of the target molecule electronic structure. Special procedures have been proposed by Gil *et al* (1994) and Rozum *et al* (2003) for treating Rydberg states in close-coupling studies. More

generally the molecular R-matrix with pseudostates (RMPS) method (Gorfinkiel and Tennyson 2004, 2005) has been demonstrated to give an excellent representation of polarization effects (Halmová and Tennyson 2008, Zhang *et al* 2011). In this work we develop a comprehensive, *ab initio* model for the low energy scattering of electrons from methane which considers elastic scattering and rotational excitation at energies spanning the Ramsauer–Townsend minimum, as well as electron impact electronic excitation and hence impact dissociation.

Our aim was to create a single model which replicated the specific features of the low-energy electron-methane collision system simultaneously. To do this we concentrated on three main aspects of the problem: the location (and presence) of the Ramsauer–Townsend minimum, the polarizability of the methane target, and the thresholds for the electronic excitations of the target. The following section gives an overview of the theory used, and then describes our attempts to develop a unified model. Section 3 presents and discusses our results with the final section giving conclusions.

2. Method of calculation

2.1. Theory

Calculations were all performed using the R-matrix method as implemented in the Quantemol-N expert system (Tennyson *et al* 2007) and the recently updated UKRMol programs (Carr *et al* 2012). This methodology has been thoroughly reviewed (Tennyson 2010, Burke 2011) and we will therefore only consider aspects of the problem associated with this paper.

The basic idea of the R-matrix method is the division of space into an inner region, which encloses the entire charge cloud of the N-electron target molecule, and an outer region. Within the inner region the interaction of the scattering electron with the target is complicated: both correlation and exchange effects need to be considered in detail. The $N+1$ electron wavefunction in this region is generally written:

$$\psi_k^{N+1} = \mathcal{A}\sum_{ij} a_{ijk}\Phi_i^N(\mathbf{x}_1 \ldots \mathbf{x}_N)u_{ij}(\mathbf{x}_{N+1}) + \sum_i b_{ik}\chi_i^{N+1}(\mathbf{x}_1 \ldots \mathbf{x}_{N+1}), \quad (1)$$

where Φ_i^N is the wave function of ith target state. For a many electron system such as methane, the target wave function itself is represented by a sum over configurations:

$$\Phi_i^N = \sum_m c_{im}\chi_m^N(\mathbf{x}_1 \ldots \mathbf{x}_N). \quad (2)$$

in equation (1), u_{ij} are the extra orbitals introduced to represent the scattering electron, here represented by Gaussian type orbitals (GTOs) (Faure *et al* 2002). The electrons in the scattering wave function must obey the Pauli principle and are therefore anti-symmetrized by operator $\mathcal{A}$. The UKRMol codes use a particularly efficient procedure for treating wavefunctions in this form (Tennyson 1996a).

The second summation in equation (1) involves configurations which have no amplitude on the R-matrix boundary and where all electrons are placed in orbitals associated with the target. Since they are confined to a finite volume of space they are often referred to as L^2 configurations. Such configurations allow for relaxation of the orthogonalization between the continuum orbitals and those belonging to the target and are also used to model the effects of target polarization. Different models are discussed extensively below; L^2 configurations are generated for each these models by placing an extra electron (the scattering electron) in any of the orbitals specified subject to the constraints of occupancy and overall symmetry. Doing this requires care with the phase of the overall wavefunction (Tennyson 1997).

In standard close-coupling treatments, the first summation over i in equation (1) runs over the target electronic states included in the model. Given that even without considering the target continuum, there are an infinite number of target states to consider, this sum is always truncated. The RMPS method (Bartschat *et al* 1996) uses the properties of the R-matrix method to try and create effectively complete close-coupling expansions. In terms of equation (1), this is done by extending the sum over i to run over a set of pseudo-states. These states are designed to give a complete representation of all the target electronic states, including the continuum, up to some total energy but only within the confines of the R-matrix sphere. In practice this is done by adding an extra basis set at the centre of the system; for molecules this involves an additional set of even-temperered GTOs (Gorfinkiel and Tennyson 2004).

Methane in its equilibrium geometry has T_d symmetry. However the polyatomic implementation of the UKRMol codes only treats Abelian groups which in practice means D_{2h} and its subgroups (Morgan *et al* 1997). Here methane was treated using C_{2v} symmetry. D_2 symmetry can also be used and allows only a single H atom to be defined. However, tests found that D_2 calculations yield the same results, with no noticable computational advantages. Care was taken in all models to preserve the degeneracies present in a fully symmetrized calculation. Where possible our results are presented below using T_d symmetry. A C–H bondlength of 1.093 95 Å was used for all calculations. All calculations used Hartree–Fock orbitals in the target representation.

2.2. Target wavefunctions

A scattering model comprises a target representation and a treatment of the '$N+1$ electron' scattering system. Clearly the target polarizability and electronic excitation thresholds are properties of the target model alone, whereas the treatment of the Ramsauer–Townsend (RT) minimum depends on both steps. Below we discuss a number of different target models we tested, in choosing between them it is also necessary to consider results obtained using them in scattering calculations.

2.2.1. Complete actice space configuration interaction. The treatment of electronic excitation necessarily involves using

target wavefunctions determined using configuration interaction (CI) based procedure. In practice each term is defined using configuration state functions (CSFs) which define the distribution of the electrons between orbitals and the associated spin-couplings. Use of a complete active space (CAS) CI representation of the target has certain advantages when balancing the N and $N+1$ electron calculations (Tennyson 1996b). A CASCI target wavefunction includes all possible CSFs generated using a given orbital set and can be described as:

$$[\text{core}]^n[\text{CAS}]^{(N-n)},$$

where n electrons are frozen in core orbitals and the remaining $(N-n)$ target electrons are distributed freely across a set of suitable selected valence orbitals. All our calculations froze at least the electrons in the $1a_1$ (carbon 1 s) orbital. A small CASCI calculation for methane might be given by:

$$\left[1a_1\right]^2\left[2a_1,\,1t_2,\,2t_2\right]^8,$$

which comprises the ground configuration plus the lowest unoccupied molecular orbital (LUMO). In practice this model gives a target polarizability which is far too small, no RT minimum in the associated scattering calculation, and electronic excitations which are too high. Given that the RT minimum is a feature of low-energy electron scattering caused by a cancellation between the repulsive, static exchange potential and the attractive polarization potential, it is to be expected that underestimating the polarizability will lead to a poor representation of the minimum.

A more reasonable CAS distributes the eight valence electrons amongst the 8 active or valence orbitals, giving the following model:

$$\left[1a_1\right]^2\left[2a_1,\,3a_1,\,1t_2,\,2t_2\right]^8.$$

In fact, it was found that freezing the lowest four electrons had little effect on calculated cross sections, while drastically reducing the computation time, so the following CASCI model was used as a base for the remainder of the calculations.

$$\left[1a_1,\,2a_1\right]^4\left[3a_1,\,1t_1,\,2t_2\right]^6.$$

In a CASCI calculation increasing the number of active orbitals improves all aspects of the calculation. In practice, this approach offers rapidly diminishing returns as using an enlarged CAS gives only a modest improvement to the scattering calculation for a large increase in computational cost (Tennyson 1996b). Increasing the size of the active space has a larger effect on the excitation energies than the polarizability. Including extra orbitals in the active space does give an RT minimum eventually, where the number of orbitals required for it to present depends on the basis set. Using a larger basis set with more diffuse functions tended to give the RT minimum sooner. 6-311G* gave an RT minimum for all models examined, as did cc-pVDZ (though surprisingly cc-pVTZ did not). Including the first 4 LUMOs meant that all basis sets tested produced an RT minimum (with the exception of TZ), although they were all located too low in energy. The smaller basis sets also produced larger total cross sections above about 2 eV (larger by about 1 Å^2 at the peak). The same shifting of thresholds and the peak is seen when including more orbitals.

Table 1. First excitation threshold for different basis sets where the CAS is $[1a_1,\,2a_1]^4[3a_1,\,1t_1,\,2t_2]^6$, and polarizabilities are computed using all states up to 25 eV.

Basis set	First threshold (eV)	Polarizability (a_0^3)
DZP	13.853	9.14
TZ	13.650	8.11
6-31G*	12.335	11.27
6-31G	12.300	11.50
cc-pVDZ	11.626	9.69
cc-pVTZ	11.404	8.30
6-311G*	11.403	7.52
6-311G	11.372	7.75

Excitation energies and polarizabilties as a function of basis set used are shown in table 1. The value of the vertical excitation threshold for the first excited state, which is a repulsive triplet state, is not particularly well determined experimentally but would appear to be in the region of 8.8 eV (Brongersma and Oosterhoff 1969) and 9.0 eV (Kanik *et al* 1993). As can be seen from the table, theory tends to overestimate these values with Ziółlkowski *et al* (2012) obtaining 10.01 eV. Our final scattering calculations presented below use a model for which the threshold to excitation is 10.58 eV, although some of our other models gave values lower than this.

The polarizabilities presented in table 1 are consistently too low, ranging from 7.5–11.5 a_0^3, where the experimental value is 16.52 a_0^3 (Olney *et al* 1997). The polarizabilities can be improved beyond those in the table by including more states in the target region, but the gains are small and the computational cost high. Even if all the states are included, this approach still leads to polarizabilities which converge to less than the true value (Jones and Tennyson 2010). The dependence of the polarizability on basis and model is slightly complicated as approximate wavefunctions are often more polarizable than their more exact counterparts. This means that the calculated polarizabilty may decrease as the calculation is improved (Jones and Tennyson 2010). Up to this point, all test calculations were performed using a standard CASCI model. These tested included some very large CASCI treatments; up to $[1a_1]^2[2-5a_1,\,1-4t_1,\,1-4t_2,\,1e]^8$, which would have been impractical to use in a full $N+1$ scattering treatment (Halmová *et al* 2008).

2.2.2. Rydberg model. Methane's low-lying excited electron states are diffuse and have a strong Rydberg character. An attempt at modelling this was made including several additional diffuse functions using standard basis sets on the carbon without changing the CAS. These treatments lowered the excitation energies, but not significantly.

Next we tested the role of the CAS. Our model used a core CAS with the option of exciting a single electron outside this CAS. This model can be described by CSFs of the form:

$$[\text{core}]^{n}[\text{CAS}]^{(N-n)}$$
$$[\text{core}]^{n}[\text{CAS}]^{(N-n-1)}[\text{Rydberg}]^{1}.$$

For example, the main model we tested had CSFs defined by:

$$\left[1a_1, 2a_1\right]^4\left[3a_1, 1t_2, 2t_2\right]^6$$
$$\left[1a_1, 2a_1\right]^4\left[3a_1, 1t_2, 2t_2\right]^5\left[4a_1, 3t_2, 4t_2, 1e\right]^1.$$

We tested two different basis sets to represent Rydberg-like orbitals, which were added to the carbon basis set since the carbon is located at the centre-of-mass. The first basis was a set of quasi-Slater type orbitals recreated from Rozum *et al* (2003) as a sum of six GTOs each. The second set were GTOs taken from Nestmann *et al* (1994). These attempts gave large orbital spaces, the largest being $[8a_1, 5t_1, 7t_2, 3e]$; these procedures gave significantly lower ground state energies but proved computationally expensive, where the target calculation alone took a whole day on a high end workstation; although these calculations were performed prior to the diagonalization routines being improved (Zhang *et al* 2011). The results of the two different basis sets were very similar. Increasing the number of orbitals in the extended space decreases the ground energy monotonically, with larger calculations giving lower results–the calculations are variational, so this is exactly as expected. This model improved upon all aspects of the CASCI target model. The results of this model were promising, however to obtain a reasonable polarizability, the number of states required in the inner region was very large—with some tests reaching 1000 states. The RMPS method is proposed as a solution to this.

2.2.3. RMPS. The previous calculations which attempted to represent Rydberg states predate the development of the molecular RMPS method (Gorfinkiel and Tennyson 2004, 2005). In fact the two procedures have some similarities since the RMPS method involves using the same CSFs as in the Rydberg model, but uses a distinct basis set for the RMPS orbitals—a set of even-tempered GTOs placed on the molecular centre-of-mass. These orbitals are designed to fill up all the space inside the R-matrix sphere, representing the Rydberg states leading up to ionization and continuum of states, found above the ionization limit, within this sphere.

We therefore undertook a series of RMPS calculations. For these calculations, the RMPS orbitals were represented using even-tempered GTOs with 14 functions for s, p, and d functions, each with $\alpha_0 = 0.05$ and $\beta = 1.4$. The orthogonalization thresholds used in the N, and $N + 1$ electron regions were 2×10^{-4} and 1×10^{-6}, respectively.

As with the Rydberg Model, the polarizability is dependent on the number of states included, and increases aymptotically with increasing numbers of states. Including all states up to 30 eV gave a value within 15% of experiment. The RMPS approach again improved all aspects of the target model over the Rydberg Model, ground energies, first excitation thresholds, and polarizabilities are shown in table 2.

The RMPS method gives a good target description but we encountered problems when it was used as part of a scattering calculation: the model predicted an unphysical bound anionic state. First, it was thought this might be a linear dependance problem (Little and Tennyson 2014), particularly because this was the first time the molecular RMPS method had been used with an atom placed on the centre-of-mass. The integral codes had to be adapted to cope with this, and the deletion thresholds to deal with linear dependence closely monitored, and adjusted. Increasing the deletion thresholds did not fix the model. Second, we tested the effects of the RMPS orbitals being used. After several other tests the space-filling, even-tempered GTOs were replaced by the virtual orbitals generated by a cc-pVTZ calculation. However this also had little effect: the cross sections obtained after this change were very similar to the standard RMPS ones. Third, a closer inspection of the configurations used in the target model compared to those used in the scattering calculation suggested that the calculation was over correlated as the L^2 terms from equation (1) used in the RMPS calculation can contribute as double excitations of the target.

The unbalanced nature of the RMPS model is clearly shown by the behaviour of the low-energy eigenphase sums as the number of orbitals included in the RMPS procedure is increased. As shown in figure 1, the behaviour of the eigenphases changes abruptly with larger models. The eigenphases of the larger models are characteristic of the presence of a bound anionic state; these models also feature an R-matrix pole which lies below the energy of the target ground state. A standard CASCI calculation is balanced, by construction. An RMPS calculation may not be. How balanced a calculation must be to give physical results is not a simple problem, and the level of correlation between the N and $N + 1$ electron problems is a subtle problem (Rescigno 1994).

2.2.4. Multi-reference configuration interaction (MRCI). To try and balance the RMPS procedure we tested target models which had multiple excitations out of the CAS. Given that the cc-pVTZ basis set alone gave similar results to the cc-pVTZ + RMPS GTOs sets for the single excitation RMPS model, and given the extra complexity of using multiple basis sets and multiple orthogonalizations for the target, just the cc-pVTZ basis set alone was used to produce all orbitals. This approach may not be general as the central carbon in methane locates GTOs at the centre-of-mass.

The simplest form of this model is described by target CSFs of the form:

$$\left[1a_1, 2a_1\right]^4\left[3a_1, 1t_2, 2t_2\right]^6$$
$$\left[1a_1, 2a_1\right]^4\left[3a_1, 1t_2, 2t_2\right]^5\left[4a_1, 5a_1, 3t_2, 4t_2, 1e\right]^1$$
$$\left[1a_1, 2a_1\right]^4\left[3a_1, 1t_2, 2t_2\right]^4\left[4a_1, 5a_1, 3t_2, 4t_2, 1e\right]^2.$$

Use of this wavefunction solved the issue of the erroneous bound state, as demonstrated by inspection of the low-energy

Table 2. Ground energies, first excitation thresholds, and spherical polarizabilities (obtained by summing states up to 30 eV) for various RMPS and MRCI models. MRCI models are defined by the number of frozen orbitals in the core, and the number of possible excitations out of the CAS.

RMPS orbitals included	Ground energy E_h	Threshold (eV)	Polarizability (a_0^3)
RMPS: 2 Frozen, single excitations; $[1a_1, 2a_1]^4[3a_1 1t_2, 2t_2]^{6-(0,1)}$ [RMPS]$^{(0,1)}$			
$[3t_2]$	−40.224 66	11.291	10.92
$[4a_1, 3t_2]$	−40.226 76	10.948	11.45
$[4a_1, 3t_2, 4t_2]$	−40.257 56	10.843	12.30
$[4a_1, 3t_2, 4t_2, 1e]$	−40.272 31	10.931	13.78
$[4a_1, 5a_1, 3t_2, 4t_2, 1e]$	−40.274 74	10.928	13.84
$[4a_1, 5a_1, 1t_1, 3t_2, 4t_2, 1e]$	−40.274 74	10.928	13.84
MRCI: 2 Frozen, double excitations; $[1a_1, 2a_1]^4[3a_1, 1t_2, 2t_2]^{6-(0,1,2)}$ [RMPS]$^{(0,1,2)}$			
$[3t_2]$	−40.224 66	11.291	10.93
$[4a_1, 3t_2]$	−40.226 76	10.948	11.47
$[4a_1, 3t_2, 4t_2]$	−40.257 56	10.843	12.44
$[4a_1, 3t_2, 4t_2, 1e]$	−40.272 31	10.931	14.12
$[4a_1, 5a_1, 3t_2, 4t_2, 1e]$	−40.274 74	10.928	14.18
MRCI: 1 Frozen, triple excitations; $[1a_1]^2[2a_1, 3a_1, 1t_2, 2t_2]^{8-(0,1,2,3)}$ [RMPS]$^{(0,1,2,3)}$			
$[3t_2]$	−40.228 34	11.107	11.38
$[4a_1, 3t_2]$	−40.228 34	11.107	11.385
$[4a_1, 3t_2, 4t_2]$	−40.276 99	10.566	13.01

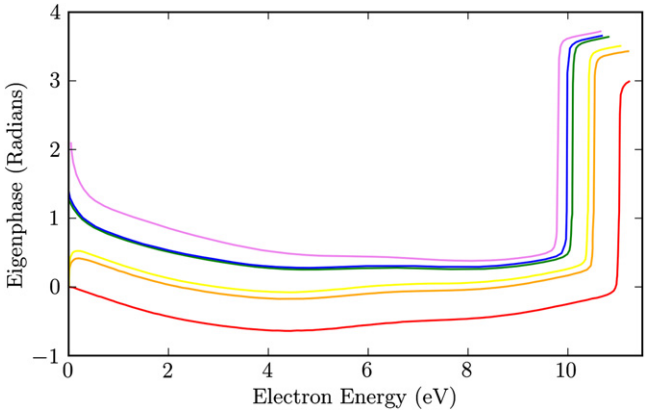

Figure 1. C_{2v} A_1 symmetry eigenphase sums for single-excitation RMPS models with increasing numbers of orbitals. All models used a target CASCI of $[1a_1, 2a_1]^4[3a_1, 1t_2, 2t_2]^6$ (red line), and are then augmented by single excitations to the following additional virtual orbitals: $[3t_2]$ (orange line); $[4a_1, 3t_2]$ (yellow line); $[4a_1, 3t_2, 4t_2]$ (green line); $[4a_1, 3t_2, 4t_2, 1e]$ (blue line); $[4a_1, 5a_1, 3t_2, 4t_2, 1e]$ (purple line).

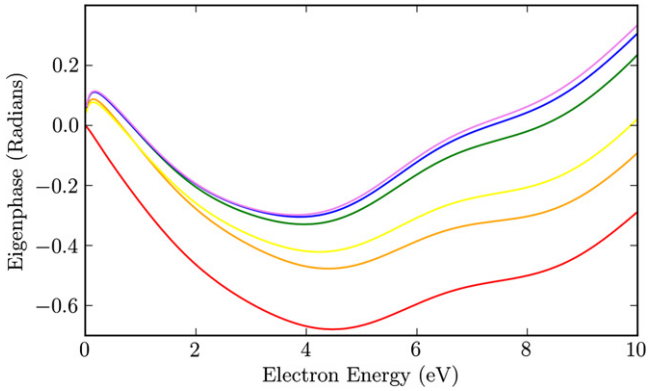

Figure 2. C_{2v} A_1 eigenphase sums at low energy for the various models examined: the CASCI model $[1a_1, 2a_1]^4[3a_1, 1t_2, 2t_2]^6$ (red line), and then the MRCI models, including single and double excitations to the following additional orbitals: $[3t_2]$ (orange line); $[4a_1, 3t_2]$ (yellow line); $[4a_1, 3t_2, 4t_2]$ (green line); $[4a_1, 3t_2, 4t_2, 1e]$ (blue line); $[4a_1, 5a_1, 3t_2, 4t_2, 1e]$ (purple line).

eigenphase sums: compare the results presented in figure 2 with those of the RMPS model given in figure 1. The corresponding elastic cross sections show an even more dramatic change at low-energy, see figure 3. We therefore decided to employ a model based on a CASCI and double excitations from it. This form of the wavefunction is similar to that produced by quantum chemical MRCI calculations. We therefore dub this the MRCI model.

Of course the MRCI model can regarded as step towards doing a complete CASCI run with a CAS of $[1 - 5a_1, 1 - 4t_2, 1e]^{10}$. The next step would be to include triple excitations. However that appears unneccesary for a balanced calculation; the improvement of double over single excitations is very significantly more than the changes found when including triples over doubles. Furthermore, the computational demands of including triple excitations is too great to be contemplated in a full calculation. The model

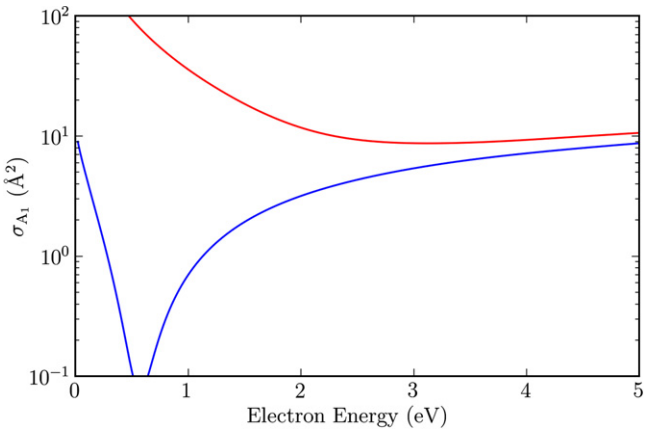

Figure 3. C_{2v} A_1 symmetry cross sections for methane when including CSFs with single and double excitations to the virtual orbitals. Red line: single excitation; blue line: double excitation.

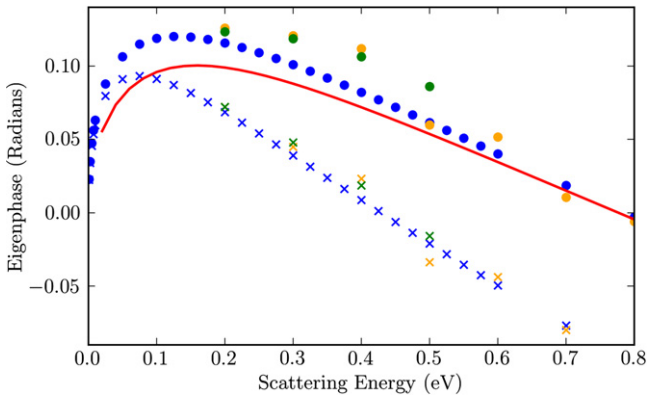

Figure 4. Low-energy eigenphases: summed C_{2v} R-matrix A_1 eigenphases (red curve). For the empirical determinations crosses represents waves only and circles summed s + p + 2d; empirical data from Ferch *et al* (1985) (green); Sohn *et al* (1986) (orange) and Fedus and Karwasz (2014) (blue).

including only single excitations gives incorrect behaviour at low energy unlike that with doubles, see the total cross sections shown in figure 3.

2.2.5. Outer region. For the smaller calculations the outer region is computationally straightforward. However when the number of target states involved becomes large, this is no longer so and to obtain a good polarizability, a large number of states are required in the sum over states expression (Jones and Tennyson 2010). For low energy, this is not an issue, as high-energy states can simply be dropped in the outer region calculation with no detriment to lower energy cross sections (Rabadán and Tennyson 1997). However this is not possible for when considering electronic excitation, as these states represent the electron impact dissociation channel. This means that all the states needed to be included, which is not feasible using the standard UKRMol codes.

This problem was solved for energies up to 15 eV using the PFARM (Sunderland *et al* 2002, Burke *et al* 2002, Sunderland *et al* 2010) codes, which perform the outer region work in a massively parallel environment. PFARM, originally designed to enable full CI calculations of electron collisions with open d-shell ions (and atoms) relevant to astrophysics, with many open channels, has recently been adapted with an interface to the UKRMol suite (Carr *et al* 2012). The current set of calculations was thoroughly tested for convergence of results with respect to variations of the long-range propagation distance at which the R-matrix is matched to asymptotic coupled radial solutions and with respect to the accuracy and stability of the series expansions used to form these solutions (Sunderland *et al* 2002). As a result of using PFARM, with distributed pipelined task-groups of cores and parallelized linear algebra (Sunderland *et al* 2010), the calculation time for a set of energies with a given symmetry using (for example) 1152 cores was reduced from months to one or two hours, making the calculations possible.

Finally, the program polyDCS (Sanna and Gianturco 1998) was run to produce rotationally resolved differential cross sections (DCS).

3. Results and discussions

A number of target basis sets and R-matrix radii were tested, however the calculations were not particularly sensitive to these. The final model used a cc-pVTZ GTO basis set, an R-matrix sphere radius of 13 a_0 and the MRCI model with the core, active and virtual spaces defined by $[1a_1, 2a_1]^4$, $[3a_1, 1t_2, 2t_2]$ and $[4a_1, 5a_1, 3t_2, 4t_2, 1e]^1$, respectively. In the outer region R-matrices were propagated to 100.1 a_0, plus or minus 10–20 a_0 for convergence tests. All subsequent results are from this model only, with 223 states included in the outer region (all states found up to 30 eV). Unless otherwise stated, the results are summed over the four symmetries given in a C_{2v} calculation: $^2A_1$, $^2B_1$, $^2B_2$ and $^2A_2$.

3.1. Eigenphases

Eigenphases are a useful diagnostic tool for comparing various models and theories. Sohn *et al* (1986) provide some empircal eigenphases extracted from their measured DCS using phaseshift analysis due to Nesbet (1979). Their analysis assumed that only partial waves up to d are important which is a dubious assumption as they considered energies as high as 5 eV. Ferch *et al* (1985) performed a modified effective range analysis of low-energy cross section measurements to give low-energy eigenphases. Very recently Fedus and Karwasz (2014) also performed an effective range analysis yielding a set of low-energy s, p and d eigenphases.

Figure 4 compares our results with those of Ferch *et al* (1985), Sohn *et al* (1986) and Fedus and Karwasz (2014) for energies below 1 eV. Our 'A_1' calculations are actually for A_1 in C_{2v} symmetry so contain contributions from other symmetries in T_d. Considering only $\ell \leqslant 2$, these eigenphases correspond to s+p+2d. It can be seen that even at 0.1 eV, partial waves with $\ell > 0$ make a significant contribution. A comparison of our eigenphases with the 'A_1' eigenphases of Fedus and Karwasz (2014) gives good agreement at higher energies, at low energy the peak in our eigenphase sum appears slightly too low. This is consistent with the fact that

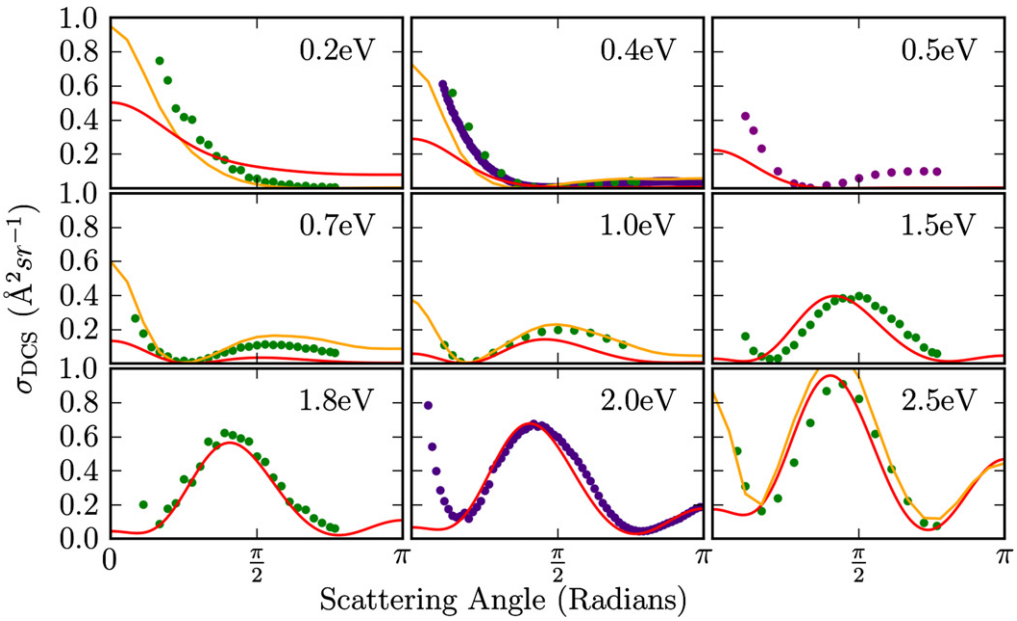

Figure 5. Differential cross sections for energies between 0.2 and 2.5 eV. Red lines: present work; orange lines: Machado *et al* (2002); purple circles: Müller *et al* (1985); green circles: Sohn *et al* (1986).

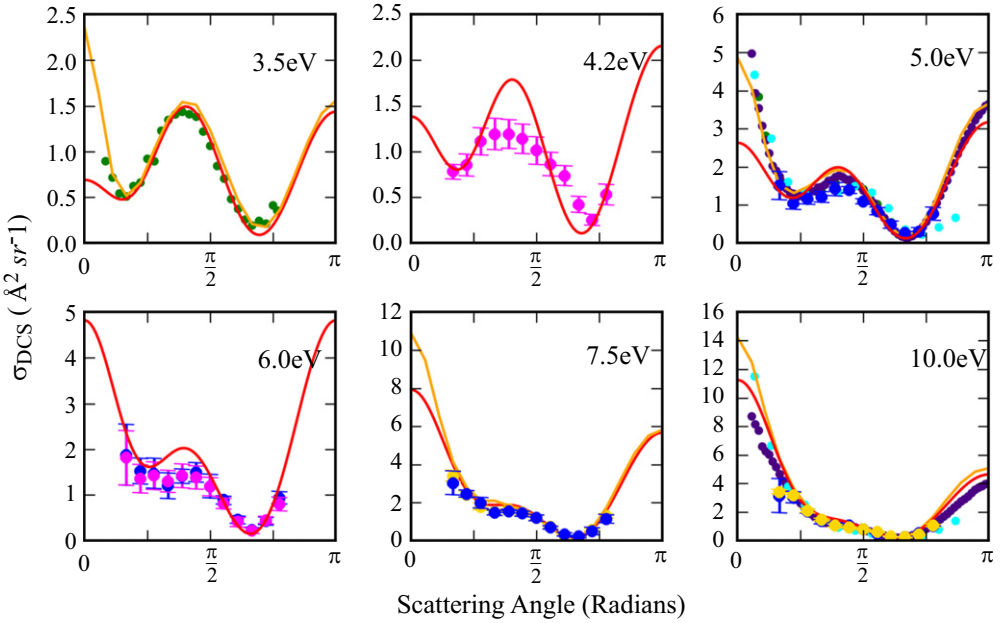

Figure 6. Differential cross sections for energies between 3.5 and 10.0 eV. Red lines: present work; orange lines: Machado *et al* (2002); purple circles: Müller *et al* (1985); light blue circles: Shyn and Cravens (1990); yellow circles: Curry *et al* (1985); dark blue circles: Tanaka *et al* (1982).

our model still does not recover the full polarizability, as discussed further below.

3.2. DCS

As seen in figure 5, the DCS do not agree well with experiment below 1 eV for a scattering angle below 30°. Above 1 eV, but below 5 eV, the agreement is good, but only above 30°. Above 5 eV, see figure 6, the agreement with experiment is excellent, and all the theories agree with just small differences in the forward scattering.

The behaviour for small angles at low energy may be due to the still incomplete representation of polarization effects. Previous calculations have shown that it is indeed at low angles and low energies that are particularly sensitive to the inclusion of polarization effects (Fujimoto *et al* 2014). However our calculation uses a truncated partial wave expansion with $\ell \leqslant 4$. The long-range polarization potential will induce minor contributions from higher partial waves. This problem was studied by O'Malley (1963) for collisions with rare gas atoms for which the polarizability is also the

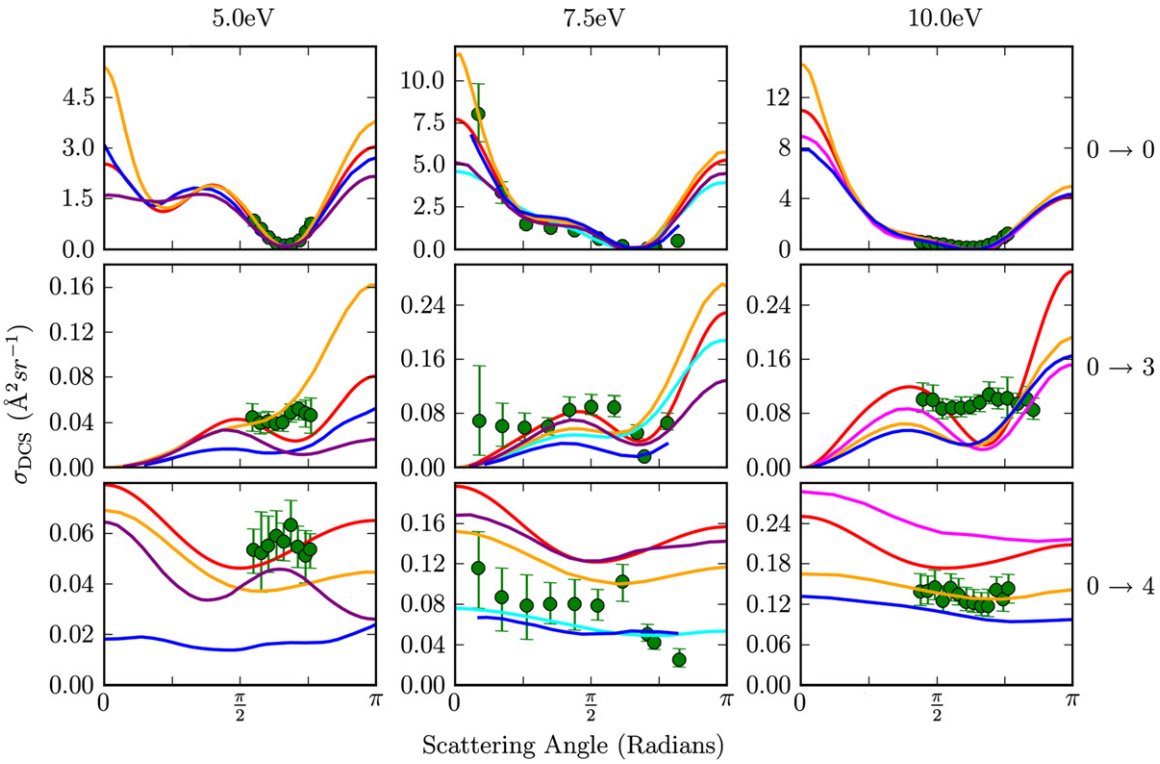

Figure 7. Comparison of rotationally resolved differential cross sections with experiment. The columns are comparisons at 5, 7.5, and 10 eV, respectively. The rows distinguish between different transitions. Red lines: present work; orange lines: Machado *et al* (2002); purple lines: Brescansin *et al* (1989); dark blue lines: Jain and Thompson (1983); light blue lines: Varella *et al* (2001); green circles: Müller *et al* (1985).

leading long-range interaction. O'Malley derives formulae for the high-ℓ contribution at low energy. Isaacs and Morrison (1996) considered this problem for non-polar linear molecules but we are not aware of a treatment for spherical tops like methane. A new version of the UKRMol codes is under development which will allow treatment of partial waves of arbitrarily high ℓ. This problem will be used as test case for these codes. In this context it is interesting to note that Machado *et al* (2002), who find significantly higher cross sections at low angles than us and hence better agreement with experiment, use ℓ up to 16 in their calculations.

3.3. Rotational excitation

Rotationally resolved DCS are also calculated, and agree well with experimental results of Müller *et al* (1985), as shown in figure 7. The elastic 0 → 0 cross section is much larger than the excitation cross sections and the calculations show differences at low angles similar to those observed for the rotationally unresolved elastic DCS. The small excitation cross sections all have a relatively large experimental uncertainty and our calculations agree reasonably well with these measurements.

Figure 8 shows that our calculated rotational excitation cross sections are in good agreement with the measured ones due to Abusalbi *et al* (1983) and Brescansin *et al* (1989).

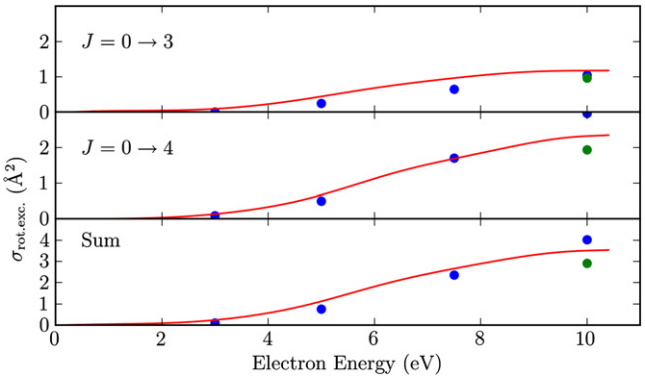

Figure 8. Rotational excitations for $J = 0 \rightarrow 3$, 4 and their sum. Red lines: present work; dark blue circles: Brescansin *et al* (1989); green circles: Abusalbi *et al* (1983).

3.4. Elastic cross section

As seen in figure 9, the calculated elastic cross section agrees well with the various experiments, the Ramsauer–Townsend minimum is present at the correct energy—albeit with a slightly lower minimum, which could be due to either to experimental cross sections being blurred by the energy resolution or our neglect of nuclear motion. Otherwise we obtain good agreement with the measured cross sections and in particular they agree with the recommendations of Song *et al* (2014), which were compiled from consideration of multiple experiment results, at all energies.

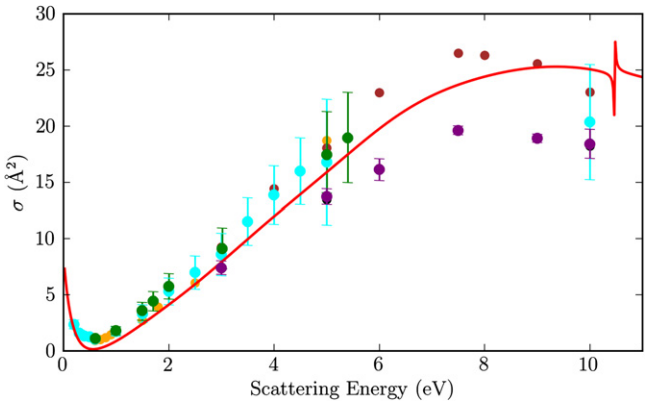

Figure 9. Elastic cross section compared with experimental results. Red lines: present work; orange circles: Sohn *et al* (1986); green circles: Bundschu *et al* (1997); brown circles: Boesten and Tanaka (1991); purple circles: Tanaka *et al* (1982); light blue circles: Song *et al* (2014). The results of Cho *et al* (2008) can be seen at 5 and 10 eV, underneath the Tanaka *et al* (1982) points.

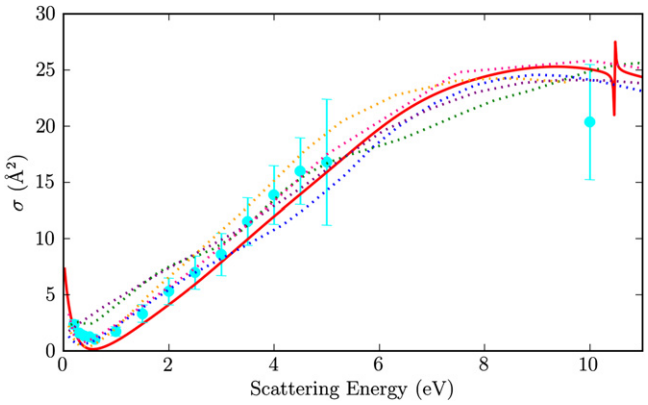

Figure 10. Elastic cross section compared with various other theories and experimental results. Red lines: present work; orange dotted line: Varambhia *et al* (2008); pink dotted line: Machado *et al* (2002); green dotted line: Ziółlkowski *et al* (2012); purple dotted line: Vinodkumar *et al* (2001); blue dotted line: Nestmann *et al* (1994); light blue circles: Song *et al* (2014).

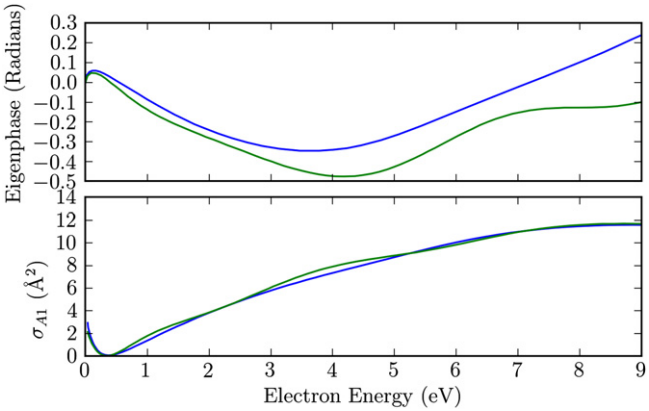

Figure 11. A_1 Eigenphase and cross section for two different inner region deletion thresholds: blue lines: 2×10^{-9} and green lines: 2×10^{-8}.

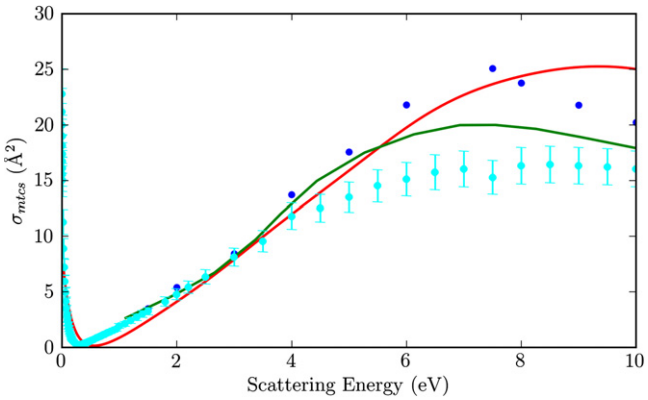

Figure 12. Momentum transfer cross section: Red lines: present work; green line: theory by Machado *et al* (2002); dark blue circles: experiment by Tanaka *et al* (1982); light blue circles: recommended by Song *et al* (2014).

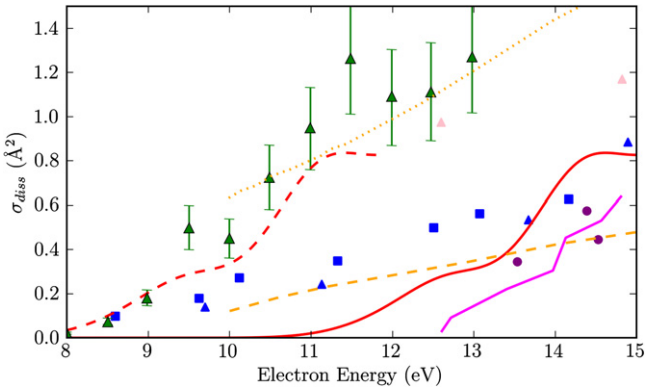

Figure 13. Electron impact dissociation cross section. Theory: red solid line: present work; red dashed line: present work, shifted to lower energy by 3.2 eV; purple solid line: Hayashi (1991); orange dashed line: CH_2 of Ziółlkowski *et al* (2012); orange dotted line: CH_3 of Ziółlkowski *et al* (2012). Experiment: blue squares: CH_2 of Nakano *et al* (1991); blue triangles: CH_3 of Nakano *et al* (1991); green triangles: CH_3 of Makochekanwa *et al* (2006); pink triangles: CH_3 of Motlagh and Moore (1998); purple circles: Winters (1975).

Figure 10 compares the elastic cross section with various other theoretical results: the other R-matrix calculations of Varambhia *et al* (2008), Ziółlkowski *et al* (2012), Vinodkumar *et al* (2001), and Nestmann *et al* (1994), as well as the Schwinger variational iterative method calculations by Machado *et al* (2002). The recommended values of Song *et al* (2014) are also given. We note that our cross section is smooth and monotonic in the energy range 1 to 10 eV, while the previous R-matrix calculations gave undulant curves. Such undulations are not physical and almost certainly are the result of an incomplete representation of the continuum due to too aggressive orthogonalization. This is illustrated in figure 11 which shows the effect of changing the deletion threshold. The results with the higher threshold show the undulations characteristic of an incomplete basis.

Figure 12 compares our momentum transfer cross section with the experimental results of Tanaka *et al* (1982), and the theoretical results of Machado *et al* (2002). Both the present work, and Machado *et al* (2002) show reasonable agreement

with the experimental values recommended by Song *et al* (2014), although in both cases the peak is shifted to higher energy.

3.5. Electron impact dissociation

All electronic excitations in methane lie above the dissociation limit and the low-lying excited states are all known to be dissociative. Therefore the dissociation cross section calculated here is simply a sum of all of the excitation cross sections, as they are all assumed to be dissociative.

Figure 13 compares results for electron impact dissociation which shows that both experiment and theory conflict. As seen earlier in figure 10, the total cross section results differ only a small amount from one another; however the dissociation cross sections are much less consistent.

There are two issues with the near-threshold behaviour of the calculated electron impact dissociation cross sections. The first is that our theoretical model overestimates the vertical excitation energy for the lowest excited state. The second is that inclusion of nuclear motion effects is likely to significantly lower this threshold, see Stibbe and Tennyson (1998). Ziółlkowski *et al* (2012) addressed these issues by shifting their cross sections to lower energy by 3.5 eV which they justified because of their overestimate of the vertical excitation threshold and because the peak in their elastic scattering calculation was too high. As our vertical excitation energy is 0.3 eV lower than theirs, figure 13 also gives our cross sections shifted to lower energy by 3.2 eV. Our shifted results give excellent agreement with the near-threshold measurements of Nakano *et al* (1991) and Makochekanwa *et al* (2006); this must however be regarded as somewhat fortuitous.

4. Conclusion

It is difficult to develop a completely *ab initio* theoretical model for low-energy electron collisions with methane which recovers all the key properties of the system such as the Ramsauer–Townsend minimum and the electronic excitation energy of low-lying, diffuse excited states. In this work we test a number of possible collision models and find that the best results are obtained using a target representation which involves use of a complete active space for the valence electrons and excitations of up to two electrons from this valence space into an extended set of virtual orbitals. By analogy with quantum chemical electronic structure calculations, we call this a MRCI model. This model gives a good representation of the Ramsauer–Townsend minimum. It also appears to give a good treatment fixed-nuclei of the electron-impact dissociation problem, although a full study of this would require considering both a better treatment of the excited Rydberg states and of nuclear motion.

The treatment of polarization could perhaps be further improved by including more states in the calculation, or by freezing fewer electrons. The approaches are not exclusive, but both increase the computational cost.

The MRCI model represents a move beyond either the use of a complete active space target of or the standard RMPS representation, although it has some similarities with the latter approach. Whether it works equally well for low-energy electron collisions with other molecules will be a matter for further study. However it is clear that use of the MRCI model is computationally demanding and its application to electron collisions with targets with many active electrons will require further algorithmic developments to make the method generally tractable.

Acknowledgments

This work made use of the facilities of HECToR, the UK's national high-performance computing service (2007–2014), which was provided by UoE HPCx Ltd at the University of Edinburgh, Cray Ltd and NAG Ltd, and funded by the Office of Science and Technology through EPSRC's High End Computing Programme. WJB thanks STFC for a CASE studentship.

References

Abusalbi N, Eades R A, Nam T, Thirumalai D, Dixon, D A, Truhlar D G and Dupuis M 1983 *J. Chem. Phys.* **78** 1213–27
Althorpe S C, Gianturco F A and Sanna N 1995 *J. Phys. B: At. Mol. Opt. Phys.* **28** 4165
Baek J J, Kim T H and Park D W 2013 *J. Nanosci. Nanotechnol.* **13** 7418–23
Bartschat K, Hudson E T, Scott M P, Burke P G and Burke V M 1996 *J. Phys. B: At. Mol. Opt. Phys.* **29** 115–23
Bettega M H F, Ferreira L G and Lima M A P 1993 *Phys. Rev.* A **47** 1111
Bettega M H F, Ferreira L G and Lima M A P 1998 *Phys. Rev.* A **57** 4987
Boesten L and Tanaka H 1991 *J. Phys. B: At. Mol. Opt. Phys.* **24** 821
Brescansin L M, Lima M A P and McKoy V 1989 *Phys. Rev.* A **40** 5577–82
Brongersma H H and Oosterhoff L J 1969 *Chem. Phys. Lett.* **3** 437
Bundschu C T, Gibson J C, Gulley R J, Brunger M J, Buckman S J, Sanna N and Gianturco F A 1997 *J. Phys. B: At. Mol. Opt. Phys.* **30** 2239–59
Burke P G 2011 *R-Matrix Theory of Atomic Collisions: Application to Atomic Molecular and Optical Processes* (Berlin: Springer)
Burke P, Noble C J, Sunderland A G and Burke V M 2002 *Phys. Scr.* **T100** 55–63
Carr J M, Galiatsatos P G, Gorfinkiel J D, Harvey A G, Lysaght M A, Madden D, Masin Z, Plummer M and Tennyson J 2012 *Eur. Phys. J.* D **66** 58
Cho H, Park Y S, Castro E A y, de Souza G L C, Iga I, Machado L E, Brescansin L M and Lee M-T 2008 *J. Phys. B: At. Mol. Opt. Phys.* **41** 045203
Cravens T E, Yelle R V, Wahlund J E, Shemansky D E and Nagy A F 2010 *Titan from Cassini–Huygens* ed R H Brown, J-P Lebreton and J H Waite (Dordrecht: Springer) chapter 10 pp 259–95
Čurík R, Čársky P and Allan M 2008 *J. Phys. B: At. Mol. Opt. Phys.* **41** 115203
Curry P J, Newell W R and Smith A C H 1985 *J. Phys. B: At. Mol. Opt. Phys.* **18** 2303
Faure A, Gorfinkiel J D, Morgan L A and Tennyson J 2002 *Comput. Phys. Commun.* **144** 224–41

Bibliography

Abusalbi, N. et al., 'Electron scattering by methane: Elastic scattering and rotational excitation cross sections calculated with ab initio interaction potentials', *J. Chem. Phys.* **78** (1983), pp. 1213 – 1227.

Ajello, J. M. et al., 'Spectroscopic Evidence for High-Altitude Aurora at Jupiter from Galileo Extreme Ultraviolet Spectrometer and Hopkins Ultraviolet Telescope Observations', *Icarus* **152** (2001), pp. 151 – 171.

Al-Refaie, A. F. and Tennyson, J., 'A parallel algorithm for Hamiltonian matrix consruction in electron-molecule collision calculations: MPI-SCATCI', *arXiv:1709.03005 [physics.comp-ph]* (????).

Almlöf, J. and Taylors, P. R., 'Computational Aspects of Direct SCF and MCSCF Methods', *in* Advanced Theories and Computational Approaches to the Electronic Structure of Molecules, volume 133 of *NATO ASI Series* (edited by C. Dykstra) (Springer Netherlands, 1984), ISBN 978-94-009-6453-2, pp. 107–125.

Althorpe, S. C., Gianturco, F. A., and Sanna, N., 'Calculation of integral cross sections for vibrationally inelastic electron-methane scattering', *J. Phys. B: At. Mol. Opt.* **28** (1995), p. 4165.

Altmann, S. L., 'On the symmetries of spherical harmonics', *Math. Proc. Cambridge* **53** (1957), p. 343.

Altmann, S. L. and Bradley, C. J., 'On the symmetries of spherical harmonics', *Philos. Tr. R. Soc. S.: A* **255** (1963), pp. 199 – 215.

Altmann, S. L. and Bradley, C. J., 'Lattice harmonics ii. hexagonal close-packed lattice', *Rev. Mod. Phys.* **37** (1965), pp. 33 – 45.

Altmann, S. L. and Cracknell, A. P., 'Lattice harmonics i. cubic groups', *Rev. Mod. Phys.* **37** (1965), pp. 19 – 32.

Antony, B. K. et al., 'R-matrix calculation of low-energy electron collisions with LiH', *J. Phys. B: At. Mol. Opt.* **37** (2004), pp. 1689–1697.

Arthurs, A. M. and Dalgarno, A., 'The Theory of Scattering by a Rigid Rotator', *Proc. Roy. Soc. A* **256** (1960), pp. 540–551.

Backx, C. and van der Wiel, M. J., 'Electron-ion coincidence measurements of CH_4', *J. Phys. B: At. Mol. Opt.* **8** (1975), p. 3020.

Baek, J., Kim, T., and Park, D., 'Synthesis of Few Layer Graphene by Non-Transferred Arc Plasma System', *J. Nanosci. Nanotechno.* **13** (2013), pp. 7418 – 7423.

Baker, S. et al., 'Probing Proton Dynamics in Molecules on an Attosecond Time Scale', *Science* **312** (2006), pp. 424 – 427.

Baluja, K. L., Noble, C. J., and Tennyson, J., 'Electronic excitation of the b $^3\Sigma_u^+$ state of H_2 using the R-matrix method', *J. Phys. B: At. Mol. Phys.* **18** (1985), p. L851.

Baluja, K. L. et al., 'Electron collisions with ClO using the R-matrix method', *J. Phys. B: At. Mol. Opt.* **33** (2000), pp. L667 – L684.

Banerjee, A. and Das, K. K., 'Theoretical spectroscopic studies of InI and InI^+', *Int. J. Quantum Chem.* **112** (2011), pp. 453 – 469.

Bartschat, K. et al., 'Electron - atom scattering at low and intermediate energies using a pseudo-state R -matrix basis', *J. Phys. B: At. Mol. Opt.* **29** (1996), p. 115.

Bederson, B. and Kieffer, L. J., 'Total Electron-Atom Collision Cross Sections at Low Energies-A Critical Review', *Rev. Mod. Phys.* **43** (1971), pp. 601–640.

Bencze, L. et al., 'Mass spectrometric investigation of the equilibrium gas-phase composition over InI3 at elevated temperatures', *Organic Mass Spectrometry* **28** (1993), pp. 1570–1576.

Best, T. et al., 'Absolute Photodetachment Cross-section Measurements for Hydrocarbon Chain Anions', *The Astrophysical Journal* **742** (2011), p. 63.

Bettega, M. H. F., Ferreira, L. G., and Lima, M. A. P., 'Transferability of local-density norm-conserving pseudopotentials to electron-molecule-collision calculations', *Phys. Rev. A* **47** (1993), p. 1111.

Bettega, M. H. F., Ferreira, L. G., and Lima, M. A. P., 'Electronic excitation of XH_4 (X= C, Si, Ge, Sn, Pb) by electron impact', *Phys. Rev. A* **57** (1998), p. 4987.

Blaga, C. I. et al., 'Imaging ultrafast molecular dynamics with laser-induced electron diffraction', *Nature* **483** (2012), pp. 194 – 197.

Bloch, C., 'Une formulation unifiée de la théorie des réactions nucléaires', *Nuclear Physics* **4** (1957), pp. 503 – 528.

Boesten, L. and Tanaka, H., 'Elastic DCS for e+CH4 collisions, 1.5-100 eV', *J. Phys. B: At. Mol. Opt.* **24** (1991), p. 821.

Bradforth, S. E. et al., 'Photoelectron spectroscopy of CN^-, NCO^-, and NCS^-', *J. Chem. Phys.* **98** (1993), pp. 800–810.

Brescansin, L. M., Lima, M. A., and McKoy, V., 'Cross sections for rotational excitation of CH_4 by 3-20-eV electrons', *Phys. Rev. A* **40** (1989), pp. 5577 – 5582.

Brigg, W. J., Tennyson, J., and Plummer, M., 'R-matrix calculations of low-energy electron collisions with methane', *J. Phys. B: At. Mol. Opt.* **47** (2014), p. 185203.

Brigg, W. J. et al., 'Calculated photoionization cross sections using Quantemol-N', *Jpn. J. Appl. Phys.* (2015).

Brunger, M. J. and Buckman, S. J., 'Electron - molecule scattering cross-sections. I. Experimental techniques and data for diatomic molecules', *Phys. Rep.* **357** (2002), pp. 215 – 458.

Brunger, M. J., Buckman, S. J., and Newman, D. S., 'Low Energy Electron Scattering From H_2', *Aust. J. Phys.* **43** (1990), pp. 665 – 682.

Buckman, S. J. and Mitroy, J., 'Analysis of low-energy electron scattering cross sections via effective-range theory', *J. Phys. B: At. Mol. Opt.* **22** (1989), p. 1365.

Bundschu, C. T. et al., 'Low-energy electron scattering from methane', *J. Phys. B: At. Mol. Opt.* **30** (1997), pp. 2239 – 2259.

Burke, P. et al., 'Electron collisions with iron peak elements: a computational grand challenge', *Phys. Scripta.* **T100** (2002), pp. 55 – 63.

Burke, P. G., 'R-Matrix Theory of Atomic and Molecular Processes', *in* Atomic Physics 5 (edited by R. Marrus, M. Prior, and H. Shugart) (Springer US, 1977), ISBN 978-1-4613-4204-5, pp. 293–311.

Burke, P. G. and Berrington, K. A. (eds.), 'Atomic and Molecular Processes: an R-Matrix Approach', (CRC Press, 1993).

Burke, P. G., Hibbert, A., and Robb, W. D., 'Electron scattering by complex atoms', *J. Phys. B: At. Mol. Opt.* **4** (1971), p. 153.

Burke, P. G., Mackey, I., and Shimamura, I., 'R-matrix theory of electron-molecule scattering', *J. Phys. B: At. Mol. Opt.* **10** (1977), p. 2497.

Burke, P. G., McVicar, D. D., and Smith, K., 'The excitation of He^+ by electrons', *Proc. Phys. Soc.* **83** (1964), pp. 397–407, cited By (since 1996)6.

Burke, P. G. and Robb, W. D., 'The R-Matrix Theory of Atomic Processes', *Adv. Atom. Mol. Phys.* **11** (1976), pp. 143 – 214.

Burke, P. G. and Schey, H. M., 'Elastic Scattering of Low-Energy Electrons by Atomic Hydrogen', *Phys. Rev.* **126** (1962), pp. 147–162.

Burke, V. M. and Noble, C. J., 'Farm - A flexible asymptotic R-matrix package', *Comput. Phys. Commun.* **85** (1995), pp. 471 – 500.

Carr, J. et al., 'UKRmol: a low-energy electron- and positron-molecule scattering suite', *The European Physical Journal D* **66** (2012), 58.

Cho, H. et al., 'A comparative experimental-theoretical study on elastic electron scattering by methane', *J. Phys. B: At. Mol. Opt.* **41** (2008), p. 045203.

Chu, S. and Dalgarno, A., 'Rotational excitation of CH^+ by electron impact', *Phys. Rev. A* **10** (1974), pp. 788–792.

Chung, H.-K. et al., 'Uncertainty estimate for theoretical atomic and molecular data', *J. Phys. D: Appl. Phys.* **49** (2016).

Collins, L. A. and Schneider, B. I., 'Linear algebraic approach to electronic excitation of atoms and molecules by electron impact', *Phys. Rev. A* **27** (1983), pp. 101–111.

Cooper, D. L. and Kirby, K., 'Theoretical study of low lying $^1\Sigma^+$ states and $^1\Pi$ states of CO potential energy curves and dipole moments.', *J. Chem. Phys.* **87** (1987), pp. 424 – 432.

Cravens, T. E. et al., 'Composition and Structure of the Ionosphere and Thermosphere', *in* Titan from Cassini-Huygens (edited by R. H. Brown, J.-P. Lebreton, and J. H. Waite), chapter 10 (Springer Netherlands, 2010), pp. 259 – 295.

Crees, M. A., 'ASYPCK, a program for calculating asymptotic solutions of the coupled equations of electron collision theory', *Comput. Phys. Commun.* **19** (1980), pp. 103 – 137.

Crees, M. A., 'ASYPCK2, an extended version of ASYPCK', *Comput. Phys. Commun.* **23** (1981), pp. 181 – 198.

Cukras, J. et al., 'Photoionization cross section by Stieltjes imaging applied to coupled cluster Lanczos pseudo-spectra', *J. Chem. Phys.* **139** (2013), p. 094103.

Čurík, R., Čársky, P., and Allan, M., 'Vibrational excitation of methane by slow electrons revisited: theoretical and experimental study', *J. Phys. B: At. Mol. Opt.* **41** (2008), p. 115203.

Curry, P. J., Newell, W. R., and Smith, A. C. H., 'Elastic and inelastic scattering of electrons by methane and ethane', *J. Phys. B: At. Mol. Opt.* **18** (1985), p. 2303.

Darby-Lewis, D., Mašín, Z., and Tennyson, J., 'R-matrix calculations of electron impact electronic excitation of BeH', *J. Phys. B: At. Mol. Opt.* (2017).

Demekhin, P. V., Ehresmann, A., and Sukhorukov, V. L., 'Single center method: A computational tool for ionization and electronic excitation studies of molecules', *J. Chem. Phys.* **134** (2011), p. 024113.

Ditchfield, R., Hehre, W. J., and Pople, J. A., 'Self consistent molecular orbital methods IX. An extended Gaussian type basis for molecular orbital studies of organic molecules', *J. Chem. Phys.* **54** (1971), pp. 724–728.

Douguet, N., Kokoouline, V., and Orel, A. E., 'Photodetachment cross sections of the $C_{2n}H^-$ ($n = 1 \rightarrow 3$) hydrocarbon-chain anions', *Phys. Rev. A* **90** (2014), p. 063410.

Dunning, T. H., 'Gaussian basis sets for use in correlated molecular calculations. I. The atoms boron through neon and hydrogen', *J. Chem. Phys.* **90** (1989), pp. 1007–1023.

Fabrikant, I. I., 'R-matrix theory of vibrational excitation of the HCl molecule by slow electrons in the adiabatic approximation', *J. Phys. B: At. Mol. Opt.* **18** (1985), p. 1873.

Farley, J. W., 'Photodetachment cross sections of negative ions: The range of validity of the Wigner threshold law', *Phys. Rev. A* **40** (1989), pp. 6286 – 6292.

Faure, A. et al., 'GTOBAS: fitting continuum functions with Gaussian-type orbitals', *Comput. Phys. Commun.* **144** (2002), pp. 224–241.

Fedus, K. and Karwasz, G. P., 'Ramsauer-Townsend minimum in methane - modified effective range analysis', *Eur. Phys. J. D* **68** (2014), 93.

Ferch, J., Granitza, B., and Raith, W., 'The Ramsauer minimum of methane', *J. Phys. B: At. Mol. Opt.* **18** (1985), pp. L445–L450.

Flannery, M. R. and Öpik, U., 'The photoionization of the hydrogen molecule from the ground electronic and vibrational state', *Proc. Phys. Soc.* **86** (1965), pp. 491 – 500.

Fuente, A. et al., 'On the chemistry and distribution of HOC^+ in M82', *Astron. Astrophys.* **492** (2008), pp. 675 – 684.

Fujimoto, M. M., Brigg, W. J., and Tennyson, J., 'R-Matrix calculations of differential and integral cross sections for low-energy electron collisions with ethanol', *Eur. Phys. J. D* **66** (2012).

Fujimoto, M. M., Tennyson, J., and Michelin, S. E., 'Low-energy electron collisions with the alanine molecule', *Eur. Phys. J. D* **68** (2014), p. 67.

Fuss, M. C. et al., 'Electron-methane interaction model for the energy range 0.1-10000eV', *Chem. Phys. Lett.* **486** (2010), pp. 110 – 115.

Gailitis, M., 'New forms of asymptotic expansions for wavefunctions of charged-particle scattering', *J. Phys. B: At. Mol. Opt.* **9** (1976), p. 843.

Geppert, W. D. and Larsson, M., 'Dissociative recombination in the interstellar medium and planetary ionospheres', *Mol. Phys.* **106** (2008), pp. 2199–2226.

Gianturco, F. A. and Thompson, D. G., 'Computed static potentials for AH_n molecules: a scattering-orintated form', *Chemical Physics* **14** (1976), pp. 111 – 120.

Gil, T. J. et al., '*Ab initio* complex Kohn calculations of dissociative excitation of methane: Close-coupling convergence studies', *Phys. Rev. A* **49** (1994), pp. 2551 – 2560.

Girivheva, N. I. et al., 'Electron-diffraction studies on the In-I system. IV. Geometrical configuration, vibrational frequencies, and molecular energetics for indium iodide', *J. Struct. Chem+* **29** (1989), pp. 695–701.

Goodings, J. M., Bohme, D. K., and Ng, C.-W., 'Detailed ion chemistry in methane - oxygen flames. I. Positive ions', *Combust. Flame* **36** (1979), p. 27.

Gorfinkiel, J. D. and Tennyson, J., 'Electron-H_3^+ collisions at intermediate energies', *J. Phys. B: At. Mol. Opt.* **37** (2004), pp. L343–L350.

Gorfinkiel, J. D. and Tennyson, J., 'Electron impact ionization of small molecules at intermediate energies: the molecular R -matrix with pseudostates method', *J. Phys. B: At. Mol. Opt.* **38** (2005), p. 1607.

Gross, E. K. U. and Kohn, W., 'Time-Dependent Density-Functional Theory', *in* Density Functional Theory of Many-Fermion Systems, volume 21 of *Adv. Quantum Chem.* (edited by P.-O. Löwdin) (Academic Press, 1990), pp. 255 – 291.

Haessler, S. et al., 'Attosecond imaging of molecular electronic wavepackets', *Nat. Phys.* **5** (2010), pp. 200 – 206.

Halmová, G., Gorfinkiel, J. D., and Tennyson, J., 'Low and intermediate energy electron collisions with the C_2^- molecular anion', *J. Phys. B: At. Mol. Opt.* **41** (2008), p. 155201.

Halmová, G. and Tennyson, J., 'Resonances in Electron-Impact Electron Detachment of $C_2{}^-$', *Phys. Rev. Lett.* **100** (2008), p. 213202.

Hamnett, A., Stoll, W., and Brion, C. E., 'Photoelectron branching ratios and partial ionization cross-sections for CO and N_2 in the energy range 18-50 eV', *J. Electron Spectrosc.* **8** (1976), pp. 367 – 376.

Harvey, A., 'Electron re-scattering from Aligned Molecules using the R-matrix Method', Ph.D. thesis, University College London (2010), www.tampa.phys.ucl.ac.uk/ftp/eThesis/AlexHarvey2010.pdf.

Harvey, A. G. and Tennyson, J., 'Electron re-scattering from aligned linear molecules using the R-matrix method', *J. Phys. B: At. Mol. Opt.* **42** (2009), p. 095101.

Harvey, A. G. et al., 'CDENPROP: Transition matrix elements involving continuum states', (2013), http://arxiv.org/abs/1401.0229.

Harvey, A. G. et al., 'Photoelectron angular distributions from aligned molecules using the R-matrix method', (2014a), http://arxiv.org/abs/1402.3853.

Harvey, A. G. et al., 'An R-matrix approach to electron-photon-molecule collisions: photoelectron angular distributions from aligned molecules', *J. Phys. B: At. Mol. Opt.* **47** (2014b), p. 215005.

Hayashi, M., 'Electron Collision Cross-Sections Determined from Beam and Swarm Data by Boltzmann Analysis', *in* Nonequilibrium Processes in Partially Ionized Gases (edited by M. Capitelli and J. N. Bardsley) (Springer US, 1990), pp. 333 – 340.

Hiyama, M. and Kosugi, N., 'Ab initio R-matrix/MQDT method for near-edge x-ray absorption fine structure', *Physica Scripta* **2005** (2005), p. 136.

Hiyama, M. and Kosugi, N., 'Ab initio R-matrix/multi-channel quantum defect theory approach to study molecular core excitation and ionization: GSCF4R', *J. Theor. Comput. Chem.* **4** (2015), p. 35.

Hotop, H., Rul, M.-W., and Fabrikant, I. I., 'Resonance and Threshold Phenomena in Low-Energy Electron Collisions with Molecules and Clusters', *Phys. Scripta.* **2004** (2004), p. 22.

Huestis, D. L. et al., 'Cross Sections and Reaction Rates for Comparative Planetary Aeronomy', *Space Sci. Rev.* **139** (2008), pp. 63–105.

Humberston, J. W. et al., 'Positron - hydrogen scattering in the vicinity of the positronium formation threshold', *J. Phys. B: At. Mol. Opt.* **30** (1997), p. 2477.

Ivanov, M. Y., Brabec, T., and Burnett, N., 'Coulomb corrections and polarization effects in high-intensity high-harmonic emission', *Phys. Rev. A* **54** (1996), pp. 742 – 745.

Ivanov, M. Y. and Smirnova, O., 'How Accurate Is the Attosecond Streak Camera?', *Phys. Rev. Lett.* **107** (2011), p. 213605.

Jain, A. and Baluja, K. L., 'Total (elastic plus inelastic) cross sections for electron scattering from diatomic and polyatomic molecules at 10 - 5000 eV: H_2, Li_2, HF, CH_4, N_2, CO, C_2 H_2, HCN, O_2, HCl, H_2S, PH_3, SiH_4, and CO_2', *Phys. Rev. A* **45** (1992), pp. 202 – 218.

Jain, A. and Thompson, D. G., 'Rotational excitation of CH_4 and H_2O by slow electron impact', *J. Phys. B: At. Mol. Opt.* **16** (1983), p. 3077.

Jin, C., Le, A.-T., and Lin, C. D., 'Retrieval of target photorecombination cross sections from high-order harmonics generated in a macroscopic medium', *Phys. Rev. A* **79** (2009), p. 053413.

Johnson III, R. D., 'NIST Computational Chemistry Comparison and Benchmark Database', (2013), nIST Standard Reference Database Number 101, http://cccbdb.nist.gov.

Jones, M. and Tennyson, J., 'On the use of pseudostates to calculate molecular polarizabilities', *J. Phys. B: At. Mol. Opt.* **43** (2010), p. 045101.

de Jong, W. A., Harrison, R. J., and Dixon, D. A., 'Parallel Douglas-Kroll energy and gradients in NWChem: Estimating scalar relativistic effects using Douglas-Kroll contracted basis sets', *J. Chem. Phys.* **114** (2001), pp. 48–53.

Jose, J., Lucchese, R. R., and Rescigno, T. N., 'Interchannel coupling effects in the valence photoionization of SF_6', *J. Chem. Phys.* **140** (2014), p. 204305.

Kapur, P. L. and Peierls, R., 'The Dispersion Formula for Nuclear Reactions', *Proc. Roy. Soc. A* **166** (1938), pp. 277 – 295.

Kato, H. et al., 'Cross sections and Oscilattor strengths for electron-impact excitation of electronic states in polyatomic molecules - Application examples of the BEf-scaling model in optically-allowed transitions', (2009), http://www.nifs.ac.jp/report/nifs-data108.html.

Kim, Y.-K., 'Scaling of plane-wave Born cross sections for electron-impact excitation of neutral atoms', *Phys. Rev. A* **64** (2001), p. 032713.

Kim, Y.-K., 'Scaled Born cross sections for excitation of H_2 by electron impact.', *J. Chem. Phys.* **126** (2007), p. 064305.

Klünder et al., 'Probing Single-Photon Ionization on the Attosecond Time Scale', *Phys. Rev. Lett.* **106** (2011), p. 143002.

Kobourov, S. G., 'Spring embedders and force directed graph drawing algorithms', (2012), http://arxiv.org/pdf/1201.3011.pdf.

Krueger, A. J. and Maitra, N. T., 'Autoionizing resonances in time-dependent density functional theory', *Phys. Chem. Chem. Phys.* **11** (2009), pp. 4655 – 4663.

Kumar, S. S. et al., 'Photodetachment as destruction mechanism for CN^- and C_3N^- anions in circumstellar envelopes', (2013), http://arxiv.org/abs/1307.2709.

Lane, N. F., 'The theory of electron-molecule collisions', *Rev. Mod. Phys.* **52** (1980), pp. 29 – 119.

Lassettre, E. N., 'Power series representation of generalized oscillator strengths.', *J. Chem. Phys.* **43** (1965), p. 4479.

LeClair, L. R. et al., 'A time-of-flight spectrometer for measuring inelastic to elastic differential cross-section ratios for electron-gas scattering', *Rev. Sci. Instrum.* **67** (1996), pp. 1753 – 1760.

Lein, M., Marangos, J. P., and Knight, P. L., 'Electron diffraction in above-threshold ionization of molecules', *Phys. Rev. A* **66** (2002), p. 051404.

Lengsfield III, B. H., Rescigno, T. N., and McCurdy, C. W., 'Ab initio study of low-energy electron-methane scattering', *Phys. Rev. A* **44** (1991), p. 4296.

Lima, M. A. P. et al., 'Cross sections for electron impact excitation of the b $^3\Sigma_u^+$ state of H_2 : an application of the Schwinger multichannel variational method', *J. Phys. B: At. Mol. Phys.* **18** (1985), p. L865.

Little, D. A. and Tennyson, J., 'An R-matrix study of singlet and triplet continuum states of N_2', *J. Phys. B: At. Mol. Opt.* **47** (2014), p. 105204.

Liu, J. W. and Hagstrom, S., 'Generalized oscillator-strength calculations for some low-lying excited states of H_2 using a high-accuracy configuration-interaction wave function', *Phys. Rev. A* **48** (1993), pp. 166 – 172.

Löwdin, P., 'On the Non Orthogonality Problem Connected with the Use of Atomic Wave Functions in the Theory of Molecules and Crystals', *J. Chem. Phys.* **18** (1950), pp. 365 – 375.

Lucchese, R. R., Takatsuka, K., and McKoy, V., 'Applications of the Schwinger variational principle to electron molecule collisions and molecular photoionization', *Phys. Rep.* **131** (1986), pp. 147 – 221.

Lun, A. et al., 'Inversion of electron-water elastic-scattering data', *Phys. Rev. A* **49** (1994), pp. 3788–3798.

Luque, A., Ebert, U., and Hundsdorfer, W., 'Interaction of Streamer Discharges in Air and Other Oxygen-Nitrogen Mixtures', *Phys. Rev. Lett.* **101** (2008), p. 075005.

Lynch, D. L. and Schneider, B. I., 'Molecular photoionization using the complex Kohn variational method', *Phys. Rev. A* **45** (1992), pp. 4494 – 4498.

Machado, L. E., Brescansin, L. M., and Lee, M. T., 'Elastic and rotational excitation cross sections for electron scattering by polyatomic molecules', *Braz. J. Phys.* **32** (2002), pp. 804 – 811.

Madden, D., Tennyson, J., and Zhang, R., 'R-Matrix with Pseudo-States (RMPS) method: Application to CH+ resonances curves', *J. Phys. Conf. Ser.* **300** (2011).

Maddern, T. M. et al., 'Absolute Electron Scattering Cross Sections for the CF_2 Radical', *Phys. Rev. Lett.* **100** (2008a), p. 063202.

Maddern, T. M. et al., 'An apparatus for measuring absolute electron scattering cross sections for molecular radicals', *Measurement Science and Technology* **19** (2008b), p. 085801.

Makochekanwa, C. et al., 'Experimental observation of neutral radical formation from CH_4 by electron impact in the threshold region', *Phys. Rev. A* **74** (2006), p. 042704.

Mapstone, B. and Newell, W. R., 'Elastic differential electron scattering from CH_4, C_2H_4 and C_2H_6', *J. Phys. B: At. Mol. Opt.* **25** (1992), p. 491.

Maschhoff, K. and Sorensen, D., 'PARPACK: An Efficient Portable Large Scale Eigenvalue Package for Distributed Memory Parallel Architectures', (1996), http://www.caam.rice.edu/software/ARPACK.

Mason, N. J., 'The status of the database for plasma processing', *J. Phys. D: Appl. Phys.* **42** (2009), p. 194003.

Mašín, Z. and Gorfinkiel, J. D., 'Towards an accurate representation of the continuum in calculations of electron, positron and laser field interactions with molecules', *J. Phys. Conf. Ser.* **490** (2014), p. 012090.

McLean, A. D. et al., 'ALCHEMY II: A Research Tool for Molecular Electronic Structure and Interactions', *in* Modern Techniques in Computational Chemistry, chapter 6 (Springer, 1991), pp. 233 – 353.

McWeeny, R., 'Methods of Molecular Quantum Mechanics', (Academic Press, London, 1989).

Meckel, M. et al., 'Laser-Induced Electron Tunneling and Diffraction', *Science* **320** (2008), pp. 1478 – 1482.

Meyer, H.-D., 'The equivalence of the log derivative Kohn principle with the R-matrix method', *Chem. Phys. Lett.* **223** (1994), pp. 465 – 468.

Meyer, K. W., Greene, C. H., and Bray, I., 'Simplified model of electron scattering using R-matrix methods', *Phys. Rev. A* **52** (1995), pp. 1334 – 1343.

Meyerhof, W. E., 'Threshold Effects in Average Cross Sections According to **R**-Matrix Theory', *Phys. Rev.* **129** (1963), pp. 692–702.

Meyerhof, W. E. and Laricchia, G., 'Threshold and channel-coupling effects in positron elastic scattering from noble gases', *J. Phys. B: At. Mol. Opt.* **30** (1997), p. 2221.

Michael, B. D. and O'Neill, P., 'A Sting in the Tail of Electron Tracks', *Science* **287** (2000), pp. 1603–1604.

Millar, T. J. et al., 'Hydrocarbon Anions in Interstellar Clouds and Circumstellar Envelopes', *Astrophys. J. Lett.* **662** (2007), pp. L87 – L90, 0705.0639.

Morgan, L. A., 'A generalized R-matrix propagation program for solving coupled second-order differential equations', *Comput. Phys. Commun.* **31** (1984), pp. 419 – 422.

Morgan, L. A., Tennyson, J., and Gillan, C., 'The UK molecular R-matrix codes', *Comput. Phys. Commun.* **114** (1998), pp. 120 – 128.

Morgan, L. A. et al., 'R-matrix calculations for polyatomic molecules: electron scattering by N_2O', *J. Phys. B: At. Mol. Opt.* **30** (1997), pp. 4087–4096.

Morgan, W. L., 'A critical evaluation of low-energy electron impact cross sections for plasma processing modeling. II: Cl_4, SiH_4, and CH_4', *Plasma Chem. Plasma P.* **12** (1992), pp. 477 – 493.

Mori, A., 'Boundary-Condition Constants of the Lane-Robson Calculable Theory', *Phys. Rev. C* **5** (1972), pp. 1795–1796.

Morrison, M. A. and Sun, W., 'How to Calculate Rotational and Vibrational Cross Sections for Low-Energy Electron Scattering from Diatomic Molecules using Close-Coupling Techniques', *in* Computational Methods for Electron - Molecule Collisions (edited by W. Huo and F. Gianturco) (Springer US, 1995), ISBN 978-1-4757-9799-2, pp. 131–190.

Motlagh, S. and Moore, J. H., 'Cross sections for radicals from electron impact on methane and fluoroalkanes', *J. Chem. Phys.* **109** (1998), pp. 432 – 438.

Müller, R. et al., 'Rotational excitation of CH_4 by low-energy-electron collisions', *J. Phys. B: At. Mol. Opt.* **18** (1985), p. 3971.

Munro, J. J. et al., 'A dissociative electron attachment cross-section estimator', *J. Phys. Conf. Ser.* **388** (2012), p. 012013.

Nakano, T., Toyoda, H., and Sugai, H., 'Electron-Impact Dissociation of Methane into CH_3 and CH_2 Radicals II. Absolute Cross Sections', *Jpn. J. Appl. Phys. 1* **30** (1991), pp. 2912 – 2915.

Nesbet, R. K., 'Variational calculations of accurate e^- - He cross sections below 19 eV', *Phys. Rev. A* **20** (1979), pp. 58 – 70.

Nestmann, B. M., Nesbet, R. K., and Peyerimhoff, D., 'A concept for improving the efficiency of R-matrix calculations for electron-molecule scattering', *J. Phys. B: At. Mol. Opt.* **24** (1991), p. 5133.

Nestmann, B. M., Pfingst, K., and Peyerimhoff, S. D., 'R-matrix calculation for electron methane scattering cross-sections.', *J. Phys. B: At. Mol. Opt.* **27** (1994), pp. 2297 – 2308.

Nickel, J. C. et al., 'Principles and procedures for determining absolute differential electron-molecule (atom) scattering cross sections', *J. Phys. E: Sci. Instrum.* **22** (1989), p. 730.

Niikura, H. et al., 'Sub-laser-cycle electron pulses for probing molecular dynamics', *Nature* **417** (2002), pp. 917 – 922.

Niikura, H. et al., 'Probing molecular dynamics with attosecond resolution using correlated wave packet pairs', *Nature* **421** (2003), pp. 826 – 829.

Noble, C. J., 'The ALCHEMY linear molecule integral generator', (1982), technical memorandum, http://purl.org/net/epubs/manifestation/5220.

Noble, C. J., Burke, P. G., and Salvini, S., 'Low-energy scattering of electrons by diatomic molecules', *J. Phys. B: At. Mol. Opt.* **15** (1982), p. 3779.

Noble, C. J. and Nesbet, R. K., 'CFASYM, a program for the calculation of the asymptotic solutions of the coupled equations of electron collision theory', *Comput. Phys. Commun.* **33** (1984), pp. 399 – 411.

Olney, T. N. et al., 'Absolute scale determination for photoabsorption spectra and the calculation of molecular properties using dipole sum-rules', *Chem. Phys.* **223** (1997), pp. 59 – 98.

O'Malley, T. F., 'Extrapolation of Electron-Rare Gas Atom Cross Sections to Zero Energy', *Phys. Rev.* **130** (1963), pp. 1020 – 1029.

O'Malley, T. F. and Crompton, R. W., 'Electron-neon scattering length and S-wave phaseshifts from drift velocities', *J. Phys. B: At. Mol. Opt.* **13** (1980), p. 3451.

O'Malley, T. F., Rosenberg, L., and Spruch, L., 'Low-Energy Scattering of a Charged Particle by a Neutral Polarizable System', *Phys. Rev.* **125** (1962), pp. 1300 – 1310.

Orel, A. E. and Rescigno, T. N., 'Photoionization of ammonia', *Chem. Phys. Lett.* **269** (1997), pp. 222 – 226.

Paul, P. M. et al., 'Observation of a Train of Attosecond Pulses from High Harmonic Generation', *Science* **292** (2001), pp. 1689 – 1692.

Peterson, K. A., 'Systematically convergent basis sets with relativistic pseudopotentials. I. Correlation consistent basis sets for the post-d group 13 - 15 elements', *J. Chem. Phys.* **119** (2003), pp. 11099–11112.

Peterson, K. A. and Dunning Jr., T. H., 'Accurate correlation consistent basis sets for molecular core-valence correlation effects: The second row atoms Al-Ar, and the first row atoms B-Ne revisited', *J. Chem. Phys.* **117** (2002), p. 10548.

Pfingst, K., Nestmann, B. M., and Peyerimhoff, S. D., 'An R-matrix approach for electron scattering off polyatomic molecules', *J. Phys. B: At. Mol. Opt. Phys.* **27** (1994), p. 2283.

Plummer, M., Noble, C. J., and Le Dourneuf, M., 'Low-energy behaviour of e^- - O scattering calculations', *J. Phys. B: At. Mol. Opt.* **37** (2004), p. 2979.

Pople, J. A. and Nesbet, R. K., 'Self-Consistent Orbitals for Radicals', *J. Chem. Phys.* **22** (1954), pp. 571–572.

Prager, J., Riedel, U., and Warnatz, J., 'Modeling ion chemistry and charged species diffusion in lean methane-oxygen flames', *Proc. Combust. Inst.* **31** (2007), p. 1129.

Rabadán, I. and Tennyson, J., 'R-matrix calculation of the bound and continuum states of the e^- - NO^+ system', *J. Phys. B: At. Mol. Opt.* **29** (1996), p. 3747.

Read, F. H. and Channing, J. M., 'Production and optical properties of an unscreened but localized magnetic field', *Review of Scientific Instruments* **67** (1996), pp. 2372–2377.

Reiter, D. and Janev, R. K., 'Hydrocarbon Collision Cross Sections for Magnetic Fusion: The Methane, Ethane and Propane Families', *Contrib. Plasm. Phys.* **50** (2010), pp. 986 – 1013.

Rescigno, T. N., 'Low-energy electron-collision processes in molecular chlorine', *Phys. Rev. A* **50** (1994), pp. 1382 – 1389.

Rescigno, T. N. et al., 'The Complex Kohn Variational Method', (1995), pp. 1 – 44.

Resigno, T. N. and Lengsfield III, B. H., 'The incorporation of modern electronic structure methods in electron molecule collision problems variational calculations using the complex Kohn method', *in* Modern Electronic Structure Theory (edited by D. R. Yarkony), chapter 9 (World Scientific Publishing, 1995), pp. 502 – 583.

Roberts, P., 'Parallelisation and porting of UKRMol-in, the electron-molecule scattering inner region R-matrix codes', (2012), `http://www.hector.ac.uk/cse/distributedcse/reports/UKRMolin/`.

Röllig, M. et al., 'A photon dominated region code comparison study', *Astron. Astrophys.* **467** (2007), pp. 187 – 206.

Rouzée, A. et al., 'Imaging the electronic structure of valence orbitals in the XUV ionization of aligned molecules', *J. Phys. B: At. Mol. Phys.* **47** (2014), p. 124017.

Rozum, I., Mason, N. J., and Tennyson, J., 'Electron collisions with the CF radicals using the R-matrix method.', *J. Phys. B: At. Mol. Opt.* **36** (2003), pp. 2419 – 2432.

Samson, J. A. R., Gardner, J. L., and Starace, A. F., '$^2P_{\frac{3}{2}}$:^{2} $P_{\frac{1}{2}}$ partial photoionization cross-section ratios in the rare gases', *Phys. Rev. A* **12** (1975), pp. 1459 – 1463.

Samson, J. A. R. and Haddad, G. N., 'Total photoabsorption cross sections of H_2 from 18 to 113 eV', *J. Opt. Soc. Am. B* **11** (1994), pp. 277 – 279.

Samson, J. A. R., Haddad, G. N., and Gardner, J. L., 'Total and partial photoionization cross sections of N $_2$ from threshold to 100 eV', *J. Phys. B: At. Mol. Opt.* **10** (1977), p. 1749.

Sanna, N. and Gianturco, F. A., 'Differential cross sections for electron-positron scattering from polyatomic molecules', *Comput. Phys. Commun.* **114** (1998), pp. 142 – 167.

Sarpal, B. K. et al., 'Bound states using the R-Matrix method - Rydberg states of HeH.', *J. Phys. B: At. Mol. Opt.* **24** (1991), pp. 3685 – 3699.

Schneider, B. I., 'R-matrix theory for electron-atom and electron-molecule collisions using analytic basis set expansions', *Chem. Phys. Lett.* **31** (1975a), pp. 237 – 241.

Schneider, B. I., 'R-matrix theory for electron-molecule collisions using analytic basis set expansions. II. Electron-H_2 scattering in the static-exchange model', *Phys. Rev. A* **11** (1975b), pp. 1957–1962.

Schneider, B. I. and Collins, L. A., 'Electronic excitation of the b $^3\Sigma_u$ state of H_2 by electron impact in the linear algebraic approach', *J. Phys. B: At. Mol. Phys.* **18** (1985), p. L857.

Schneider, B. I. and Hay, P. J., 'Elastic scattering of electrons from F_2: An **R**-matrix calculation', *Phys. Rev. A* **13** (1976), pp. 2049–2056.

Schneider, B. I. and Rescigno, T. N., 'Complex Kohn variational method: Application to low-energy electron-molecule collisions', *Phys. Rev. A* **37** (1988), pp. 3749–3754.

Schultze, M. et al., 'Delay in Photoemission', *Science* **328** (2010), pp. 1658 – 1662.

Senftleben, A. et al., 'Fivefold differential cross sections for ground-state ionization of aligned H_2 by electron impact', *J. Chem. Phys.* **133** (2010), p. 044302.

Shi, X. and Burrow, P. D., 'Differential scattering cross sections of neon at low electron energies', *J. Phys. B: At. Mol. Opt.* **25** (1992), p. 4273.

Shirai, T. et al., 'Analytic cross sections for electron collisions with hydrocarbons: CH_4, C_2H_6, C_2H_4, C_2H_2, C_3H_8, and C_3H_6', *Atomic Data and Nuclear Data Tables* **80** (2002), pp. 147 – 204.

Shyn, T. W. and Cravens, T. E., 'Angular distribution of electrons elastically scattered from CH_4', *J. Phys. B: At. Mol. Opt.* **23** (1990), p. 293.

Smirnova, O. et al., 'High harmonic interferometry of multi-electron dynamics in molecules', *Nature* **460** (2009), pp. 972–977.

Sohn, W. et al., 'Elastic electron scattering from CH_4 for collision energies between 0.2 and 5 eV', *J. Phys. B: At. Mol. Opt.* **19** (1986), p. 3625.

Song, M. et al., 'Cross sections for electron collisions with methane', *J. Phys. Chem. Ref. Data* (2015).

Spanner, M. et al., 'Reading diffraction images in strong field ionization of diatomic molecules', *J. Phys. B: At. Mol. Opt.* **37** (2004), p. L243.

Stener, M. et al., 'Recent advances in molecular photoionization by density functional theory based approaches', *Theor. Chem. Acc.* **117** (2007), pp. 943 – 956.

Stibbe, D. T. and Tennyson, J., 'Time-delay matrix analysis of resonances in electron scattering: e^- - H_2 and H_2^+', *J. Phys. B: At. Mol. Opt.* **29** (1996), p. 4267.

Stibbe, D. T. and Tennyson, J., 'Near-threshold electron impact dissociation of H2 within the adiabatic nuclei approximation', *New J. Phys.* **1** (1998), pp. 1 – 9.

Stratmann, R. E. and Lucchese, R. R., 'A graphical unitary-group approach to study multiplet specific multichannel electron correlation-effects in the photoionization of O_2.', *J. Chem. Phys.* **102** (1995), pp. 8493 – 8505.

Stratmann, R. E., Zurales, R. W., and Lucchese, R. R., 'Multiplet-specific multichannel electron-correlation effects in the photoionization of NO', *J. Chem. Phys.* **104** (1996), pp. 8989 – 9000.

Sun, W. et al., 'Detailed theoretical and experimental analysis of low-energy electron-N_2 scattering', *Phys. Rev. A* **52** (1995), pp. 1229 – 1256.

Sunderland, A. G., Noble, C. J., and Plummer, M., 'Future Proof Parallelism for Electron - Atom Scattering Codes on the XT4', *in* Cray User Group Meeting, Atlanta, Georgia, USA (2009), pp. 1 – 10, http://www.hector.ac.uk/cse/distributedcse/reports/prmat/.

Sunderland, A. G. et al., 'A parallel R-matrix program PRMAT for electron-atom and electron-ion scattering calculations', *Comput. Phys. Commun.* **145** (2002), pp. 311 – 340.

Takatsuka, K., Lucchese, R. R., and McKoy, V., 'Relationship between the Schwinger and Kohn-type variational principles in scattering theory', *Phys. Rev. A* **24** (1981), pp. 1812 – 1816.

Takatsuka, K. and McKoy, V., 'Extension of the Schwinger variational principle beyond the static-exchange approximation', *Phys. Rev. A* **24** (1981), pp. 2473 – 2480.

Takatsuka, K. and McKoy, V., 'Theory of electronically inelastic scattering of electrons by molecules', *Phys. Rev. A* **30** (1984), pp. 1734 – 1740.

Tanaka, H. et al., 'Differential cross sections for elastic scattering of electrons by CH_4 in the energy range of 3 to 20 eV', *J. Phys. B: At. Mol. Opt.* **15** (1982), p. 3305.

Tao, L., McCurdy, C. W., and Rescigno, T. N., 'Grid-based methods for diatomic quantum scattering problems: A finite-element discrete-variable representation in prolate spheroidal coordinates', *Phys. Rev. A* **79** (2009), p. 012719.

Tarana, M. and Horáček, J., 'Correlation effects in R-matrix calculations of electron-F_2 elastic scattering cross sections', *J. Chem. Phys.* **127** (2007), p. 154319.

Tarana, M. et al., 'Effects of two vibrational modes in the dissociative electron attachment to CF_3Cl', *Phys. Rev. A* **79** (2009), p. 052712.

Tashiro, M., 'Application of the R-matrix method to photoionization of molecules', *J. Chem. Phys.* **132** (2010), p. 134306.

Tashiro, M., Ueda, K., and Ehara, M., 'Double core-hole correlation satellite spectra of N_2 and CO molecules', *Chem. Phys. Lett.* **521** (2012), pp. 45 – 51.

Taylor, J. R., 'Scattering Theory: The Quantum Theory of Nonrelativistic Collisions', (John Wiley & Sons, New York, 1972).

Tennyson, J., 'Fully vibrationally resolved photoionisation of H_2 and D_2', *J. Phys. B: At. Mol. Phys.* **20** (1987), p. L375.

Tennyson, J., 'Calculated Vibrationally and Rotationally Resolved Photoelectron Spectra of H2', *in* Electron-Molecule Scattering and Photoionization, Physics of Atoms and Molecules, chapter 19 (Springer US, 1988), ISBN 978-1-4612-8309-6, pp. 247 – 251.

Tennyson, J., 'A new algorithm for Hamiltonian matrix construction in electron-molecule collision calculations', *J. Phys. B: At. Mol. Opt.* **29** (1996a), pp. 1817–1828.

Tennyson, J., 'R-matrix calculation of Rydberg states of CO.', *J. Phys. B: At. Mol. Opt.* **29** (1996b), pp. 6185 – 6201.

Tennyson, J., 'Phase factors in electron-molecule collision calculations', *Comput. Phys. Commun.* **100** (1997), pp. 26–30.

Tennyson, J., 'Partitioned **R**-matrix theory for molecules', *J. Phys. B: At. Mol. Opt.* **37** (2004), p. 1061.

Tennyson, J., 'Electron - molecule collision calculations using the **R**-matrix method', *Phys. Rep.* **491** (2010), pp. 29 – 76.

Tennyson, J. and Chandra, N., 'PEAD âĂŤ for the calculation of photoelectron angular distributions of linear molecules', *Comput. Phys. Commun.* **46** (1987), pp. 99 – 105.

Tennyson, J. and Noble, C. J., 'RESON - A program for the detection and fitting of Breit-Wigner resonances', *Comput. Phys. Commun.* **33** (1984), pp. 421–424.

Tennyson, J., Noble, C. J., and Burke, P. G., 'Continuum states of the hydrogen molecule with the R-matrix method', *Int. J. Quantum Chem.* **29** (1986), pp. 1033 – 1042.

Tennyson, J. et al., 'Quantemol-N: an expert system for performing electron molecule collision calculations using the R-matrix method', *J. Phys. Conf. Ser.* **86** (2007), p. 012001.

Trajmar, S. and McConkey, J. W., 'Benchmark Measurements of Cross Sections for Electron Collisions: Analysis of Scattered Electrons', *in* Cross Section Data, volume 33 of *Advances In Atomic, Molecular, and Optical Physics* (edited by M. Inokuti) (Academic Press, 1994), pp. 63 – 96.

Trajmar, S., McConkey, W., and Kanik, I., 'Electron-Atom and Electron-Molecule Collisions', *in* Springer Handbook of Atomic, Molecular, and Optical Physics (edited by G. Drake) (Springer New York, 2006), ISBN 978-0-387-20802-2, pp. 929–941.

Truhlar, D. G., Abdallah, J., and Smith, R. L., 'Algebraic Variational Methods in Scattering Theory', *in* Advances in Chemical Physics (edited by I. Prigogine and S. A. Rice), chapter 4 (John Wiley & Sons, Inc., 2007), ISBN 9780470143773, pp. 211 – 293.

Varambhia, H. N., Munro, J. J., and Tennyson, J., 'R-matrix calculations of low-energy electron alkane collisions', *Int. J. Mass Spectrom.* **271** (2008), pp. 1 – 7.

Varella, M. T. do N. et al., 'Applications of the Schwinger Multichannel Method with Pseudopotentials to electron scattering from polyatomic molecules II. rotational excitation cross sections', *Braz. J. Phys.* **31** (2001), pp. 21 – 29.

Vinodkumar et al., 'Electron impact calculations of total elastic cross sections over a wide energy range 0.01 eV to 2 keV for CH_4, SiH_4 and H_2O', *Eur. Phys. J. D* **61** (2001), pp. 579–585.

Vriens, L., 'Excitation of Helium by Electrons and Protons', *Phys. Rev.* **160** (1967), pp. 100 – 108.

Wainfan, N., Walker, W. C., and Weissler, G. L., 'Photoionization Efficiencies and Cross Sections in O_2, N_2, CO_2, H_2O, H_2, and CH_4', *Phys. Rev.* **99** (1955), pp. 542 – 549.

Werner, H.-J. et al., 'Molpro: a general-purpose quantum chemistry program package', *WIREs Comput. Mol. Sci.* **2** (2012), pp. 242–253.

van der Wiel, M. J. et al., 'Partial oscillator strengths (25 - 50 eV) of the one-electron states of CH_4^+, measured in an (e, 2e) experiment', *Chem. Phys. Lett.* **37** (1976), pp. 240 – 242.

Wigner, E. P., 'Resonance Reactions', *Phys. Rev.* **70** (1946a), pp. 606 – 618.

Wigner, E. P., 'Resonance Reactions and Anomalous Scattering', *Phys. Rev.* **70** (1946b), pp. 15 – 33.

Wigner, E. P. and Eisenbud, L., 'Higher Angular Momenta and Long Range Interaction in Resonance Reactions', *Phys. Rev.* **72** (1947), pp. 29 – 41.

Wilde, R. S., Gallup, G. A., and Fabrikant, I. I., 'Semiempirical R-matrix theory of low energy electron-CF_3Cl inelastic scattering', *J. Phys. B: At. Mol. Opt.* **32** (1999), p. 663.

Winstead, C. and Mckoy, V., 'Electron - Molecule Collisions in Low-Temperature Plasmas: The Role of Theory', *in* Fundamentals of Plasma Chemistry, volume 43 of *Advances In Atomic, Molecular, and Optical Physics* (edited by B. Bederson and H. Walther) (Academic Press, 2000), pp. 111 – 145.

Winstead, C. et al., 'Studies of electron-molecule collisions on distributed-memory parallel computers', *Aust. J. Phys.* **45** (1992), pp. 325 – 336.

Winstead, C. et al., 'Electronic excitation of CH_4 by low-energy electron-impact', *J. Chem. Phys.* **98** (1993), pp. 2132 – 2137.

Winters, H. F., 'Dissociation of methane by electron impact', *J. Chem. Phys.* **63** (1975), pp. 3462 – 3466.

Wisman, D. L., Marcum, S. D., and Ganguly, B. N., 'Electrical control of the thermodiffusive instability in premixed propane-air flames', *Combust. Flame* **151** (2007), p. 639.

Zammit, M. C., Fursa, D. V., and Bray, I., 'Electron scattering from the molecular hydrogen ion and its isotopologues', *Phys. Rev. A* **90** (2014).

Zatsarinny, O., Bartschat, K., and Tayal, S. S., 'Low-energy elastic electron scattering by atomic oxygen', *J. Phys. B: At. Mol. Opt.* **39** (2006), p. 1237.

Zhang, R., Galiatsatos, P. G., and Tennyson, J., 'Positron collisions with acetylene calculated using the R-matrix with pseudo-states method', *J. Phys. B: At. Mol. Opt.* **44** (2011), p. 195203.

Ziółlkowski, M. et al., 'Modeling the electron-impact dissociation of methane', *J. Chem. Phys.* **137** (2012), p. 22A510.

Zou, W. et al., 'Ab initio calculations on the ground and low-lying excited states of InI', *Mol. Phys.* **101** (2003), pp. 2963 – 2968.

Zubek, M. et al., 'Measurements of elastic electron scattering in the backward hemisphere', *J. Phys. B: At. Mol. Opt. Phys.* **29** (1996), pp. L239–L244.

Zuo, T., Bandrauk, A. D., and Corkum, P. B., 'Laser-induced electron diffraction: a new tool for probing ultrafast molecular dynamics', *Chem. Phys. Lett.* **259** (1996), pp. 313 – 320.